43èmes Journées des Actinides

Programme and Abstracts

Sestri Levante, Italy
6-9 April 2013

43èmes Journées des Actinides
(43th JdA)

Centro Congressi
Convento dell'Annunziata
Sala Oleandro
Via Portobello, 16039 Sestri Levante (GE)

Sestri Levante, Italy
6-9th April 2013

Organized by

University of Genoa

Department of Chemistry and Industrial Chemistry, Genoa

CNR Institute SPIN, Genoa

UNIVERSITÀ DEGLI STUDI
DI GENOVA

Scope

This conference is a traditional forum for informal discussion encompassing numerous different aspects related to the chemistry and physics of the actinides. It regularly brings together experts from all the fields involved, emphasizing exchanges and lively discussions on current issues in actinide science and stimulating new collaborative projects. Moreover, a strong emphasis is given on presentations of on-going research projects by young scientists and PhD students.

Journées des Actinides - Committees

Conference Chairs

Mauro Giovannini (DCCI- Genova University, Italy)

Roberto Caciuffo (JRC-ITU, Karlsruhe, Germany)

Local organizing Committee

Mauro Giovannini (DCCI)

Adriana Saccone (DCCI)

Marco Ripani (INFN)

Alberto Martinelli (CNR-SPIN)

Anna Cardinale (DCCI)

Pavlo Solokha (DCCI)

International Advisory Committee

Jean Aupiais (Arpajon, France)

Eric Colineau (Karlsruhe, Germany)

Nicolas Dacheux (Montpellier, France)

David Geeson (Reading, UK)

Antonio Pereira Gonçalves (Sacavém, Portugal)

Ladislav Havela (Prague, Czech Republic)

Itzhak Halevy (Be'er Sheva, Israel)

Dariusz Kaczorowski (Wroclaw, Poland)

Marian Mihalik (Košice, Slovakia)

Thomas B. Scott (Bristol, UK)

43th JdA was supported by:

University of Genova

Enlargement and Integration Action 2013 of the EU

Ansaldo Nucleare Spa Italy

Istituto Nazionale di Fisica Nucleare (INFN)

Nanovision S.r.l.

Panalytical S.r.l.;

AGENTE E DISTRIBUTORE AIR LIQUIDE
ITALIA SERVICE SRL

Comune di Sestri Levante

Programme

Saturday, 6th April 2013

17.30-19.00	Registration
19.00-22.00	Welcome Party

Sunday, 7th April 2013

9.00-9.10		Welcome address
		Session I - Actinides and The Fourth Generation Challenge
9.10-9.30	I-O1	A. Alemberti, L. Mansani *The European Lead Fast Reactor strategy and the Roadmap for the demonstrator ALFRED*
9.30-9.50	I-O2	L. Mansani, A. Alemberti *The Lead Fast Reactor: Design of the European LFR (ELFR) and of the Demonstrator ALFRED*
9.50-10.10	I-O3	P. Agostini *Issues and considerations for fuel cladding materials of ALFRED reactor*
10.10-10.30	I-O4	G. Grasso *An effective strategy for recycling all actinides: the adiabatic reactor concept*
10.30-10.50	I-O5	M. Ripani *The strategic project INFN-E*
10.50-11.20		**Coffee break**
		Session II – Celebrating the 40th anniversary of JdA
11.20-11.40	II-O6	J.-M. Fournier *Journées des Actinides : 40 years in perspective*
11.40-12.00	II-O7	G. H. Lander *Looking back over 40 years on the actinide dioxides*
12.00-12.20	II-O8	R. Troć *Historical view of the studies of actinide compounds*
12.20-12.40	II-O9	P. Wachter *Localized versus itinerant: Towards the limits.*
12.40-14.20		**Lunch**

Session III – Superconductivity

14.20-14.40	III-O10	L. Havela, I. Tkach, N.-T.H. Kim-Ngan, S. Mašková, A.P. Gonçalves, A. Warren, T. Scott *Electronic properties of □-U and superconductivity of U-Mo alloys*
14.40-15.00	III-O11	A.P. Gonçalves, M.S. Henriques, E.B. Lopes, L.C.J. Pereira, A. Janssen, T. Wiss, L. Havela *HRTEM studies on the UCoGe ferromagnetic superconductor*
15.00-15.20	III-O12	A. Hen, I. Halevy, I. Orion, E. Colineau, R. Eloirdi, J.-C. Griveau, P. Gaczyński, T. Klimczuk, J.-P. Sanchez, A. B. Shick, R. Caciuffo *Superconductivity and Mössbauer effect in actinides*
15.20-15.40	III-O13	A. B. Shick, T. Klimczuk, R. Eloirdi, E. Colineau, J.-C. Griveau, and R. Caciuffo *Electronic structure and magnetic properties of NpFeAsO and PuFeAsO*
15.40-16.10		**Coffee break**

Session IV – Magnetism

16.10-16.30	IV-O14	E. Colineau, J.-C. Griveau, R. Eloirdi, R. Caciuffo *Preliminary investigations on the new compound NpRuGe*
16.30-16.50	IV-O15	R. Gumeniuk, W. Schnelle, U. Burkhardt, H. Borrmann, M. Nicklas, A. Leithe-Jasper, Y. Grin *$ThPt_2$ – a new representative of close packed tetragonal structures*
16.50-17.10	IV-O16	J.-C. Griveau, E. Colineau, D. Bouëxière, K. Gofryk, T. Klimczuk, and J. Rebizant *Magnetic properties of the new Pu-based ferromagnet $Pu_2Pt_3Si_5$*
17.10-17.30	IV-O17	M.S. Henriques, D.I. Gorbunov, J.C. Waerenborgh, L. Havela, A.B. Shick, M. Diviš, A.V. Andreev, A.P. Gonçalves *Peculiar magnetism of U_2Fe_3Ge probed in single crystal studies*
17.30-17.50	IV-O18	I. Tkach, N.-T.H. Kim-Ngan, S. Mašková, L. Havela, A.V. Andreev, Z. Matej *Amorphous 5f ferromagnetic hydrides UH_3Mo_x*
17.50-19.20		**Poster session**
19.50-22.00		**Dinner**

Monday, 8th April 2013

Session V – Theory, Electronic structure

8.40-9.00	V-O19	G. Zwicknagl *5f correlations and core level photoelectron spectra of actinides*
9.00-9.20	V-O20	M. Samsel-Czekała, M.J. Winiarski *Electronic and magnetic structures of U_2N_2(P;As;S;Se) having the highest Néel temperatures among uranium compounds*
9.20-9.40	V-O21	S. Khmelevskyi, A. B. Shick, E. Colineau *Theoretical modeling of complex antiferromagnetic state in NpCoGe intermetallic compound*
9.40-10.00	V-O22	A. I Bram, A. Venkert, L. Meshi *Towards prediction of symmetry of the intermetallic structures formed in the Al-TM-Ac alloys*
10.00-10.20	V-O23	B. Dorado, P. Garcia *First-principles modeling of uranium and plutonium mixed oxide*
10.20-10.40	V-O24	E. Vathonne, M. Freyss, B. Amadon, M. Bertolus *First-principles study of radiation damage in uranium dioxide: inclusion of strong electronic correlations and van der Waals interactions*
10.40-11.10		**Coffee break**

Session VI – Materials

11.10-11.30	VI-O25	N.J. Harker, T.B. Scott, C.P. Jones, J.R. Petherbridge, J. Glascott *Altering the hydriding behaviour of uranium metal by induced oxide penetration around carbonitride inclusions*
11.30-11.50	VI-O26	A.M. Adamska, T.B. Scott, R. Springell, P.J. Heard, K.R. Hallam and C.M. Younes *Characterization of uranium-molybdenum alloys and associated surface corrosion products*
11.50-12.10	VI-O27	C. Stitt, R.A. Crane, C. Jones, T.B. Scott *The influence of surface topography on the initiation of uranium hydriding*
12.10-12.30	VI-O28	C.J. Broan, D.T. Goddard, R. Orr, H. Godfrey, A. Diggle *The influence of the temperature of preparation on the alpha/beta phase ratio of uranium hydride and on its rate of hydrolysis*
12.30-12.50	VI-O29	M. Shandalov, I. Kelson and E. Yahel *A New Concept in Radiation Damage Studies: System Model for Self-Irradiation Experiments in Th-doped PbSe and PbS Thin Films*

12.50-14.30		**Lunch**

Session VII – Magnetism 2

14.30-14.50	VII-O30	R. Eloirdi, A.J. Fuchs, J.-C. Griveau, E. Colineau, A.B. Shick, D. Manara and R. Caciuffo *Evidence for persistent spin-fluctuations in uranium sesquicarbide*
14.50-15.10	VII-O31	F. Wilhelm, R. Eloirdi, J. Rusz, R. Springell, E. Colineau, J.-C. Griveau, P.M. Oppeneer, R. Caciuffo, A. Rogalev and G. H. Lander *X-ray magnetic circular dichroism experiments and theory of transuranium Laves phase compounds*
15.10-15.30	VII-O32	Z. Bao, E. Tereshina, C. Kübel, S. Daniš, L. Havela, T. Gouder, R. Caciuffo *Exchange bias in UO_2/Fe_3O_4 bilayers*
15.30-15.50	VII-O33	S. Maskova, L. Havela, S. Danis *New ternary compounds $U_3Si_2H_{1.8}$ and UNiZn and their properties*
15.50-16.10	VII-O34	D.I. Gorbunov, M.S. Henriques, J.C. Waerenborgh, L. Havela, A.V. Andreev, Y. Skourski, A.P. Gonçalves *A single crystal study of $U_3Fe_4Ge_4$*
16.10-16.30	VII-O35	A. Hen, E. Colineau, R. Eloirdi, J.-C. Griveau, J.-P. Sanchez, A.B. Shick, I. Halevy, I. Orion, and R. Caciuffo *Electronic and Magnetic Properties of $NpNi_5$.*
16.30-17.00		**Coffee break**

Session VIII: New EU Projects - Access to Research Infrastructures

17.00-17.20		E. Colineau *The Actinide User Laboratory (ActUsLab) at JRC-ITU*
17.20-17.40		L. Havela *The new large user project TALISMAN*
17.40-19.00		**Break**
19.00-23.00		**Conference dinner**

Tuesday, 9th April 2013

Session IX: Fuels, environment

9.00-9.20	IX-O36	D.W. Wheeler, R.F.E. Jenkins, P. Roussel, R.K.B. Gover, M.B. Matthews *Observations and characterisation of a Pu-0.18 wt. % Ga alloy*
9.20-9.40	IX-O37	O.S. Vălu, O. Beneš, R.J.M. Konings, J. Somers *Thermodynamic investigations of the (U, Am)O_2 solid solution*
9.40-10.00	IX-O38	J. MacFarlane *Using Autonomous Aerial Vehicles for Radiation Detection*
10.00-10.20	IX-O39	B. Negulici, V.P. Gheorghe, A. Gheorghe *Experimental Assessment Techniques for CANDU Pressure Tubes Degradation Mechanisms*
10.20-10.40		**Coffee break**

Session X: Chemistry

10.40-11.00	X-O40	V. Sladkov, M. Meyer, S. Brandès, J.-C. Chambron, P. Jewula *Interaction of U(VI) with Siderochelates by Affinity Capillary Electrophoresis*
11.00-11.20	X-O41	I.N.Izosimov, N.G.Firsin, N.G.Gorshkov, V.A.Mikhalev, S.N.Nekhoroshkov *Time-Resolved Laser Induced Chemiluminescence Spectroscopy of Aqueous Actinide and Lanthanide Containing Solutions*
11.20-12.10		**Closing session**
12.10-14.00		**Lunch**

ORAL COMUNICATIONS

The European Lead Fast Reactor strategy and the Roadmap for the demonstrator ALFRED

Alessandro Alemberti,[1] Luigi Mansani[1]

[1] *Ansaldo Nucleare, Corso Perrone,25, 16152 Genova, Italy, e-mail: Presenting.author@example.it*

The development of the technology for a new reactor must follow a chain of gradual and progressive steps to reach maturity. This paper presents the strategy for the development of a nuclear fast reactor with closed fuel cycle and based on lead coolant technology for economical electricity production: the European Lead Fast Reactor (ELFR) [1]. This reactor has the potential to multiply by two orders of magnitude the energy output from a given amount of uranium while improving the safety of the plant and the management of HLRW through the transmutation of minor actinides. The roadmap of ELFR is based on the progressive up-scaling from a zero power facility to the commercial deployment of the first-of-a kind plant. The intermediate steps are a Technological Pilot Plant (MYRRHA) [2], a Demonstrator (ALFRED) and a Prototype (PROLFR). The roadmap of the demonstrator ALFRED, scheduled to be in operation around 2025, is also presented.

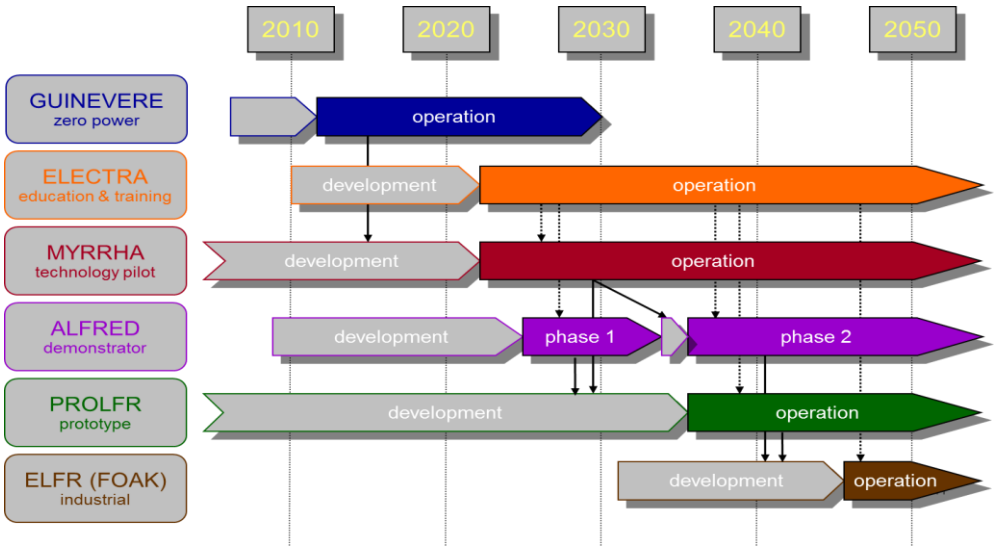

Figure1 Overall roadmap for deployment of a European LFR

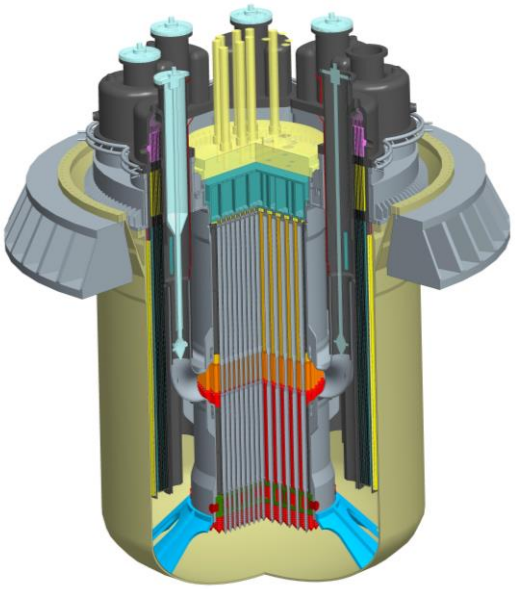

Figure 2 3D view of the ALFRED reactor block

A huge potential increase in the sustainability of nuclear energy will be achieved through demonstrating the technical, industrial and economic viability of Generation IV fast neutron reactors, thereby ensuring that nuclear energy can remain a long-term contributor to a low carbon economy. This demonstration program will play a key role by involving European industry and maintaining and developing European leadership in nuclear technologies worldwide. It will also make possible the further commercial deployment by the European industry of these technologies by 2040 and beyond. This is the prime goal for industry, which in the mean time will seek to maintain at least a 30% share of EU electricity from currently available reactors for the benefit of the European economy (the industrial needs for nuclear energy could be enhanced with an expansion towards co-generation of process heat for industrial applications when such markets develop). With the construction and operation of a LFR ETPP (MYRRHA) and ETDR (ALFRED), Europe will be in an excellent position to secure the development of a safe, sustainable and competitive fast spectrum technology. The program will allow to investigate and address the main technological issues that can then be implemented in the LFR prototype around 2020-2035. This LFR prototype, in turn, will pave the way for industrial deployment of industrial LFRs by 2050, and hence contribute significantly to the development of a sustainable and secure energy supply for Europe from the second half of this century onwards.

References

[1] Alemberti A., et al., “The Lead fast reactor - Demonstrator (ALFRED) and ELFR design”, International Conference on Fast Reactors and Related Fuel Cycles: Safe Technologies and Sustainable Scenarios (FR13), Paris, France (2013)..

[2] Aït Abderrahim, H., et all., “MYRRHA, a multi-purpose fast spectrum research reactor”, Energy Conversion & Management, Volume 63, 4-10, 2012

The Lead Fast Reactor: Design of the European LFR (ELFR) and of the Demonstrator ALFRED

Luigi Mansani,[1] Alessandro Alemberti[1]

[1] *Ansaldo Nucleare, Corso Perrone,25, 16152 Genova, Italy, e-mail: luigi.mansani@ann.ansaldo.it*

Ansaldo Nucleare, as coordinator of the LEADER project (Lead-cooled European Advanced DEmonstration Reactor) [1], funded by the EC in the frame of the 7th FP, is promoting research and development on Lead Fast Reactors. The LEADER project has the objective to design a commercially viable reactor, for large-scale electricity production (ELFR), based on lead coolant technology. The industrial deployment of ELFR requires a scaled demonstrator reactor, with the objective to demonstrate the achievement of the required safety standards, to assess economic competitiveness of lead technology, and to validate the engineering options and materials selection. The paper presents, after a summary of the project, the main design features of the ELFR plant and of the demonstrator ALFRED (Advanced Lead Fast Reactor European Demonstrator). In particular, relevance is given to the description of the Reactors configuration and the main components such as Reactor Vessel, Steam Generator, Primary Pump and Decay Heat Removal System.

The Lead-cooled Fast Reactor (LFR) technology [2] has a great potential to fulfill all the main goals established by the "Generation IV International Forum" (GIF) for the next generation nuclear power plants. The LFR is based on a closed fuel cycle for efficient conversion of fertile uranium and management of actinides (enhanced sustainability), the inert nature of the coolant provides important design simplification (improved economics) and allows for designing decay heat removal systems based on well known light water technology and passive features (increased safety). Moreover, the reference LFR fuel (MOX) constitutes a very unattractive route for diversion or theft of weapons-usable materials and provides increased physical protection against acts of terrorism (Non-proliferation and Physical Protection).

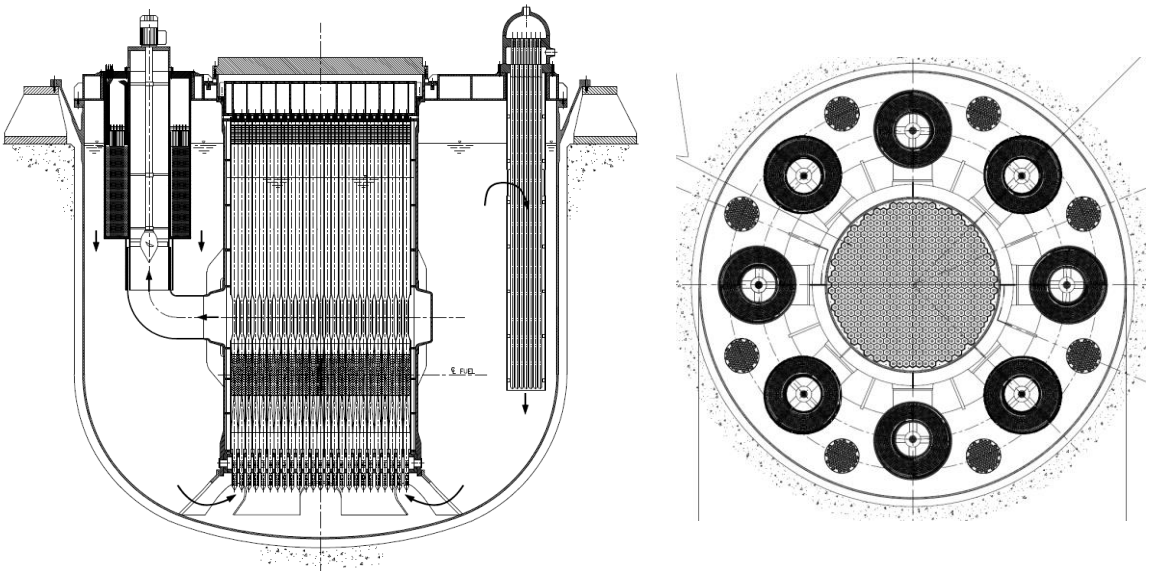

Figure 1 ELFR reactor block vertical section and plan view

ALFRED, in the role of LFR demonstrator, will show the viability of the LFR technology for

use in a future commercial power plant, being the first link of the technology chain connected to the electrical grid. It is expected to significantly reduce uncertainties in construction and licensing.

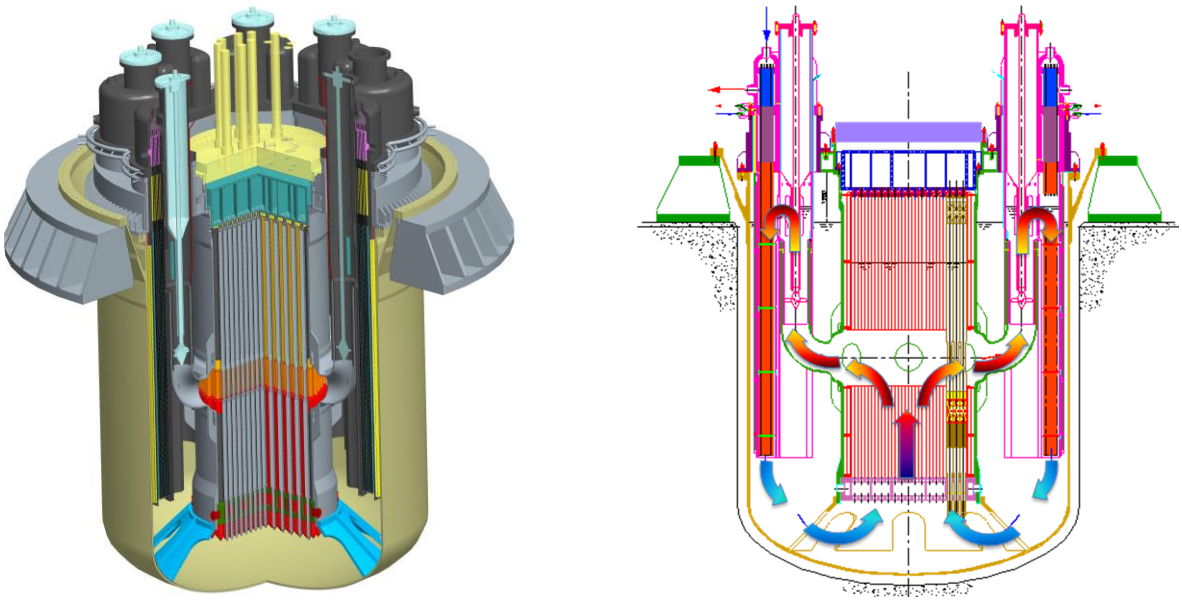

Figure 2 ALFRED 3-D sketch and reactor block vertical sections

References

[1] LEADER project, www.leader-FP7.eu

[2] L. Mansani et al., Lead-cooled system design and challenges in the frame of Generation IV international forum, *Journal of Nuclear Materials, Vol. 415, Issue 3, p.245-253 (2011).*

Issues and considerations for fuel cladding materials of ALFRED reactor

P.Agostini - ENEA

The Lead Fast Reactor presents, as any other reactor, several motivations for damage and eventually rupture of the steel structures. These damage modes have to be envisaged in order to select the right steels. The most critical area for the structural material is the fuel cladding, where high neutron flux, high temperature and harsh chemical environment affect the structural material that is subject to mechanical stress and deformation. The typical LFR damage modes in this area are: irradiation damage (swelling, creep, embrittlement), thermal creep, thermal fatigue, LM corrosion, LM embrittlement. Assuming as reference the ELSY design (First Of A Kind), the conditions are :

- Max allowed peak linear power 32kW/m;
- Max clad and fuel temperatures of 560 °C and 2100 °C, respectively;
- Max neutron flux $2.4*10^{15}$ n/cm^{2}s
- Peak clad damage of 100 dpa, in correspondence of a fuel burn-up of 100 MWd/kgHM;
- Hoop stress to be examined for creep 160 MPa
- Pure lead as coolant.

Irradiation swelling at the fast neutron spectrum was tested in Phenix (sodium) evidencing the good behaviour of F/M steels and of advanced austenitic steels. Also the creep characteristics of the two steel families are compared. The austenitic steels are shown to exhibit a better creep resistance. The reason for that is supposed to be linked with the void formation close to Laves phases (Fe2Mo). As for the creep rupture sensitivity, a significant effect is attributed to the liquid metal environment.

The fatigue resistance by grade 91 steel is limited by its reported softening after few cycling.

Both F/M and austenitic materials are resistant to irradiation embrittlment while the grade 91 is very prone to liquid metal embrittlement which take place at temperatures between 250 and 550°C (ductility trough). A welding issue arose for grade 91 due to the appearance of type four cracks in the fine grain HAZ under fatigue cycling.

An oxygen content in lead of E-06 weight % provides protection towards liquid metal corrosion through surface passivation up to 500°C for both steel categories. For higher temperatures the development of corrosion barriers is compulsory. In the short term (LFR Demonstrator), the reference material for fuel cladding is 15-15 Ti, Si stabilized, protected by a well qualified corrosion barrier. The potential candidates for corrosion barriers include : Fe-Al, TiN (BLUE), Al oxide, GESA, Ta and possibly others.

In the long term (First Of A Kind), corrosion resistant austenitic steels have to be selected and qualified for fuel cladding: Si or Al containing steels, advanced austenitic steels.

The next steps along the fuel cladding development are:

- Extensive testing campaign of steel corrosion barriers in controlled corrosion conditions
- Extensive testing campaign of steel corrosion barriers in HLM under stress and strain conditions
- PIE after irradiation tests performed in BOR 60 at 16 dpa
- Development of additional corrosion barriers for austenitic and F/M steels
- Qualification of corrosion resistant steels for cladding
- Collaborations to get irradiation data on advanced austenitic steels

An effective strategy for recycling all actinides: the adiabatic reactor concept

Giacomo Grasso[1]

[1] *Italian National Agency for New Technologies, Energy and Sustainable Economic Development (ENEA), v. Martiri di Monte Sole, 4, 40129 Bologna, Italy, e-mail: giacomo.grasso@enea.it*

The management of the transuranics – the main contributors to the long-term radio-toxicity of the high-level waste produced by nuclear reactors – represents the password for unlocking the concerns of society with regard to the implementation of nuclear energy.
As recognized by the European Community, the full closure of the fuel cycle, through the continuous recycling of all actinides in the spent fuel, would allow the fulfillment of the requirements for employing nuclear as a sustainable source of energy. By recycling all the actinides in the spent fuel, it would be simultaneously possible indeed to minimize the nuclear waste and optimally use the natural resources.
Through the European Sustainable Nuclear Industrial Initiative (ESNII), the European Community promotes the development of advanced Fast Reactors (FRs) able to implement the closure of the fuel cycle, giving body to a future generation of nuclear power plants which will add – to the pillars of safety, reliability, radiological protection, security and economics already proper of the state-of-the-art nuclear power plants presently available – also excellent sustainability performances. Which is what we call Generation IV.
All the candidate technologies under investigation in Europe nowadays (the Sodium-, Lead- and Gas-cooled Fast Reactors) have the potential to meet the criteria necessary for being included in a closed fuel cycle. All these technologies rely indeed on fast-spectrum reactors, in which the high energy of the neutrons allows for an effective conversion of fertile isotopes into fissile ones, as well as for a more efficient transmutation of the Minor Actinides (MAs) with respect to present generation systems (all based on thermal-spectrum reactors).
Nevertheless, the management of a MA-bearing fuel requires several design expedients, mainly to what concerns aspects related to the safety, during their entire life, of the reactors meant for operation with such fuel.
A promising solution consists in the adoption of the so called “adiabatic” reactor concept [1]: such a reactor would be able to operate being fed by either natural or depleted uranium and, through a reprocessing of the spent fuel aimed at the mere separation of the Fission Products (FPs) from the rest of the fuel, to continuously recycle the actinides while releasing as final waste only the fission products (Figure 1). More in detail, an adiabatic reactor is operated in its extended equilibrium state, that is: with an isotopic composition of the fuel such to reverberate exactly every fission to uranium only, maintaining the inventory of all other isotopes – during the whole life of the fuel, from irradiation to cooling, from reprocessing to re-fabrication – constant (including the unavoidable reprocessing losses).

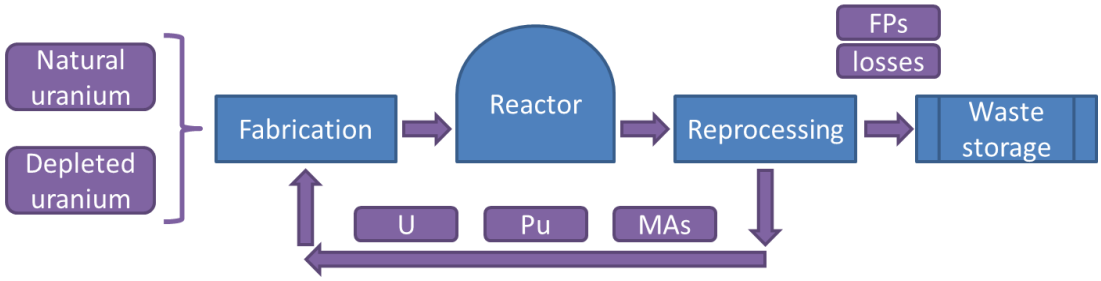

Fig. 1. Scheme of closed fuel cycle implementing an adiabatic reactor.

The main feature of this concept, is the evaluation of this equilibrium fuel beforehand, being only function of the neutron spectrum in the fuel and of the in-pile and out-of-pile residence times. Through a simple reversion in the logical scheme used to approach the design of a new reactor, the designer is allowed to cope with the adiabatic operation of the reactor to be conceived since the beginning of the design process itself.
This feature introduces the possibility to simply embed in the design of the reactor all the provisions required for the management not only of the equilibrium fuel itself, but also of the transition from the start-up core (which might be initially loaded with simple U-Pu fuel) to the equilibrium one, hardening the safety and robustness of the reactor.
The results of the application of this design strategy to the core of the European Lead-cooled Fast Reactor (the reference lead-cooled system candidate in ESNII for a European fleet of Generation-IV FRs) seem to promise excellent perspectives for a sustainable implementation of nuclear energy.

References

[1] C. Artioli, G. Grasso and C. Petrovich, A new paradigm for core design aimed at the sustainability of nuclear energy: The solution of the extended equilibrium state, *Ann. Nucl. En.* **37**, 915 (2010).

The strategic project INFN-E

M. Ripani

INFN Genova Italy

INFN mission is to carry on programs in fundamental science. However, the broad competences on basic theoretical aspects, accelerator design, construction and operation, radiation/particle detector design, construction and operation can be applied to topics like management of waste storage sites, industrial and public safety, port security, reactor monitoring, new generation fission systems (ADS and fast reactors) and the fusion program. Therefore, besides contributions to the medical field and the study of the cultural heritage, INFN can contribute to this field, too.
In this presentation, I will illustrate how the INFN-E strategic project helps in developing R&D activities on several topics and in seeking further funding through the European Union or other agencies and in seeking partnerships with industries. In the framework of nuclear safety and security, research is performed on innovative systems and instrumentation for radiation monitoring with applications to waste storage sites, port security and radiation surveys. In the framework of fission, research is performed on neutron physics aspects in fast reactors, Accelerator Driven Systems, transmutation of nuclear waste and innovative neutron detectors. In the framework of fusion, research is performed on the neutral beam injection technique to heat the plasma, accelerators for material irradiation and again innovative neutron detectors.

Journées des Actinides : 40 years in perspective

Jean-Marc Fournier[1]

[1] *Le Grangeon, 26220 Dieulefit, France ,e-mail: jean-marc.fournier@orange.*

The "Journées des Actinides" exist now since more than 40 years.
It has become the (incontournable) yearly informal meeting aside congresses for scientific people interested in pure and applied research in the different fields related to Actinides.
Remembering that plutonium was discover only 70 years ago, it becomes obvious that they cover a large part of the scientific story of the Actinides.
After recalling the why and how of their creation, we will briefly recall some scientific highlights of their first decade of existence.

Looking back over 40 years on the actinide dioxides

G. H. Lander

European Commission, Joint Research Centre, Institute for Transuranium Elements, Postfach 2340, D-76125 Karlsruhe, Germany

Since the actinide oxides became the choice for nuclear fuels in the 1950s, there has been great interest in understanding all physical properties and the associated electronic structure of these materials. One would think that with a clear O^{2-} ion the actinide ion would be An^{4+} and the interpretation of the measurements would be simple and taught in kindergartens. Alas, this was not to be.

The JdA's started 40 years ago, and even by that time many properties of the oxides were measured, and some idea of the complexity of the task of understanding them was beginning to dawn on those involved. For example, Osborne and Westrum at ANL had measured the specific heat of UO_2 and NpO_2 in 1953, and a large peak at 25 K in NpO_2 suggested a magnetic ground state, but neutron experiments in 1967 failed to find any microscopic evidence for such an ordered moment, which had been seen earlier in UO_2. Likewise, the phonons and magnons of UO_2 were measured at Chalk River by Dolling & Cowley in the late 1960s, and, at least for the magnons, the interpretation appeared extremely complex, despite the apparent simple antiferromagnetic structure.

We started experiments at ANL in 1973 that led, by accident, to the discovery of the internal distortion in UO_2 for $T < T_N$. Once one starts on these materials, they have a long-term fascination bordering, perhaps, on an obsession!

In this talk I shall try and look back over our understanding of the actinide oxides over this period. Many many talks were given on these systems in the JdA's, and many people have been involved. Solutions to most, but not all, of the problems have come in the last decade. In the case of the mysterious transition in NpO_2 it took a half-century to elucidate.

I would especially like to thank Roberto Caciuffo and Giuseppe Amoretti for a long-term friendship and a sharing of the obsession for the electronic structure of the actinide oxides. Many others have contributed significantly, such as the authors of Ref. [1].

References

[1] Paolo Santini, Stefano Carretta, and Giuseppe Amoretti, Roberto Caciuffo, Nicola Magnani, and GHL, *Rev. Mod. Phys.* **81**, 807 (2009)

Historical view of the studies of actinide compounds

Robert Troć

W. Trzebiatowski Institute of Low Temperature and Structure Research, P.O. Box 1410, 50-950 Wrocław 2, Poland, e-mail: R.Troc@int.pan.wroc.pl

As the long lasted basic investigations have pointed out, the interest in actinide compounds is due to not only their nuclear properties but it is also equally important in the studies of the electronic and numerous related behaviours, as magnetic, electrical and thermal ones. The richness of specific phenomena taking place in actinide compounds, like exotic magnetic structures, complex transitions found in studies of the magnetic phase diagrams (MPDs) driven by doping and forming complete solid solutions and by changing temperatures, magnetic field and pressure. Furthermore, the observation of low temperature transformation to heavy fermion state (HFS) and an appearance of unconventional superconductivity, dipolar and quadrupolar Kondo effects, high-order multipolar interactions, magnetic and valence fluctuations, strong magneto-elastic effects and others, all these phenomena are ascribed to the specific role of the $5f^n$ electrons ($n \geq 2$) which they play in such binary and ternary actinide compounds. This specific their role is e.g. behaviours ranging from being mostly localized to typical band-like ones. Moreover, as shown in the last decade, there is also possible their *dual* state where both these kinds of behaviours, i.e. localized and itinerant, occur simultaneously. The former has to be treated with regard to the influence of crystal field (CF) and strong magnetic exchange interactions, both leading to rising different ground states of an actinide atom with forming a large variety of different types of magnetic structures (see e.g. Fig. 1), while the latter gives rise to many types of band structures obtained by using various methods of calculations. In contrast to strictly localized character of 4f shell in lanthanides, especially the 5f electrons in ternary compounds of early actinides can more or less hybridize with those of neighbouring ligands and provide some contribution to chemical bonding. The complexity of the 5f electron behaviour is then solved with some success by intense different types of spectroscopies. All this huge richness in various physical and chemical properties of actinide compounds, well known today, have some beginning, which may be dated about 60 years ago. Thus, I would like just to devote my talk to this very beginning and the following steps, first of all concerning the magnetic properties of some selected uranium compounds.

In late 1940s the problem of an electronic structure of the actinides was in its completely initial stage and was a subject of speculations. The carried out very limited experiments provided arguments in favour of both the 6d electron (transition metal like) and 5f electron (lanthanide like) concepts. This happens due to an intermediate nature of the 5f shell between these two concepts. For example, it turned out that the effective moment in UO_2, infinite diluted by ThO_2, is equal to 2.83 μ_B, i.e. exactly as a value that corresponds to the "spin-only" value of the $6d^2$ electron configuration of the U^{4+} ion. This suggested a 6d-like magnetism of the uranium in UO_2. However, somewhat later *Hutchinson and Candella* (for refs. see [1]) found that the same value can be obtained for the case $5f^2$ electron configuration for U^{4+}, placed in the tetrahedral CF potential. In years 1950-1952 *Trzebiatowski* and his co-workers discovered a ferromagnetic transitions in β-UH_3 and β-UD_3 at 174 and 172 K, respectively [1]. This discovery was a complete surprise, because uranium as an actinide metal had already been known to be a Pauli paramagnet. Moreover, that time only several metals and alloys from the iron group of Periodic Table and also the Gd metal were the only known ferromagnets. Despite this large surprise, shortly after publication by *Trzebiatowski et al.* these data in 1954 some other laboratories have confirmed this unexpected fact.

Soon after this discovery, at the same laboratory in Wrocław, the ferromagnets: monochalcogenides U(S;Se;Te), sesquichalcogenides and sesquipnictides U_2Te_3, β-U_2N_3, $U_3(P;As;Sb;Bi)_4$ and antiferromagnets: oxy-telluride UOTe, monopnictides U(N;P;As;Sb;Bi), di-pnictides $U(P;As;S;Bi)_2$ were reported (see refs. [2] in the form of Landolt-Boernstein books). An associated important event was also the obtaining for the first time numerous single crystals by using either chemical transport or van Arkel methods. Next, but not earlier than at the end of sixties, all these families of uranium compounds became a main research interest of several laboratories in the world. One of the special interest was put in studying the MPDs between the monopnictides and monochalcogenides of uranium and thorium. A very detail study of the solid solutions, e.g. between complete mixed UP – US and UAs – USe pairs have indicated an arising of a great deal of exotic types of magnetic structures during the transformation from antiferromagnetism to ferromagnetism by variation of compositions. Based on such data, Fig. 1 shows a complete magnetic diagram (CMPD) by taking into account these monocompounds of uranium and thorium in the form of different solid solutions. The lined area marked in this CMPD show the existence of intermediate complex magnetic structures of both kinds anti- and ferrimagnetic ones.

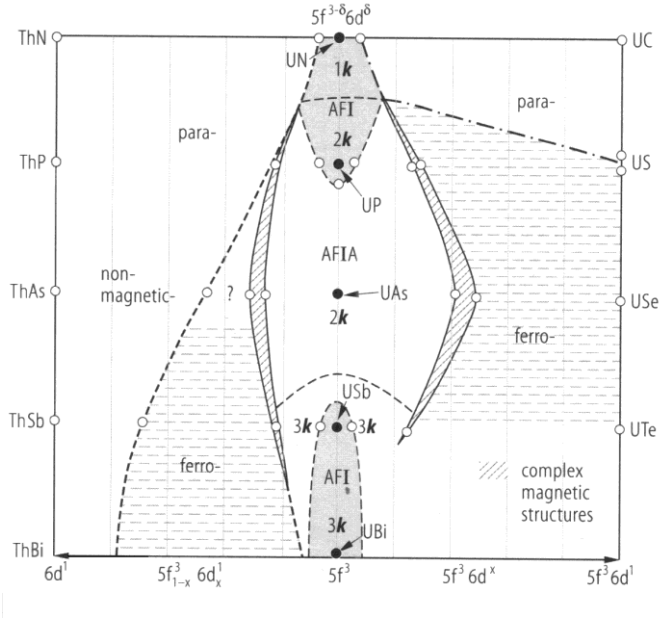

Fig. 1. The magnetic properties of solid solutions between different uranium and thorium monocompounds [2B].

All these uranium monocompounds and also those with higher stoichiometry follow the so-called Hill law, i.e. their transition temperatures T_C or T_N depend smoothly on the magnetic atom distances in various crystal structures. Otherwise situation is in the case of uranium binary and ternary systems, containing a transition metal, which have been widely explored more recently. This, however, requires a quite separate description (no LB's books exist).

References:

[1] R. Troć and W. Suski, *J. Alloy Compd.* **219,** 1-5 (1995).

[2] Landolt-Börnstein, New Series, Group III Vol. 27, Condensed Matter: A. (B6α) R. Troć, *Actinide monopnictides*; B. (B6β) R. Troć, *Actinide monochalcogenides*; C. (B7) D. Kaczorowski and R. Troć, *Binary actinide pnictides and chalcogenides*; D. (B8) D. Kaczorowski, *Ternary actinide pnictides and chalcogenides*.

Localized versus itinerant: Towards the limits.

P. Wachter

Laboratorium für Festkörperphysik, ETH Zürich, 8093 Zürich, Switzerland

Modern band structure calculations (2010) using the density functional theory still cannot treat localized and itinerant band states within the same theory. Localized states are treated as waves and thus have a certain band width. Experimentally there is practically no information about the width of localized states. Best example is Gd doped LaSb where it can be shown that the width of the Gd ground state is less than 0.14 meV. But is a 4f band possible? Yes, by admixing 5d wave functions a 4f band of 30 meV can be produced and will be described. Light actinide compounds have 5f widths of eV size, but how is the transition to localized states towards Cm? Pu chalcogenides are intermediate valent and have hybridized 5f bands in the meV range. But AmTe is integer divalent without 6d hybridization. Divalent Am is the famous $5f^7$state, a highly magnetic state. Nevertheless this compound has only a temperature independent Pauli paramagnetism. We show that the 5f band has only 24 meV width and is half filled with the 7 f electrons. Elastic properties are presented for the light actinides until AmTe.

Electronic properties of γ-U and superconductivity of U-Mo alloys

L. Havela[1], I. Tkach[1], N.-T.H. Kim-Ngan[2], S. Mašková[1], A.P. Gonçalves[3], A. Warren[4], T. Scott[4]

[1] *Faculty of Mathematics and Physics, Charles University, Ke Karlovu 5, 12116, Prague, Czech Republic, e-mail: havela@mag.mff.cuni.cz*
[2] *Institute of Physics, Pedagogical University, Podchorazych 2, 30-084 Krakow, Poland*
[3] *IST/ITN, Instituto Superior Técnico, UTL, CFMC-UL, Estrada Nacional 10, 2686-953-Sacavém, Portugal*
[4] *Interface Analysis Centre, University of Bristol, Oldbury House, Bristol, BS2 8BQ, United Kingdom*

Mo alloying leads to stabilization of the high-temperature *bcc* γ-U structure to low temperatures [1]. Using Mo doping in conjunction with splat-cooling technique allows to obtain single-phase *bcc* material (with tetragonal distortion not exceeding 3% in the range 12-12.5% Mo) for as low as 12% Mo. Lower Mo concentrations yield a bi-phase material, where the orthorhombic and *bcc* phases coexist. We have investigated low-*T* properties as a function of Mo concentration.

Magnetic susceptibility remains *T*-independent and very weakly increasing if normalized per mole U (Fig.1). In contrast with that, the Sommerfeld coefficient γ (Fig.2) increases from 11 mJ/mol K^2 for pure U to 16 mJ/mol K^2 for 15% Mo (i.e. 18.8 mJ/mol U K^2), which probably reflects the lattice expansion (≈3%) of the *bcc* phase. Fig.2 also reveals that the Debye temperature is lower in the *bcc* phase (139 K comparing to 179 K).

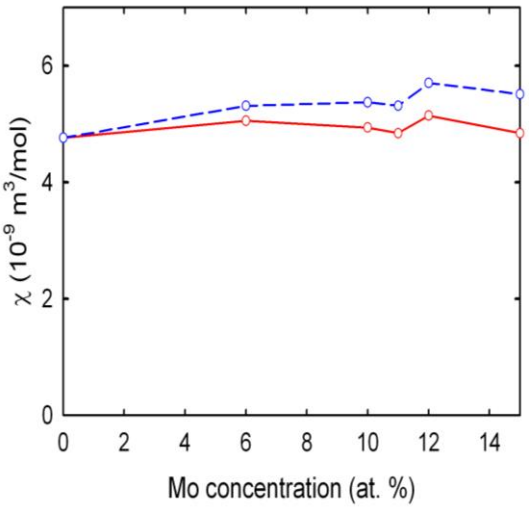

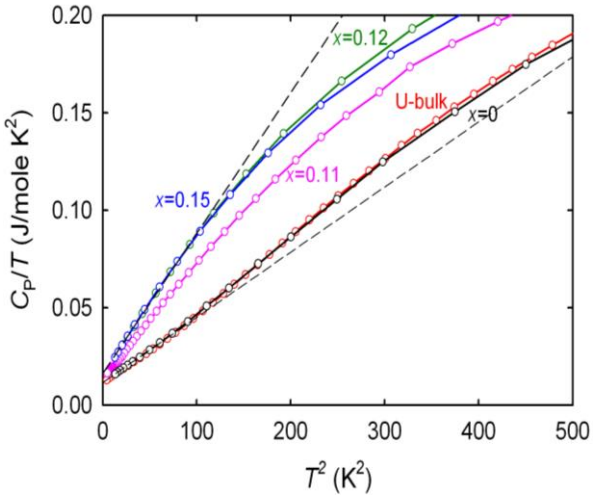

Temperature dependence of electrical resistivity of $UH_3Mo_{0.18}$ exhibits a negative slope ($d\rho/dT < 0$) (fig. 4) similar to γ-phase U-Mo alloys [1]. Its reason can be seen in the weak localization, which appears under conditions of strong disorder, and which i

One of the most interesting issues is the superconductivity, noticed for U-Mo alloys long ago and then almost forgotten. The highest critical temperature T_c = 2.1 K agrees with that reported in [2], the disagreement for low Mo concentrations (Fig.3) can be explained by different metallurgy (splats compared with bulk). The superconductivity can be classified as

BCS superconductivity, with $\Delta C = C_s - C_n \approx 1.43 * \gamma Tc$ (Fig.4). The superconductivity of pure U splats also exhibits superconductivity ($\rho = 0$ at $T = 1.2$ K), but its very small fingerprint in specific heat (Fig.4) confirms the non-bulk character, suggested in [3]. The superconductivity of the U-Mo alloys exhibits rather high upper critical field at $T = 0$, $H_{c2}(0)$, exceeding 5 T in some cases. The situation is similar to superconductors as U_6Fe [4]. As seen from Fig.5, pure U superconductivity is much less field resistant.

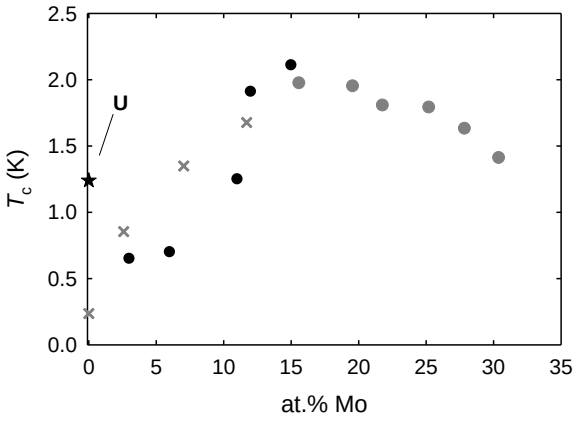

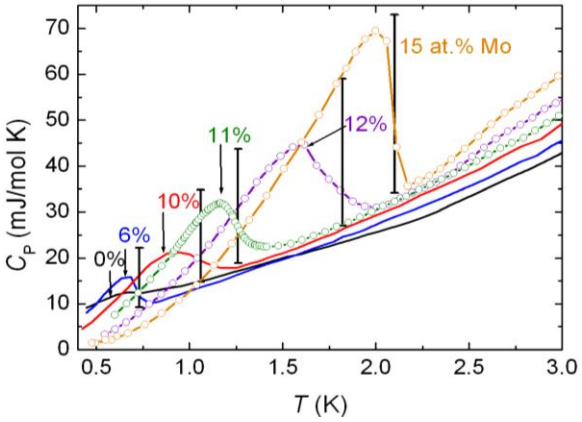

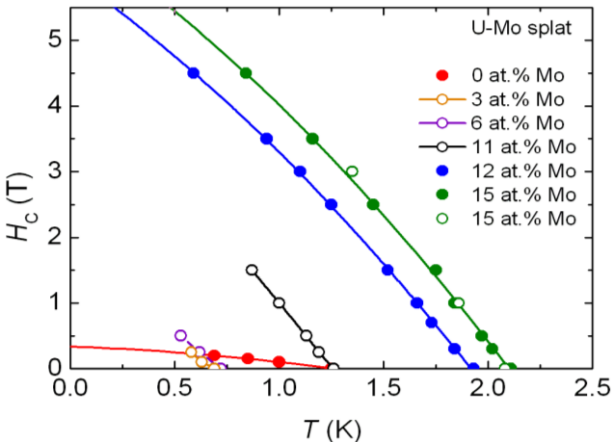

References

[1] I. Tkach et al., *J.Alloys Comp.* **101-109**, 534 (2012).
[2] B.S. Chandrasekhar, J.K. Hulm, *J.Phys.Chem.Solids* **7**, 259 (1958).
[3] D. Graf et al., *Phys.Rev. B* **80**, 241101 (2009).
[4] L.E. DeLong et al., *Physica* **135B**, 81 (1985).

HRTEM studies on the UCoGe ferromagnetic superconductor

A.P. Gonçalves,[1] M.S. Henriques [1], E.B. Lopes [1], L.C.J. Pereira [1], A. Janssen [2], T. Wiss [2], L. Havela[3]

[1] *IST/ITN, Technical University of Lisbon, CFMC-UL, 2686-953-Sacavém, Portugal, e-mail: apg@ctn.ist.utl.pt*
[2] *European Commission, Joint Research Centre, Institute for Transuranium Elements, P.O. Box 2340, D-76125 Karlsruhe, Germany*
[3] *Dept. Condensed Matter Physics, Faculty of Mathematics and Physics, Charles University 121 16 Prague, The Czech Republic*

The discovery of superconductivity at high pressures in the UGe_2 [1] ferromagnetic compound, followed by the discovery of superconductivity in the URhGe [2] and UCoGe [3] ferromagnets at ambient pressure, led to the question about the dominant mechanism responsible for the pairing and the exact symmetry of the paired state in these systems. It was first argued that on the borderline of the zero temperature transition from a paramagnetic to a ferromagnetic phase critical magnetic fluctuations emerge, which could mediate the superconductivity by pairing the electrons in triplet states. However, later works indicate a more intricate mechanism in which the superconductivity in UGe_2 and URhGe is driven by a magnetic transition between two polarized phases. In the case of UCoGe, the superconductivity seems to occur on the borderline of the ferromagnetic ordering, which points to a pairing stimulated by critical fluctuations associated with a ferromagnetic quantum critical point [3]. The physical properties of UCoGe seem to be extremely sensitive to heat treatments [3, 4], but not so much to small variations in composition [5]. Although, no studies on the microscopic origin of this behavior, in particular the role of nano-precipitates, vacancies, defects and composition inhomogeneities, have been made. Here we present the high-resolution transmission electron microscopy (HRTEM) investigation of UCoGe samples subjected to different heat treatments.

A UCoGe sample was pulled from a charge with $U_{1.01}CoGe$ nominal composition by using the Czochralski method. The compositional homogeneity along the pulled material was confirmed by microanalysis. Homogeneous pieces of UCoGe taken from the middle region of the pulled material were cut and submitted to heat treatments at 750ºC, 900ºC and 1100ºC for one week.

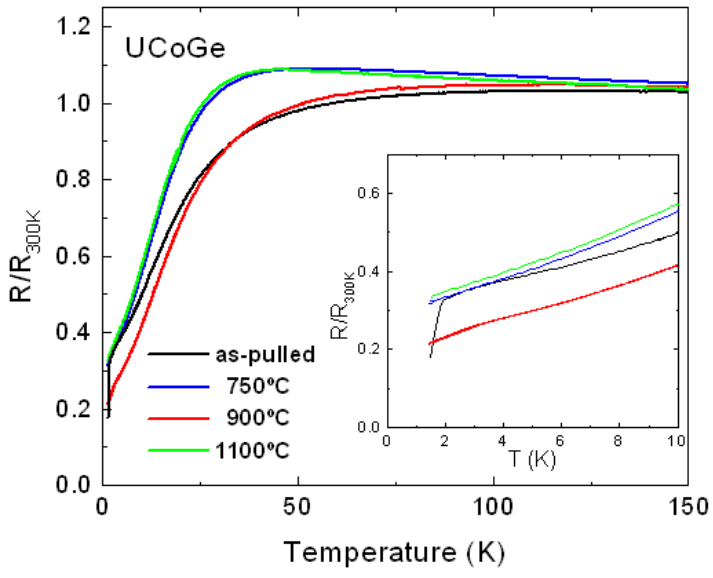

Fig. 1. Electrical resistivity ratio versus temperature of the

The physical characterization of the samples has shown that different annealing temperatures affect their properties. Electrical resistivity measurements (down to 1.5 K) indicate a maximum residual resistivity ratio (RRR = R(300 K)/R(2 K)) of ~5 for the sample annealed at 900ºC. However, a significant drop, of ~55%, on the electrical resistivity is observed in the as-pulled material below 2 K, which is most probably related with the

ferromagnetic ordering. Nevertheless, low temperature magnetization measurements also show a small ferromagnetic component on the other samples.

The HRTEM study was made in the same pieces used in the physical properties characterization. The samples were obtained by crushing part of the crystalline pieces inside ethanol. A drop containing small grains transparent to electrons was placed onto carbon reinforced holey micro grids and dried in air.

The as-pulled sample shows a high degree of defects, as disorder, stacking faults and misalignments, which are also evidenced by the large number of Moire fringes observed in the TEM images. The increase of the annealing temperature seems to decrease the number of such defects, with the material heat-treated at 750ºC still showing TEM images similar to the as-pulled material, but the sample annealed at 1100ºC presenting a high degree of long-range ordering. Interestingly, HRTEM observations show that the sample heat-treated at 900ºC has a much higher number of nano-domains, with 4-10 nm typical diameters, when compared with the other materials, which is most probably related with the higher RRR presented by this sample.

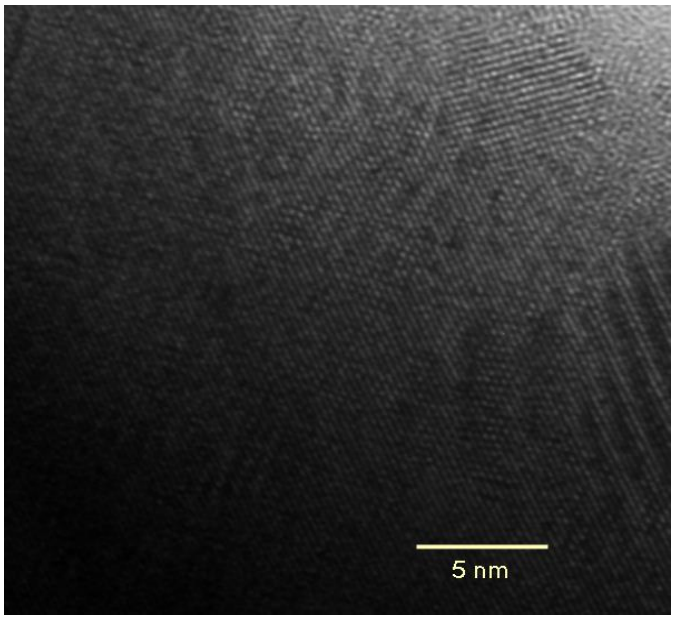

Fig. 2. HRTEM image of the UCoGe as-pulled material, evidencing a large number of defects.

Acknowledgments

This work was partially supported by the ACTINET-I3 project with Contract Number 232631, by FCT, Portugal, under the contract No. CERN/FP/123588/2011, and by the FCT-ASCR 2012 bilateral collaboration between Portugal and the Czech Republic. M.S.H. would also like to acknowledge the SFRH/BD/66161/2009 support.

References

[1] S.S. Saxena et al., Nature 406 (2000) 587
[2] D. Aoki et al., Nature 413 (2001) 613
[3] N.T. Huy et al., Phys. Rev. Lett. 99 (2007) 067006
[4] N.T. Huy, D.E. de Nijs, Y.K. Huang, A. de Visser, Phys. Rev. Lett. 100(2008) 077002
[5] D.E. de Nijs, N. T. Huy, A. de Visser, Phys. Rev. B 77 (2008) 140506(R)

Superconductivity and Mössbauer effect in actinides

A. Hen,[1,2] I. Halevy,[2,3,4] I. Orion,[2] E. Colineau,[1] R. Eloirdi,[1] J.-C. Griveau,[1] P. Gaczyński,[1] T. Klimczuk,[1] J.-P. Sanchez,[5] A. B. Shick,[1,6] and R. Caciuffo[1]

[1]*European Commission, Joint Research Centre, Institute for Transuranium Elements, Postfach 2340, D-76125 Karlsruhe, Germany*
E-mail: amir.hen@mail.huji.ac.il
[2]*Nuclear Engineering Department, Ben Gurion University, IL84105 Beer-Sheva, Israel*
[3]*Physics Department, Nuclear Research Center Negev, P.O. Box 9001, IL84190 Beer-Sheva, Israel*
[4]*California Institute of Technology, W. M. Keck Laboratory 138-78, Pasadena, California 91125, USA*
[5]*SPSMS, UMR-E CEA/UJF-Grenoble 1, INAC, FR-38054 Grenoble, France*
[6]*Institute of Physics, Academy of Sciences of the Czech Republic, Na Slovance 2, CZ-182 21 Prague, Czech Republic*

Superconductivity, discovered more than 100 years ago [1] still remains challenging for condensed matter physics, 50 years after the BCS theory on superconductivity [2].
In particular, the existence of heavy fermion superconductivity and its coexistence or proximity with magnetic order suggests that the conventional mechanism of phonon-mediated superconductivity is inappropriate and that alternative mechanisms, like spin fluctuations, should be considered for Cooper pairing.
Actinide materials and their 5f electrons are the main players in this important field, with a large number of uranium heavy fermion magnetic superconductors reported in the last three decades [3] and, more recently, transuranium unconventional superconductors : $PuCoGa_5$ [4], $PuRhGa_5$ [5], $PuCoIn_5$ [6] and $NpPd_5Al_2$ [7].

Mössbauer effect [8] has been used for more than 50 years as a unique tool for probing individual ions within compounds giving an insight on the chemical, electronic and magnetic properties of compounds, with a hyperfine energy resolution ($1.986 \cdot 10^{-7}$ eV for 1 mm/s in ^{237}Np). Mössbauer spectroscopy has many applications and is in particular a powerful tool in solid state physics. However, its use in superconductivity on one hand and in actinide materials on the other hand, has been limited [9]. Mössbauer effect can be observed in a number of actinide isotopes, however only the 60 keV electric dipole (E1) transition of the ^{237}Np isotope is suitable for systematic investigations, combining reasonable experimental constraints and exploitable output parameters [10]. Indeed, the excellent Mössbauer resonance of the ^{237}Np nucleus makes it a unique microscopic tool for gaining information on the electronic and magnetic properties of Np systems [11].

The paramagnetic heavy fermion $NpPd_5Al_2$ (T_c = 4.9K and γ = 200 mJ mole^{-1} K^{-2}) is the only neptunium-based superconductor known so far [7]. This system thus represents a unique opportunity for ^{237}Np Mössbauer spectroscopy. No magnetic hyperfine splitting is observed, indicating that the Np ions do not carry any ordered magnetic moments [11]. The isomer shift ($\delta_{IS} \approx$ -11.1 mm/s vs $NpAl_2$) is close to the value expected for ionic Np^{4+}, but attributed rather to Np^{3+} (configuration $5f^4$), after considering the influence of conduction electrons. The spectra recorded in the superconducting state are very similar to those taken in the normal state. However, a small increase in both δ_{IS} and the quadrupolar interaction parameter e^2qQ is observed below T_c, indicating that both the electronic density at the Np nuclei and the electric field gradient due to the *5f* electrons are affected by the formation of Cooper pairs.

A recent novel model has predicted a possible temperature-dependence with an extremum of the charge density in $NpPd_5Al_2$ (Fig.1, left) [13]. In order to check this behaviour, we have measured the temperature dependence of the isomer shift of $NpPd_5Al_2$ with the best experimental accuracy possible and found a small extremum (Fig.1, right). We report here on these new measurements of the isomer shift and their connection to the theoretical prediction for the related charge density.

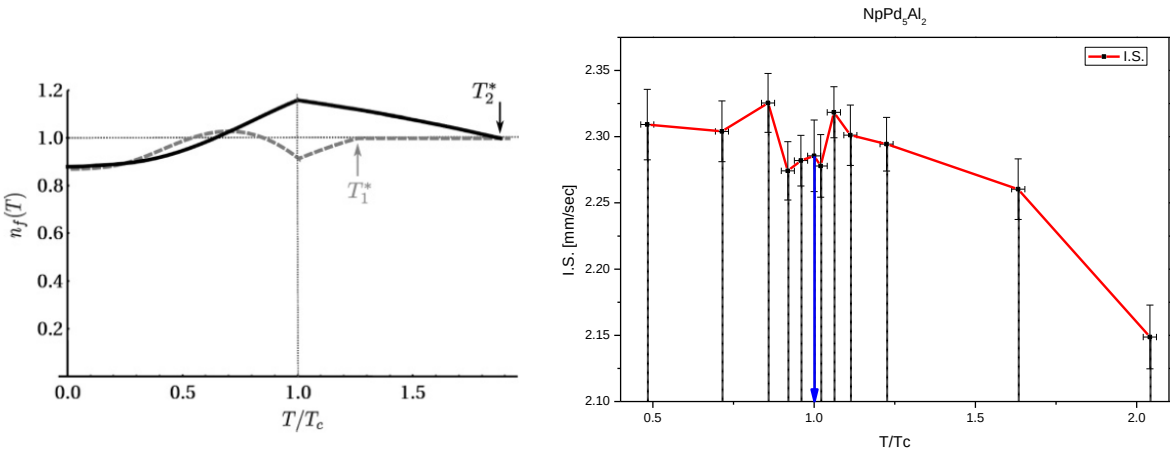

Fig.1: Left: The *f* -electron valence n_f changes as a function of normalized temperature. The black curve is predicted for $NpPd_5Al_2$, the dashed gray curve predicted for $CeMIn_5$ (From ref. [13])
Right: Isomer shift as a function of normalized temperature for $NpPd_5Al_2$, blue arrow indicates T_C (4.9 K), red line is a guide for the eyes.

Acknowledgements

The high purity Np metals required for the fabrication of the compound were made available through a loan agreement between Lawrence Livermore National Laboratory and ITU, in the frame of a collaboration involving LLNL, Los Alamos National Laboratory and the US Department of Energy.

References

[1] H. K. Onnes, Commun. Phys. Lab. Univ. Leiden 120b, 122b, 124c (1911).
[2] J. Bardeen et al. , Phys. Rev. **108**, 1175 (1957).
[3] P.S. Riseborough et al, in: Superconductivity, Springer, Ed. K.H. Bennemann and J.B. Ketterson pp 1031-1154 (2008).
[4] J.L. Sarrao et al., Nature **420**, 297 (2002).
[5] F. Wastin et al., J. Phys.: Condens. Matter **15**, S2279 (2003).
[6] E.D. Bauer et al., J. Phys.: Condens. Matter **24**, 052206 (2012).
[7] D. Aoki et al., J. Phys. Soc. Jpn. **76**, 063701 (2007).
[8] R.L. Mössbauer., Zeitschrift für Physik, Bd. **151**, S. 124-143 (1958).
[9] E. Colineau et al., Hyperfine Interact. **207**, 113 (2012)].
[10] G.M. Kalvius, J. Nucl. Mater. 166 (1989) 5
[11] J.-P. Sanchez et al., J. Alloys Comp. 275 (1998) 154
[12] K. Gofryk et al., Phys. Rev. **B 79**, 134525 (2009)
[13] R. Flint et al., Phys. Rev. B **84**, 064514 (2011)

Electronic structure and magnetic properties of NpFeAsO and PuFeAsO

A. B. Shick,[1,2] T. Klimczuk,[2,3] R. Eloirdi,[2] E. Colineau,[2] J.-C. Griveau,[2] and R. Caciuffo[2]

[1] *Institute of Physics, ASCR, Na Slovance 2, 182 21, Prague, Czech Republic, e-mail: shick@fzu.cz*

[2] *European Commission, JRC, Institute for Transuranium Elements, Postfach 2340, 76125 Karlsruhe, Germany*

[3] *Faculty of Applied Physics and Mathematics, Gdansk University of Technology, Narutowicza 11/12, 80-952 Gdansk, Poland*

A huge volume of research has resulted from the recent discovery of superconductivity [1] in the *R*FeAsO series of compounds (where *R* represents a rare-earth element) characterized by its atomic-like 4*f* electrons. The replacement of this species by a member of the actinide series presents an exciting opportunity to study the effect of varying electron correlation. The successful substitution with actinides to form the *An*FeAsO parent compounds (where *An*=Np,Pu) has already been reported [2,3]. For both NpFeAsO and PuFeAsO materials, the anti-ferromagnetic (AF) order occurs at critical temperatures T_N , 57 K (Np) and 50 K (Pu). In sharp contrast to the rare-earth analogs, no tetragonal-to-orthorhombic distortion is found. Instead, the negative thermal expansion (-0.2%) – an Invar behavior - is found in NpFeAsO below T_N.

Here, we present the results of the first-principles electronic structure calculations for the actinide-based oxypnictides, NpFeAsO and PuFeAsO, and make the comparison with the bulk experimental data. We used the full-potential LAPW method (FP-LAPW) which includes all relativistic effects (scalar-relativistic and spin-orbit coupling), and relativistic version of the rotationally invariant LSDA+*U* method.

For both NpFeAsO and PuFeAsO, LSDA+*U* yields the lowest energy AF ground state. For NpFeAsO compound, the calculated value of the total magnetic moment M_J = 2.05 μ_B (the sum of spin M_S = -2.98 μ_B, and orbital M_L = 5.03 μ_B moments) on the Np atom is found in reasonable agreement with experimental value of 1.7 μ_B for U= 3 eV. The Fe atom carries the moment M_J = 0.11 μ_B , and there are no noticeable moments on the As and O atoms. For PuFeAsO compound, the total magnetic moment M_J = 0.41 μ_B (the M_S = -3.65 μ_B, and orbital M_L = 4.06 μ_B moments) on the Pu atom is calculated for U= 4 eV. The Fe atom has the moment M_J = 0.54 μ_B , and there are no noticeable moments on the As and O atoms.

Fig. 1 shows the total and partial (atom/spin/orbital resolved) density of states (DOS) for NpFeAsO. The total DOS at E_F corresponds to the Sommerfeld coefficient γ value of 5.6 mJ/K^{2}mol, smaller than the experimental γ of 75 mJ/K^{2}mol. The DOS near E_F has mostly Fe-*d* character. The Np-*f* states are split by exchange interaction. The As and O *p* states are located in the energy region 2-7 eV below E_F . For PuFeAsO, the DOS is similar: the Pu *f* states are exchange interaction split, and the γ coefficient value of 4.7 mJ/K^{2}mol is in good agreement with the experimental value of 4 mJ/K^{2}mol.

The Fermi Surfaces (FS) of NpFeAsO and PuFeAsO consist of five sheets, each of them doubly degenerate. Examination of the band structure shows that FS-1-3 sheets are hole-like, and centered at the Γ-point. The FS-4 and FS-5 are electron-like and centered at the M-A line. Note the fairly two dimensional character of the FS, and the strong resemblance to those previously presented for *R*FeAsO. Most of the states in the vicinity of the FS are located near Γ-[0,0,0] and M-[π,π,0] k-points in the BZ suggesting the possibility of s +/- superconducting pairing mechanism.

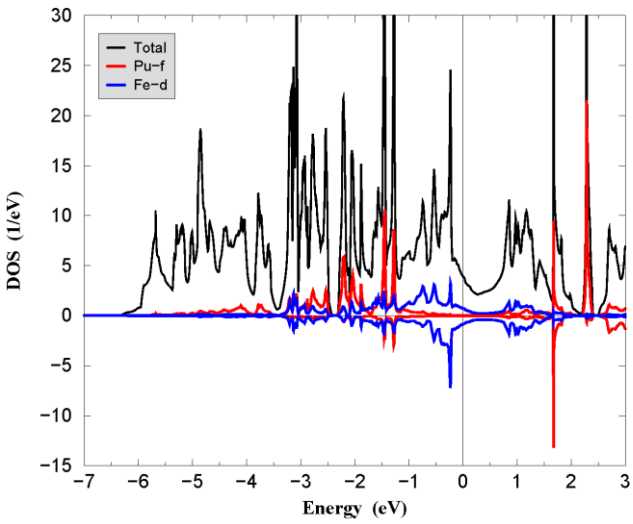

Fig. 1. Electronic structure calculations for NpFeAsO: the total DOS [per unit cell] and atom/spin/orbital resolved DOS calculated using LSDA+U = 3 eV.

In order to understand the absence of the orthorhombic structural distortion associated with the magnetic ordering, we performed magnetic anisotropy energy (MAE) calculations, rotating the staggered AF magnetization from the *c*-axis to the *a*-axis direction. What we found is that the total energy difference $E[a]$-$E[c]$ between these two directions of the magnetization is of ~30.0 meV/f.u. This means that there is a strong positive uniaxial MAE in NpFeAsO. This MAE keeps the staggered AF magnetization along the tetragonal *c*-axis and assists in the prevention of any distortion in the *a*-*b*-plane.

We used the LDA+Hubbard I approximation (LDA+HIA), to treat the paramagnetic (PM) phase of NpFeAsO with the local moments on the Np-atoms, and to analyse the negative thermal expansion (NTE). These calculations yield the effective paramagnetic moment of 2.84 μ_B per Np atom calculated in very good agreement with the moment of ~2.78 μ_B obtained from magnetic susceptibility measurements.

As follows from the total energy calculations, the resulting LSDA+U equilibrium volume of 120 Å^3 is in reasonable agreement with experimental 124 Å^3 volume. The LDA+HIA equilibrium volume of 116 Å^3 is calculated. Thus the volume of AF phase exceeds the PM phase volume by 3 %, in semi-quantitative agreement with experimental value (0.2 %).

Acknowledgements

The authors are grateful to L. Havela for helpful comments. The support from Czech Republic Grant GACR P204/10/0330 is thankfully acknowledged.

References

[1] Y. Kamihara et al., J. Am. Chem. Soc. **128**, 10012 (2006).
[2] T. Klimczuk et al., Phys. Rev. **B 85,** 174506 (2012).
[3] T. Klimczuk et al., Phys. Rev. **B 86,** 174510 (2012).

Preliminary investigations on the new compound NpRuGe

E. Colineau, J.-C. Griveau, R. Eloirdi, R. Caciuffo

European Commission, Joint Research Centre, Institute for Transuranium Element, Postfach 2340, 76125 Karlsruhe, Germany, e-mail:eric.colineau@ec.europa.eu

In the UTGe isostructural series, the tendency to magnetic ordering decreases as hybridization increases [1]. This can be illustrated by plotting the ordering temperature as a function of T element scanned from bottom to top and right to left in the periodic table (Fig.1). The ordering temperature drops from UPtGe to UIrGe and the weak ferromagnets URhGe [2] and UCoGe [3] are in the region where the magnetism collapses and superconductivity appears. Moreover, a quantum critical point has been observed in the intermediate solid solution $URh_{0.62}Ru_{0.38}Ge$ [4]. Contrarily to their uranium counterparts, neither NpRhGe [5] nor NpCoGe [6] exhibit superconductivity. Instead, these compounds order magnetically at significantly higher temperatures than URhGe and UCoGe, respectively. Actually, the neptunium compounds seem to follow the same trend as their uranium homologues, but with a shift, due to the shorter spatial extent of the *5f* orbitals in Np. Therefore, we anticipated magnetic collapse and possibly quantum criticality when moving to NpRuGe and NpFeGe (Fig.1).

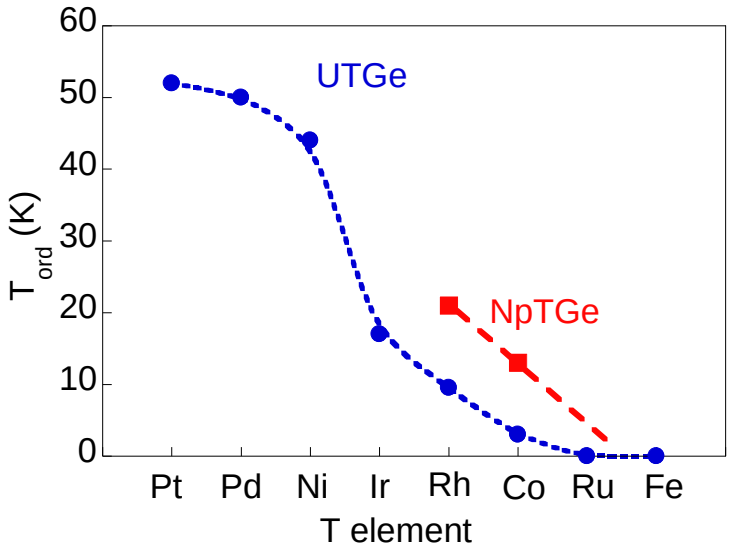

Fig. 1. Magnetic ordering temperature of UTGe (circles) [7] and NpTGe (squares) [5,6] compounds as a function of the T element.

We have synthesized polycrystalline samples of the new compound NpRuGe and found that it crystallizes into the same orthorhombic structure (Pnma) than the uranium and neptunium analogues mentioned above. We report here preliminary investigations on the magnetic and electronic properties of NpRuGe.

The magnetic susceptibility of NpRuGe shows the onset of antiferromagnetic order below $T_N \approx 56$ K (Figure 2) and a modified Curie-Weiss behaviour above T_N. The paramagnetic Curie temperature ($\theta_p \approx 14$ K) is found to be positive and relatively small compared to T_N. This indicates the presence of ferromagnetic interactions, possibly within planes coupled antiferromagnetically, and suggests that the application of a limited (but larger than 7 T)

magnetic field might break the antiferromagnetic arrangement of neptunium moments. The effective moment ($\mu_{eff} \approx 1.8\ \mu_B$) is reduced compared to the Np^{3+} free ion ($\mu_{eff} \approx 2.75\ \mu_B$ in intermediate coupling).
The specific heat of NpRuGe confirms the antiferromagnetic transition at $T_N \approx 56$ K (Fig.2) and reveals a Sommerfeld coefficient estimated to $\gamma \approx 60$mJ/mol.K^2.

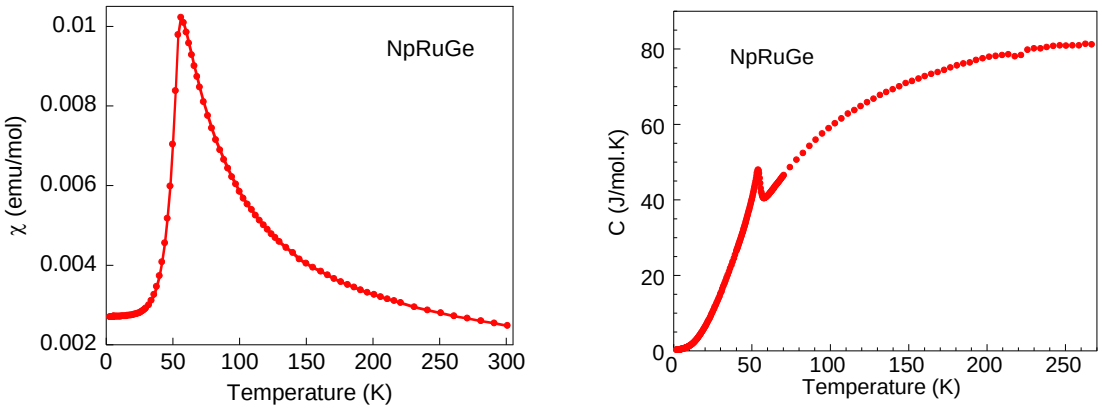

Fig. 2. Magnetic susceptibility of NpRuGe measured with B=7T (left) and specific heat in zero-field (right).

The ordering temperature of NpRuGe appears to be the largest in the whole AnTGe (An=actinide) series known so far. It obviously does not fit to the tendency extrapolated from Fig.1 where magnetic order was expected to vanish. This surprising behaviour of NpRuGe will be discussed and compared with its uranium and neptunium counterparts.
Complementary measurements are under way on NpRuGe (magnetic susceptibility up to 14 T, ^{237}Np Mössbauer spectroscopy, ab initio calculations…). Finally, it is planned to synthesize NpFeGe which is expected, from the trends observed in Fig.1, to be the least "magnetic" of the neptunium series. Results will either confirm this tendency or the deviation initiated by NpRuGe. It should be mentioned that in the uranium analogues, the weak paramagnet UFeGe [8] is not isostructural to the other UTGe compounds and exhibits instead a monoclinic distortion. The orthorhombic structure can be stabilized via hydrogenation [9] or zirconium substitution [10] but magnetic order has not been observed in any UFeGe modification.

Acknowledgements

We are grateful to D. Bouëxière, P. Amador and F. Kinnart for their technical support. The high purity Np metals required for the fabrication of the compound were made available through a loan agreement between Lawrence Livermore National Laboratory and ITU, in the frame of a collaboration involving LLNL, Los Alamos National Laboratory and the US Department of Energy.

References

[1] V. Sechovsky and L. Havela, in Ferromagnetic Materials edited by E.P. Wohlfarth and K.H. Buschow (Amsterdam: Elsevier 1988) vol **11**, p 415, and references therein.
[2] D. Aoki et al., Nature **413**, 613 (2001).
[3] N.T. Huy et al., Phys. Rev. Lett. **99**, 067006 (2007).
[4] N. T. Huy et al., Phys. Rev. B **75**, 212405 (2007)
[5] E. Colineau et al., J. Phys.: Condens. Matter **20**, 255234 (2008).
[6] E. Colineau et al., Journées des Actinides **42**, 23 (2012)
[7] R. Troć and V.H. Tran, J. Magn. Magn. Mater. **73**, 389 (1988)
[8] L. Havela et al., J. Magn. Magn. Mater. **177**, 47 (1998)
[9] A.M. Adamska et al., J. Alloys Comp. **509**, 5453 (2011)
[10] M. Henriques et al., Journées des Actinides **42**, 80 (2012)

$ThPt_2$ – a new representative of close packed tetragonal structures

Roman Gumeniuk, Walter Schnelle, Ulrich Burkhardt, Horst Borrmann, Michael Nicklas, Andreas Leithe-Jasper, Yuri Grin

Max Planck Institute for Chemical Physics of Solids, Nöthnitzer Str. 40, 01187 Dresden, Germany
gumeniuk@cpfs.mpg.de

$ThPt_2$ crystallizes with unique type of structure (space group *I*4/*mmm*, a = 4.1569(2) Å, c = 14.3678(6) Å). The crystal structure of $ThPt_2$ belongs to the variety of tetragonal structures with SG *I*4/*mmm*, unit cell parameters a = 4-5 Å; c = 14-18 Å and Pearson symbol *tI*12 (i.e. Ti_2Bi [1], La_2Sb [2] etc.).
Measurements of magnetic susceptibility, electrical resistivity and specific heat show $ThPt_2$ to be diamagnetic with metallic type of conductivity in good agreement with the calculated electronic structure ($N(E_F)$ = 0.92 states eV^{-1} $f.u^{-1}$).
An analysis of the chemical bonding by the electron density/electron localizability approach reveals formation of two-dimensional platinum anions being separated by the Th cations.

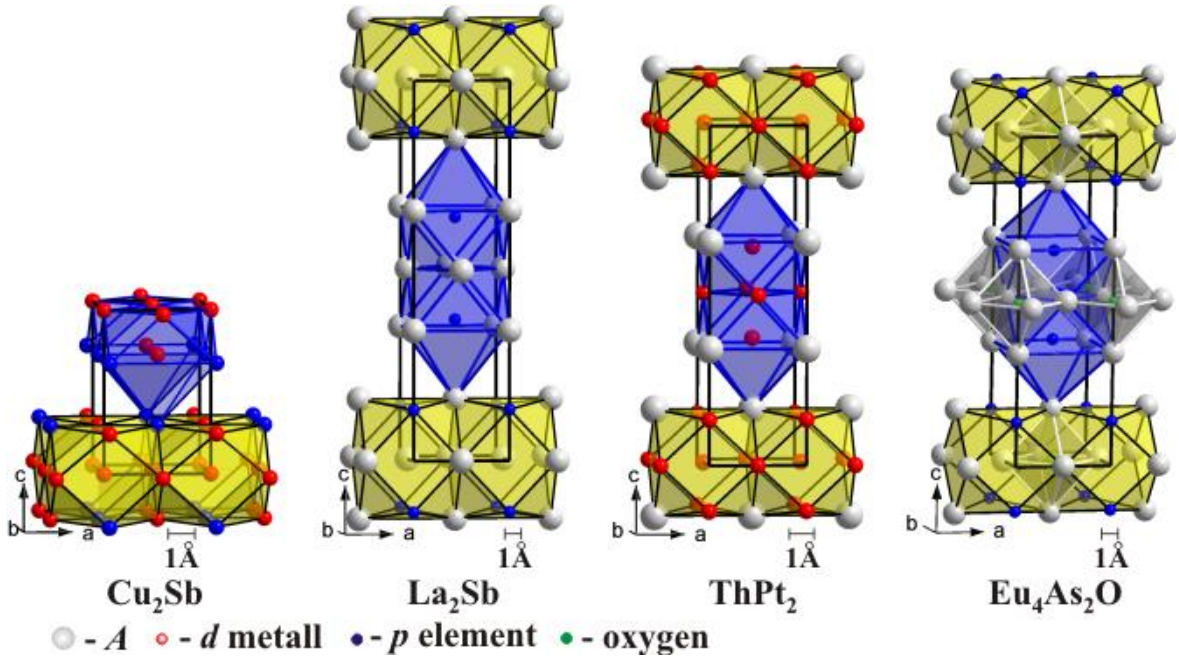

Fig. 3. Arrangement of the tetragonal antiprisms (CN = 9) and cubooctahedra (CN = 12) in the closely related Cu_2Sb, La_2Sb, $ThPt_2$ and Eu_4As_2O structure types.

References

[1] Auer-Welsbach, H. *et al. Mh. Chem.* **89**, 154 (1958).
[2] Stassen, W.N. *et al. Acta Cryst.* **26**, 1534 (1970).

Magnetic properties of the new Pu-based ferromagnet $Pu_2Pt_3Si_5$

J.-C. Griveau[1], E. Colineau[1], D. Bouëxière[1], K. Gofryk[1,2], T. Klimczuk[1,3], and J. Rebizant[1]

[1] European Commission, Joint Research Centre, Institute for Transuranium Elements; Postfach 2340, 76125 Karlsruhe, Germany, e-mail: jean-christophe.griveau@ec.europa.eu
[2] Los Alamos National Laboratory, Los Alamos, New Mexico 87545, USA
[3] Faculty of Applied Physics and Mathematics, Gdansk University of Technology, Narutowicza 11/12, 80-952 Gdansk, Poland

Considering plutonium based systems; it is surprising that not so many of them show magnetic ordering. Despite the fact that it is much more difficult to examine basic properties of plutonium compounds than for other actinides such as Th, U and even Np-based ones, the majority of Pu-based compounds, and not only intermetallics, have a tendency to present non magnetic ground states [1].

Here we report on structural, magnetic and thermodynamic properties of a new plutonium-based compound, namely $Pu_2Pt_3Si_5$. Single and polycrystals of produced by a Sn-flux technique have been analyzed by single crystal (CAD-4 diffractometer) and powder (Bruker D8) diffraction techniques. The results indicate that the new phase, $Pu_2Pt_3Si_5$, crystallizes with the orthorhombic Iabm structure (72) with atomic parameters: a=9.9226(2) Å, b=11.4436(2) Å and c=6.0148(1) Å.

Fig. 1 presents the magnetization curves of a polycristal $Pu_2Pt_3Si_5$ measured in magnetic fields of 10 and 70 kOe. The temperature behavior of the magnetization indicates that $Pu_2Pt_3Si_5$ orders ferromagnetically below T_C ~ 60 K. Above 100 K the inverse molar magnetic susceptibility, H/M ~ 1/χ determined at H= 70 kOe, can be well fit by the modified Curie–Weiss law $1/\chi = 1/(\chi_0 + C/(T-\theta_p))$ (see the inset in Fig. 1), yielding an effective magnetic moment μ_{eff} = 0.78 μ_B, a paramagnetic Curie temperature θ_p= 53.5 K, and χ_o=0.00322 emu.mol^{-1}. The positive value of the paramagnetic Curie temperature is consistent with ferromagnetic ordering in this material. The value of μ_{eff} = 0.78 μ_B is close to the Hund's rule value for Pu^{3+} (0.84 μ_B) and suggests a rather localized character of *5f*-electrons in this compound. The difference in the magnetization obtained in zero-field-cooled (ZFC) and field-cooled (FC) modes can be explained by the progressive alignments of domains when magnetic field is applied to the sample. From an Arrot's plot analysis we found that T_C is close to 58 K.

Heat capacity measurements have been performed on a single crystal of $Pu_2Pt_3Si_5$. A pronounced anomaly at T_C = 58 K is observed in agreement with the magnetic measurements. At 300 K the heat capacity has a slightly reduced value (~ 210 J.mol^{-1}K^{-1}) vs. the Dulong-Petit limit, i.e., C_p = 3nR = 244 J/mol K, where n = 10 is the number of atoms per formula unit and R is the gas constant, indicating that the Debye temperature is below 300 K. The magnetic field dependence confirms, as for magnetization measurements, a ferromagnetic nature of the anomaly: the peak visible on C_p/T is rising only slightly up when magnetic field is increased while the global area below the peak related to magnetic entropy is smeared out. The low temperature determination of the Sommerfeld contribution ($C_p/T \sim \gamma_e + \beta T^2$) leads to γ_e~2 mJ.mol^{-1}K^{-2} / Pu, and β = 0.85 mJ.mol^{-1}.K^{-4}. The value of β allows to estimate the Debye temperature θ_D ~ 286 K. The so-obtained value of θ_D is close to the one reported for the Rare Earths counterpart, with the same structure, $Lu_2Ir_3Si_5$ (θ_D ~ 320 K) [2].

The low temperature part of the electronic specific heat, γ_e~2 mJ.mol^{-1}K^{-2}/Pu, is very small when comparing to the other actinide based intermetallics, especially to similar $Pu_2Ni_3Si_5$ (85 mJ.mol^{-1}K^{-2}/Pu) and $Pu_2Co_3Si_5$ (~100 mJ.mol^{-1}K^{-2}/Pu) dense Kondo systems

[3]. This could indicate strong localization of *5f*-electrons in $Pu_2Pt_3Si_5$.

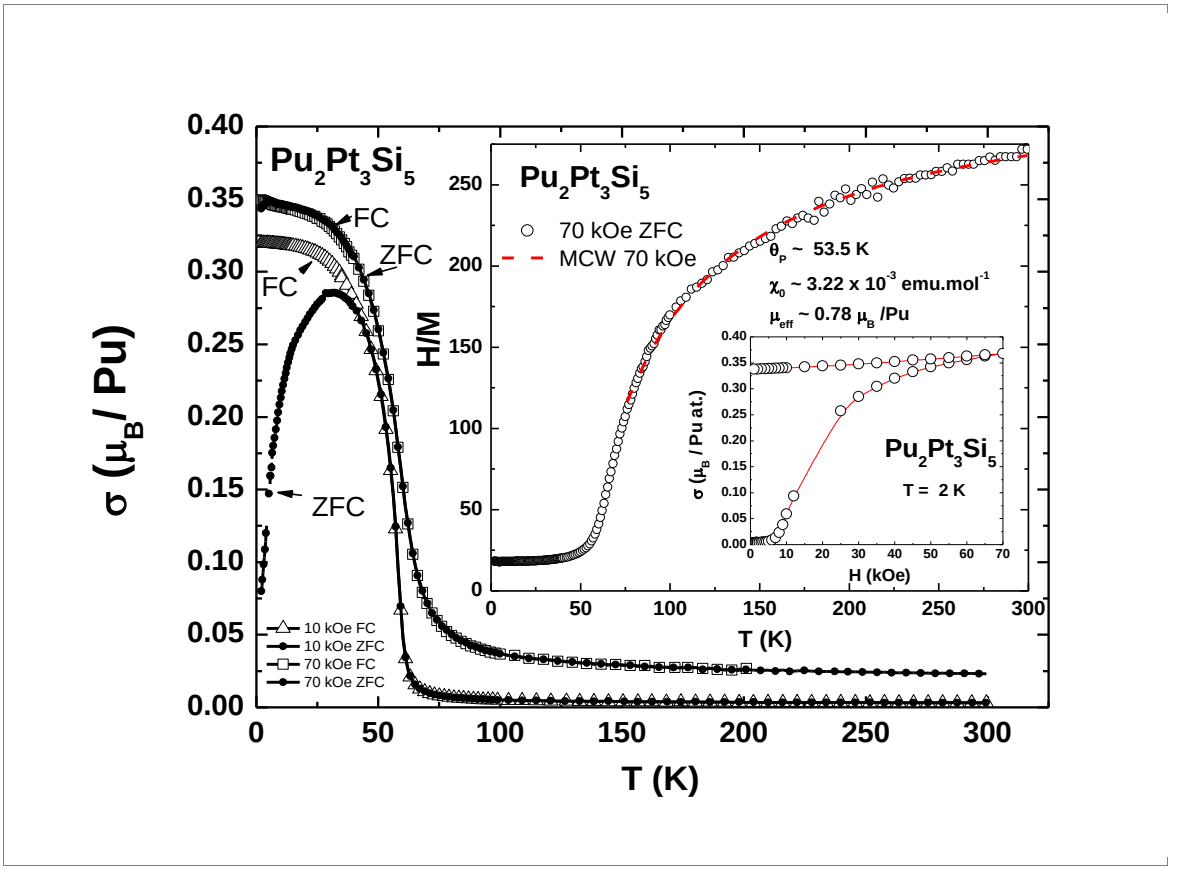

Fig. 1. Magnetization curves in ZFC and FC modes for 10 and 70 kOe obtained on a sample of 38 mg. A difference at low field for FC and ZFC indicates the presence of oriented domains in the materials. At sufficiently high field, this difference is no more observed as all domains are aligned with the applied field. The saturated moment at 70 kOe is estimated to σ_{sat}= 0.35 μ_B/Pu. Top inset shows the inverse molar susceptibility, 1/χ ~ H/M. Bottom inset shows first magnetization at 2 K and estimation of the saturated moment. It appears that the magnetization is not fully saturated even at the maximum field applied of 70 kOe.

Acknowledgements

The high purity Pu metal required for the fabrication of the compound were made available through a loan agreement between Lawrence Livermore National Laboratory and ITU, in the frame of a collaboration involving LLNL, Los Alamos National Laboratory and the US Department of Energy.

References

[1] L. Havela, P. Javorský, F. Wastin, E. Colineau, T. Gouder, A.B. Shick, V. Drchal, J. of Alloys and Compds, **444-445**, 88 (2007).
[2] Y. K. Kuo and K. M. Sivakumar, T. H. Su and C. S. Lue, Phys. Rev B **74**, 045115 (2006)
[3] E.D. Bauer, P.H. Tobash, J.N Mitchell, J.A Kennison, F. Ronning, B.L. Scott, J.D. Thompson, J. Phys.: Condens. Matter **23**, 094223 (2011)

Peculiar magnetism of U_2Fe_3Ge probed in single crystal studies

M.S. Henriques[1], D.I. Gorbunov[2,3], J.C. Waerenborgh[1], L. Havela[3], A.B. Shick[2], M. Diviš[3], A.V. Andreev[2], A.P. Gonçalves[1]

[1]*IST/ITN, Technical University of Lisbon, CFMC-UL, 2686-953-Sacavém, Portugal, e-mail: mish@ctn.ist.utl.pt*
[2]*Institute of Physics, Academy of Sciences of The Czech Republic, Na Slovance 2, 182 21 Prague, The Czech Republic*
[3]*Dept. Condensed Matter Physics, Faculty of Mathematics and Physics, Charles University 121 16 Prague, The Czech Republic*

A new U-based compound, U_2Fe_3Ge, was reported as crystallizing in the hexagonal Mg_2Cu_3Si-type structure, an ordered variant of the binary $MgZn_2$-type C14 Laves phase (space group $P6_3/mmc$) [1,2]. U_2Fe_3Ge is a fully ordered ternary compound: the U, Fe and Ge atoms occupy the three crystallographically non-equivalent sites 4*f*, 6*h* and 2*a*, respectively. (Fig. 1*a*). The structure can be described as having two kinds of layers along the *c*-axis. The first layer is non-planar and composed of U hexagons centered by Ge atoms (layer A, Fig. 1*b*). The second layer is formed only by Fe atoms arranged in a kagome net (layer B, Fig. 1*c*).The shortest U-U distances, $d_{U\text{-}U}$ = 2.8 Å, are along the *c*-axis, and are much shorter than the double atomic radius of uranium ($2r_U$ = 3.12 Å). Similar short distances, $d_{U\text{-}U}$ = 3.03 Å, were found in the isostructural compound UNi_2 [3].

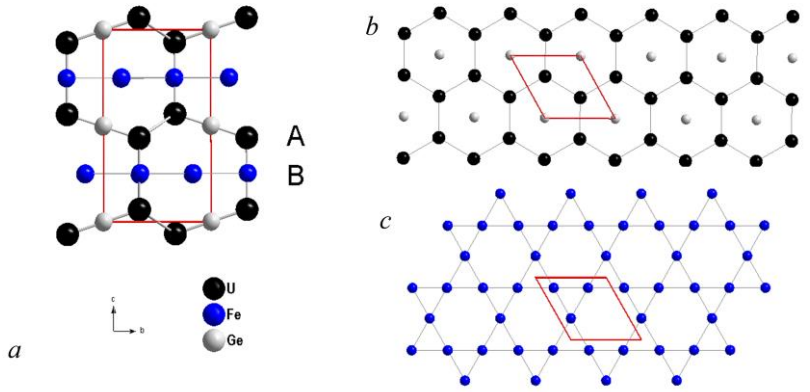

Fig. 1. Projection of the unit cell of the U_2Fe_3Ge compound onto the *bc*-plane (*a*) and the projections onto the *ab*-plane of the layer A (*b*)

Although in U_2Fe_3Ge $d_{U\text{-}U}$ is well below the Hill limit (3.4 – 3.6 Å for U), the compound is an itinerant ferromagnet below the Curie temperature T_C = 55 K, as already found on polycrystalline samples [1]. ^{57}Fe Mössbauer study showed that the Fe sublattice does not carry any significant ordered magnetic moment, which indicates that the magnetism in U_2Fe_3Ge originates from the U sublattice. For this reason U_2Fe_3Ge can be regarded as a new exception to the Hill rule.

Magnetization isotherms measured along the *a*- ([100]), *b*- ([120]) and *c*- ([001]) axes of the hexagonal U_2Fe_3Ge single crystal at T = 2 K are presented in Fig. 2. The compound exhibits a spontaneous magnetic moment along the *a*- and *b*-axes, whereas there is no spontaneous component along the *c*-axis. This indicates that the magnetic moments of U_2Fe_3Ge lie in the basal plane of the hexagonal lattice. The *c*-axis is the hard magnetization direction. The U magnetic moments are perpendicular to the shortest U-U spacing, as normally found in magnetically-ordered uranium intermetallics. There is no anisotropy in the basal plane of the compound. The spontaneous magnetic moment is equal to M_s = 1 μ_B/f.u., which corresponds to an average moment 0.5 μ_B/U atom. A strong growth in magnetization is observed along both axes in the basal plane after the domain-wall motion is completed. Magnetization along the hard axis grows linearly up to ≈ 8 T where a change of its slope appears reflecting the

anisotropy field H_a of the compound. Such low value of H_a determined directly from magnetization curves in static magnetic fields is the most striking feature displayed by the U_2Fe_3Ge compound. Even the isostructural compound UNi_2, where the low magnetic moment (0.08 μ_B/f.u.) is perpendicular to *c*-axis and is carried by U atoms, exhibits a strong magnetic anisotropy, with H_a higher than 40 T [3,4]. The type of the anisotropy with U moments in the basal plane can be associated in both cases with the shortest U-U spacing along *c*-axis, in accordance with the two-ion anisotropy model [5]. The calculation of the temperature dependence of the anisotropy constants for U_2Fe_3Ge supports this mechanism of anisotropy.
Electronic structure calculations (LSDA with FP-LAP and FPLO codes) correctly reproduce the type of anisotropy. Nevertheless, they do not explain the lack of the Fe contribution to the magnetism of U_2Fe_3Ge, giving a non-negligible ordered magnetic moment of Fe. The Fermi level is situated at the pseudo-gap of the projected spin minority DOS (Fig. 3).

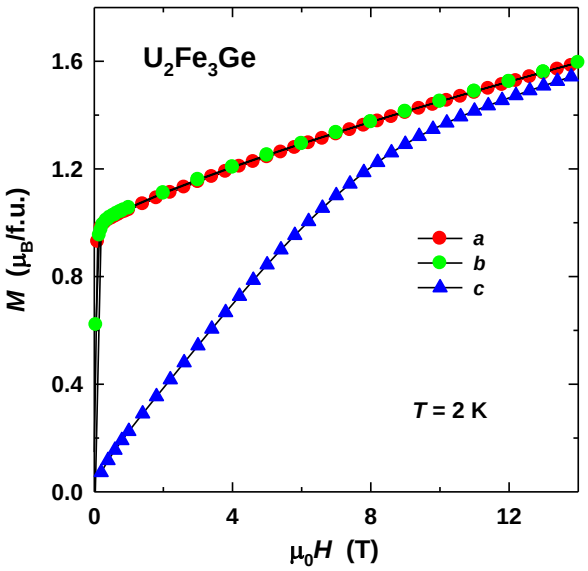

Fig. 2. Magnetization isotherms measured along the principal axes of the U_2Fe_3Ge single crystal at T = 2 K.

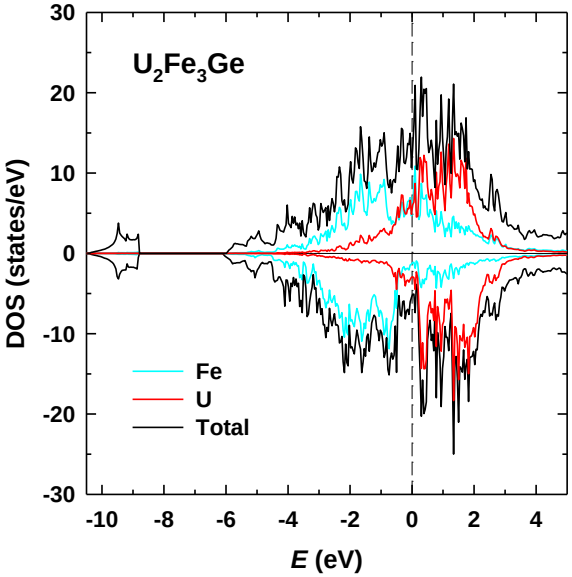

Fig. 3. Spin-polarized calculated DOS of U_2Fe_3Ge. Positive numbers mean spin-up DOS and negative numbers mean spin-down DOS. The Fe- and U-projected spin-up and spin-down DOS are shown by the cyan and red lines, respectively. The Fermi level is at zero energy.

References

[1] M.S. Henriques et al., *Solid State Comm*. **148**, 159 (2008).
[2] S.K. Dhar, et al., *Solid State Comm*. **147**, 217 (2008).
[3] P.H. Frings et al., *J. Magn. Magn. Mater* **54-57**, 541 (1986).
[4] J. J. M. Franse et al., *J. Appl. Phys*. **69**, 5903 (1991).
[5] [13] B.R. Cooper et al., in: Handbook on the Physics and Chemistry of the Actinides, A.J. Freeman and G.H. Lander, eds., vol.2, pp. 435-500, North-Holland, Amsterdam, 1985

Amorphous 5*f* ferromagnetic hydrides UH_3Mo_x

I. Tkach[1], N.-T.H. Kim-Ngan[2], S. Mašková[1], L. Havela[1], A.V. Andreev[3], Z. Matej[1]

[1] *Faculty of Mathematics and Physics, Charles University, Ke Karlovu 5, 12116, Prague, Czech Republic, e-mail: ilimp@yandex.ru*
[2] *Institute of Physics, Pedagogical University, Podchorazych 2, 30-084 Krakow, Poland*
[3] *Institute of Physics, ASCR, Na Slovance 2, 18221, Prague, Czech Republic*

Samples of uranium metal with cubic structure (γ-phase) were successfully stabilized to room temperature by ultrafast cooling technique (splat cooling) with addition of Mo [1]. While α-U sample quite easily forms β-UH_3 hydride, γ-U samples did not absorb hydrogen at ambient pressure. With increase of hydrogen pressure higher than 2.5 bar, γ-U samples start to form hydrides with hydrogen concentration 3 H/U atom. On the contrary to known crystalline β-UH_3, which is highly pyrophoric fine powder, our hydrides are in shape of 1-5 mm long brittle dark lamellas, which are stable at air and have an amorphous structure (Fig. 1) with nanoscale grain size.

The amorphous hydride $UH_3Mo_{0.18}$ exhibits ferromagnetic order with Curie temperature around 195 K (Fig. 2) and magnetisation 1.21 μ_B/U in magnetic field 14 T (175 K and 0.93 μ_B/U respectively for crystalline β-UH_3 [2]). Such fact is quite extraordinary, because introduction of disorder usually tends to suppress magnetism. A broad hysteresis appears on magnetization curves at low temperature (Fig. 3), the coercive force boosts reaching enormous 3.5 T at 1.7 K. Magnetisation reversal is characterised by a sharp jump at temperatures below 5 K. Such a behavior can be ascribed to random distribution of local high magnetic anisotropy (HARD materials).

Specific heat reveals that the Curie temperature of $UH_3Mo_{0.18}$ shifts indeed to higher temperatures (near 200 K) and transition becomes slightly broader than in β-UH_3. That can indicates some T_C distribution between different grains due to disorder in amorphous sample. Low temperature part can be well approximated by Debye model from which possible to estimate the Sommerfeld coefficient of electronic specific heat. A linear fit of C_P/T vs. T^2 in the temperature range below 50 K^2 yields the value γ_e = 27.6 mJ/mol K^2. Such value is approximately 3 times higher than for α-U and 2 times higher than for γ-U (splat sample $U_{0.85}Mo_{0.15}$). Increase of γ_e indicates increase of $N(E_F)$ and narrow 5*f* band with more localized electrons.

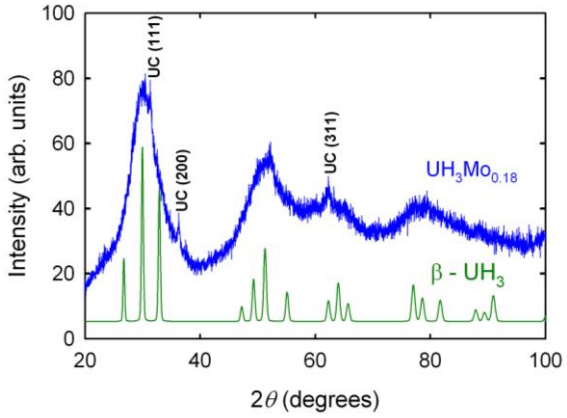

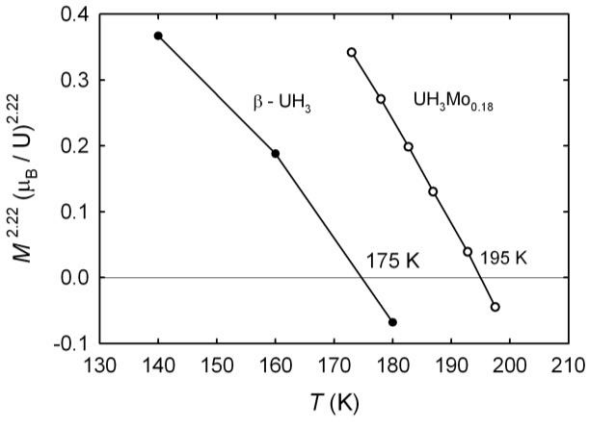

Temperature dependence of electrical resistivity of $UH_3Mo_{0.18}$ exhibits a negative slope ($d\rho/dT < 0$) (Fig. 4) similar to γ-phase U-Mo alloys [1]. Its reason can be seen in the weak localization, which appears under conditions of strong disorder, and which is partly suppressed by electron-phonon scattering. The absolute values of resistivity for $UH_3Mo_{0.18}$ are unusually high, exceeding 1000 μΩcm. It is approximately 10 times higher values than for initial splat sample $UMo_{0.18}$ and 2 times higher than for uranium deuteride [3]. A detailed inspection (see inset of Fig.4) reveals a cusp related to T_C = 200 K.
We can conclude that we described a novel type of material: 5*f* amorphous ferromagnet with high T_C. More detailed structure refinements, variations with Mo concentration and H pressure are under way.

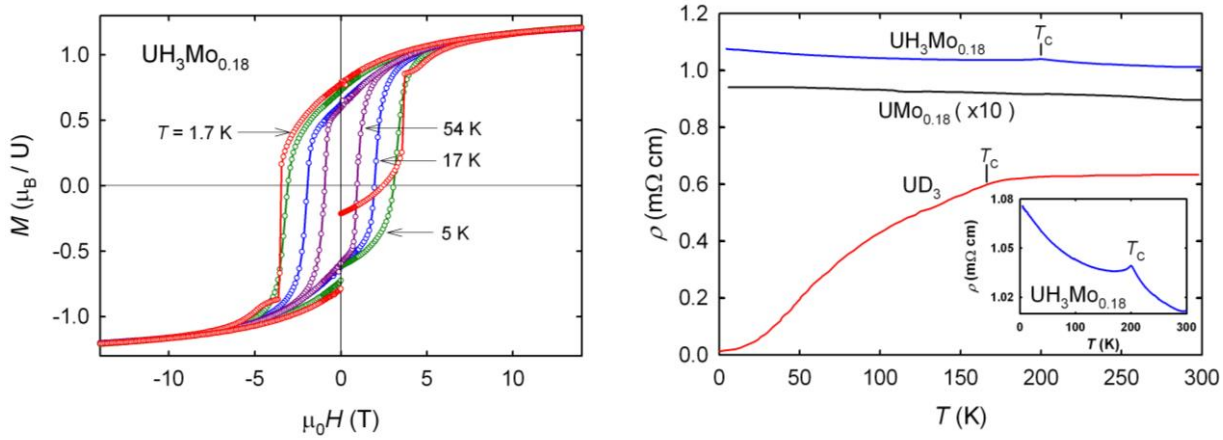

References

[1] I. Tkach, Nhu-T.H. Kim-Ngan, S. Mašková, M. Dzevenko, L. Havela, *J.Alloys Comp.* **101-109**, 534 (2012).
[2] A.V. Andreev, S.M. Zadvorkin, M.I. Bartashevich, T. Goto, J. Kamarad, Z. Arnold, H. Drulis, *J.Alloys Comp.* **32-36**, 267 (1998).
[3] J.W. Ward, L.E. Cox, J.L. Smith, G.R. Stewart, J.H. Wood, *J.Phys.* **C4-C15**, 40 (1979).

5f correlations and core level photoelectron spectra of actinides

Gertrud Zwicknagl

Institut fuer Mathematische Physik, Technische Universitaet Braunschweig, 38106 Braunschweig, Germany, e-mail: g.zwicknagl@tu-bs.de

Microscopic model calculations for core-level spectra of U compounds are presented. The key idea is that the different screening behavior of localized and itinerant electrons may help to decide whether and to which extent the actinide 5f states preserve their atomic character or whether they from extended coherent band states. The theoretical work has been motivated by recent experiments [1] which showed that the core level spectra of U compounds exhibit rich structures with a wide yet systematic variation from compound to compound. The calculations which adopt the Gunnarsson-Schoenhammer ansatz analyze the consequences of strong intra-atomic correlations within the 5f-shell. Previous model [2, 3] studies suggested that orbital-selective localization resulting from strongly anisotropic renormalization of the hybridization between 5f- and conduction states should be reflected in the line shapes. We discuss how a realistic description of the conduction electrons, the choice of the coupling scheme (LS-, jj-, intermediate coupling) and shake-up processes affect this result.

References

[1] Shin-ichi Fujimori et al., J. Phys. Soc. Jpn. **81**, , 014703, (2011)
[2] Gertrud Zwicknagl, *Mat. Res. Soc. Symp. Proc.* DOI:10.1557/opl.2012.1126
[3] Gertrud Zwicknagl,. *physica status solidi (b)* DOI: 10.1002/pssb.201200732 (2013)

Electronic and magnetic structures of U_2N_2(P;As;S;Se) having the highest Néel temperatures among uranium compounds

M. Samsel-Czekała,[1] M.J. Winiarski[1]

[1] *W. Trzebiatowski Institute of Low Temperature and Structure Research, P.O. Box 1410, 50-950 Wrocław 2, Poland, e-mail: M.Samsel@int.pan.wroc.pl*

Antiferromagnetic ternary systems U_2N_2M (*M*= P; As; S; Se) crystallize in the hexagonal Ce_2O_2S-type structure [1]. Interestingly, all of them exhibit high Néel temperatures T_N>230 K. The highest T_N = 406 K among all known actinide antiferromagnets has just been found for U_2N_2As [2]. Neutron diffraction studies [2] revealed that in these ternaries the magnetic moments on uranium atoms are aligned along the *c* axis, having also high magnitudes ranging from 1.4 to 2.25 μ_B per U at. (at 4 K). Whereas the chalcogenides U_2N_2(S;Se) have the same size of their magnetic unit cells (u.c.'s) (AFI-type) as the chemical ones, the pnictides U_2N_2(P;As) have their magnetic u.c.'s doubled along the *c* axis (AFII-type) [2].
To explain the origin of so strong magnetism in these systems, we have calculated their electronic structures and magnitudes of magnetic moments, employing fully relativistic and full potential local orbital code (FPLO-9) [3]. The local spin density approximation (LSDA) of the exchange-correlation potential was utilized with or without an inclusion of different versions of an orbital polarization correction (OPC): OPB or OPX [4]. In calculations of the total and band energies, densities of states (DOS's), Fermi surfaces (FS's) and magnitudes of uranium magnetic moments in the AFI- or AFII-types of magnetic u.c.'s, experimental values of lattice parameters and atomic positions (at 4 K) were taken from [2].

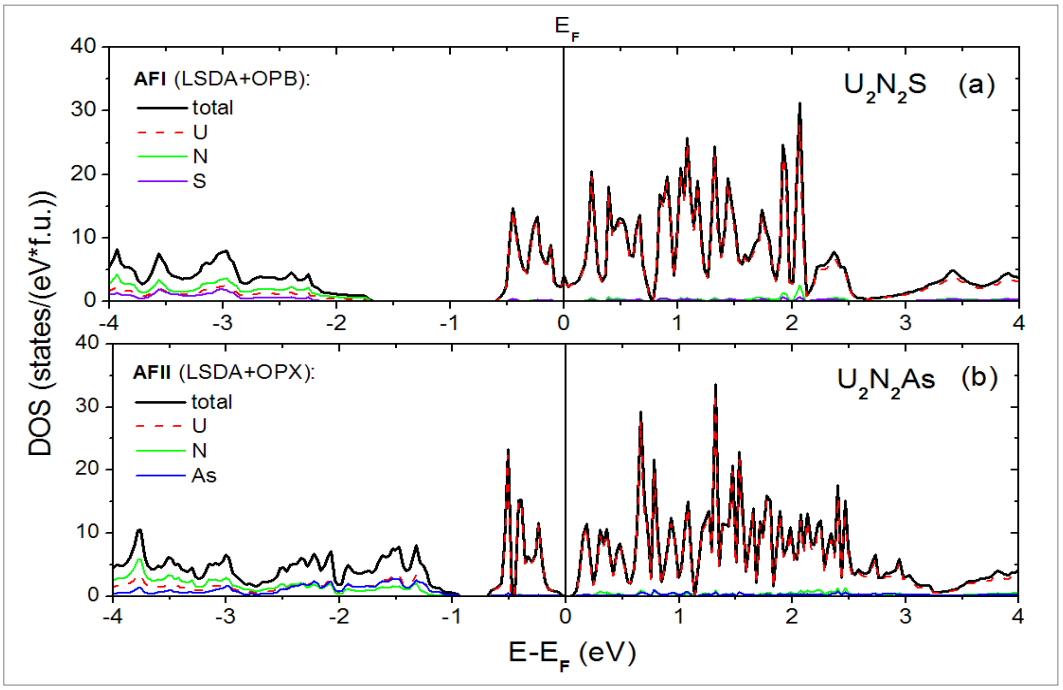

Fig. 1. The calculated total and partial (per given atom) DOS's of: (a) U_2N_2S in AFI-type magnetic u.c. (LSDA+OPB) and (b) U_2N_2As in AFII-type magnetic u.c. (LSDA+OPX).

As exemplary results, in Fig. 1 we present the total and partial DOS's of U_2N_2S (AFI) and U_2N_2As (AFII), obtained by employing the LSDA+OPB and LSDA+OPX approaches, respectively. These approaches yielded the best agreement of the calculated uranium magnetic moments with the experimental ones [2]. As seen in this figure, the computed DOS's in U_2N_2S (and also in U_2N_2Se – not shown) exhibit their metallic character, while for U_2N_2As its DOS revealed a narrow band gap at the Fermi level (E_F), being typical of semiconductors. Interestingly, the latter system in the nonmagnetic state is metallic and it becomes semiconducting only after including both spin and orbital polarization effects by the LSDA+OPX approach. Very near to a semiconducting behaviour is also its counterpart U_2N_2P (T_N = 366 K). This semiconducting behaviour can be a reason for stabilizing even above the room temperature, the magnetic structure of the AFII-type in both these pnictides.
At the same time, our calculation results indicate that the metallic bonds in U_2N_2(S;Se) are created only by electrons (mainly 5f and 6d) coming from uranium atoms, similarly to those in related compounds containing also uranium and nitrogen atoms, like UN [5], U_2N_2(Sb;Te;Bi) [6], and UN(Te;Se) [7] systems. Furthermore, their FS's are reduced (as in semimetals) to single and narrow electronlike corrugated cylinders, located along the *c* axis (see Fig. 2). It shows that the metallic state is formed primarily within the uranium planes, being perpendicular to this axis.
In conclusion, the considered ternaries, particularly U_2N_2As, turned out to possess unique electronic structures related to their outstanding magnetic properties.

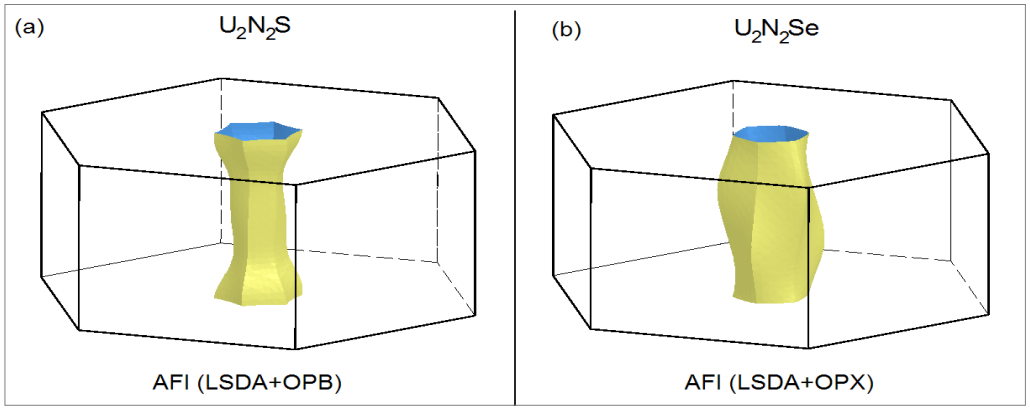

Fig. 2. The calculated FS's of: (a) U_2N_2S in AFI-type magnetic u.c. (LSDA+OPB) and (b) U_2N_2Se in AFI -type magnetic u.c. (LSDA+OPX), drawn in the hexagonal Brillouin zone boundaries.

References:

[1] R. Troć, Z. Żołnierek, *Proc. Int. Conf. on Magnetism* (Nauka, Moscow, 1975), **VI**, p. 59; Z. Żołnierek and R. Troć, *Proc. 5th Int. Conf. on Plutonium and Other Actinides*, eds. H. Blank and R. Lindner (North-Holland, Amsterdam, 1976), p. 589.
[2] J. Leciejewicz et al., *J. Phys. C: Solid State Phys.* **8**, 1697 (1975).
[3] FPLO-9.00-34-x86_64; http://www.FPLO.de.
[4] OPC implementation in FPLO-9, according to : O. Eriksson et al., *Phys. Rev. B* **41**, 7311 (1990) [OPB]; H. Eschrig et al., *EPL-Europhys. Lett.* **72**, 611 (2005) [OPX].
[5] M. Samsel-Czekała et al., *Phys. Rev. B* **76**, 144426 (2007).
[6] M. Samsel-Czekała, *Phys. Rev. B* **80**, 045121 (2009).
[7] M. Samsel-Czekała, *Phys. Rev. B* **81**, 195115 (2010).

Theoretical modeling of complex antiferromagnetic state in NpCoGe intermetallic compound.

S. Khmelevskyi,[1] A. B. Shick[2,3], E. Colineau[3]

[1] *Center for Computational Materials Science, IAP, Vienna University of Technology, Gusshausstrasse 25a, 1040, Vienna, Austria.*
[2] *Institute of Physics, Academy of Sciences of the Czech Republic, Na Slovance 2, 182 21 Prague, Czech Republic.*
[3] *European Commission, Joint Research Centre, Institute for Transuranium Elements, Postfach 2340, 76125 Karlsruhe, Germany.*

The magnetic studies of NpCoGe intermetallic compound have revealed an onset of antiferromagnetic order below 13 K. The measured Mossbauer spectra at low temperatures indicates the existing of four different values of the Np atomic moments with average at about 0.8 μ_B/Np [1,2]. In the present work we suggest that the estimated experimental values of the moments **m(r)** can be very well fit by elliptical magnetic spiral:

$$\mathbf{m}(\mathbf{r}) = \boldsymbol{p}\sin(2\pi\boldsymbol{q}\cdot\mathbf{r}+\varphi) + \mathbf{t}\cos(2\pi\boldsymbol{q}\cdot\mathbf{r}+\varphi)$$

where **r** is the radius vector of the atomic position**, q** is wave vector of the spiral , φ is the phase angle and semi-axis of the ellipse $\boldsymbol{p}$ and $\boldsymbol{t}$ are perpendicular to each other. In case of $|\boldsymbol{p}| = |\boldsymbol{t}|$ the expression describes an ordinary spin spiral.
First-principles calculations based on relativistic LAPW formalism [3] and bulk Korringa-Kohn-Rostokker Green Function method [4] has been performed to investigate the possible mechanism of the spin spiral formation. By calculating the magnetic exchange interactions using Lichtenstein Green function formalism [5] we have find a strong competition of ferro- and antiferromagnetic interactions within *bc*-planes of Np atoms on the underlying orthorhombic TiNiSi-type structure. It is shown that this competition leads to the formation of spiral magnetic states in b-crystal direction, whereas the stacking of the Np atoms within a "zigzag" of nearest neighbour atoms along *a*-axis is ferromagnetic. Thus the result of our ab-initio studies is well in agreement with hypothesis of non-collinear elliptical spin-ordering, which follows from the interpretation of Mossbauer experiments.
We have shown in addition that the Co atoms do not possess an intrinsic magnetic moment, whereas the moderate value of the Np moment is the result of strong compensation of large spin and orbital contribution, which has opposite directions.

References

[1] E. Colineau, R. Eloirdi, J.-C Griveau, P. Gaczynski and A. Shick, proceedings of the 42èmes Journées des Actinides, Bristol, UK, p.23 (2012)
[2] E. Colineau, R. Eloirdi, J.-C Griveau, P. Gaczynski and A. Shick, proceedings of ICM 2012, Busan, Korea, J. Korean Phys. Soc., in press (2013)
[3] E. Wimmer, H. Krakauer, M. Weinert, A. J. Freeman, Phys. Rev. B **24**, 864 (1981).
[4] A. V. Ruban, and H. L. Skriver, Comp. Mat. Science **15**, 119 (1999).
[5] A. I. Liechtenstein, M. I. Katsnelson, A. V. Antropov, and V. A. Gubanov, J. Magn. Magn. Mater. **200**, 148 (1987).

Towards prediction of symmetry of the intermetallic structures formed in the Al-TM-Ac alloys

Avraham I Bram[1,2], Arie Venkert[3], Louisa Meshi[1,2]

[1] *Department of Materials Engineering, Ben-Gurion University of the Negev, Beer-Sheva 84105, Israel, e-mail: avrambram@gmail.com*
[2] *Ilse Katz institute for nanotechnology, Ben Gurion University of the Negev, Beer Sheva 84105, Israel*
[3] *Nuclear Research Center-Negev, POB 9001, Beer-Sheva, Israel*

Kiv et al [1] suggested that symmetry of the stable structures of intermetallides present in the Al-based alloys with transition metal (TM) is related to the degree of distortion of the first-neighbour coordination polyhedra formed around the transition metal atoms. The aim of this work was to verify experimentally this theory for the Al-TM-Ac system where TM is transition metal and Ac-actinoid. This theory can be explained in terms of the coordination compounds and the chemical bonds theories [2]. Those theories suggest that the degenerated energy levels of d-orbital in transition metal atoms split under the influence of the field of surrounding atoms. The distance between the splitted levels is the factor which may control the stability of the structure [3]. The greater the distance between the splitted levels, the structure is more stable. The splitted levels affect the electronegativity of the neighbours of the transition metal atom and the effective charge of the transition metal. The structure symmetry is explained by Jahn-Teller effect [4]. The relationship between effective charge and electronegativity is an important characteristic which determines the stability and the symmetry of the structure. The symmetry of the stable structure is lower when this relationship is low. Therefore, the stability and the symmetry of the structure are a function only of the type of transition metal atom.

In the present research we focused on Al-TM-Th system, where TM=V, Fe and Ni. Alloys with different transition metal were prepared with the same 87at%Al-8at%TM-4at%Th composition from 99.99% pure metals in an arc furnace under argon atmosphere. Then, the samples were wrapped in Ta foil sealed in quartz tube under dried argon atmosphere and homogenized in the resistance furnace for 3 weeks at different temperatures according to the alloys composition. In order to achieve equilibrium state additional heat treatment was performed. Detailed phase characterization was performed by transmission and scanning electron microscopy (TEM and SEM) and X-ray powder diffraction. The composition of the phases was analyzed by Energy Dispersive X-ray Spectroscopy (EDS). Several new phases were revealed during the research: metastable $Al_{11}Th_3$ phase, stable $Al_{20}V_2Th$ and $Al_{12}Ni_6Th$. Some of them belong to known structure types frequently encountered in the Al-TM-Ac systems.

References

[1] A.E. Kiv, V.I. Ezersky, M.M. Talianker, Materials Science and Engineering A352, 2003, p.100-104
[2] S. Sugano, Y. Tanabe, H. Kamimura, Multiplets of Transition Metal Ions in Crystals, Academic Press, New York, London, 1970, p.331.
[3] D.A. Brown, W.J. Chambers, N.J. Fitzpatrick, Inorg. Chem. Acta. Rev. 6, 1972, p.1013.
[4] H.A. Jahn, E. Teller, Proc. R. Soc. A161, 1937, p.220.

First-principles modeling of uranium and plutonium mixed oxide

Boris Dorado,[1] Philippe Garcia[2]

[1] *CEA, DAM, DIF, F-91297 Arpajon, France, e-mail: boris.dorado@cea.fr*
[2] *CEA, DEN, DEC, Centre de Cadarache, 13108 Saint Paul Lez Durance, France*

Uranium-plutonium mixed oxide [MOX: $(U_{1-y}Pu_y)O_{2\pm x}$] is a nuclear fuel that consists of a mixture of uranium and plutonium dioxides (UO_2 and PuO_2, respectively) with a Pu content between 5% and 30%. The experimental and theoretical studies MOX fuels have been the subject of over the years have not been as comprehensive as in the case of uranium dioxide, which is the most widely used nuclear fuel worldwide, especially in relation to electronic structure.

Experimental work is made more difficult and costly with these fuels as a result of the precautions required for handling plutonium based materials. Most experimental studies deal with thermodynamic and structural characterizations of MOX along with electron microscopy and spectroscopic studies (x-ray absorption spectroscopy (XAS) or Raman spectroscopy). Recently it was shown that approaches that go beyond standard DFT are capable of providing values for the energies relating to atomic processes in uranium dioxide that are very close to the appropriate experimental data. On the strength of this, our underlying goal is to apply first principles methods to calculate as wide a range of properties as possible, thus reducing the range of experimental data required for fuel development purposes and hopefully contributing to a reduction in fuel development costs.

However, atomic-scale modeling of MOX is made more difficult by a number of complicating factors related to (1) the lack of data against which calculations may be assessed (e.g. electronic structure, magnetism, cohesive energy, elastic constants, bulk modulus, etc.) (2) the presence of strong electron correlations that require approximations beyond standard DFT (3) the presence of metastable states induced by these approximations, and (4) the random distribution of plutonium atoms in the UO_2 matrix that cannot be modeled by conventional supercell techniques. Because of these difficulties, first-principles studies of MOX are hard to come by.

The present study aims to show how these difficulties may be tackled and is a first step towards providing quantitative data (relating for instance to point defect behavior) which will ultimately help predict the specific evolution of MOX fuel microstructure under irradiation. We provide DFT based data relating to MOX fuel physical properties (electronic structure, mechanical properties, etc.) and show how they vary with respect to the amount of plutonium in the UO_2 matrix. These data are then compared to existing experimental information and should constitute an interesting benchmark against future experimental or theoretical studies.

First-principles study of radiation damage in uranium dioxide: inclusion of strong electronic correlations and van der Waals interactions

E. Vathonne,[1] M. Freyss[1], B. Amadon[2], M. Bertolus[1]

[1] *CEA, DEN, DEC, Centre de Cadarache, 13108 Saint-Paul-Lez-Durance Cedex, France, e-mail:emerson.vathonne@cea.fr*
[2] *CEA, DAM, DIF, DPTA, 91297 Arpajon Cedex, France*

Uranium dioxide is currently the most widely used fuel in the nuclear power plants. The fission of uranium atoms causes irradiation defects, as well as the production of a large quantity of volatile fission products (xenon, krypton…), which is a limiting factor for the efficiency of the fuel. Electronic structure calculations are an efficient tool allowing one to study the behaviour of point defects and fission products in uranium dioxide at the atomic scale. It is, however, still a challenge to study radiation damage in UO_2 using density functional theory-based methods.

Uranium dioxide is a Mott insulator and the uranium 5f electrons are localized and strongly correlated in this compound [1]. Within the standard approximations (LDA and GGA) of the density functional theory (DFT), the strong correlations of the 5f electrons are underestimated, which leads to a wrong description of the electronic structure of UO_2 (in particular, UO_2 is found to be metallic in standard DFT) [2]. To overcome this problem, the DFT+U [3] is used to increase the strong electronic correlations by adding a Hubbard-type coulombic term. However, a problem of metastable states appears with this method and some techniques ensuring the convergence toward the ground state of the system has to be used [4].

Secondly, the majority of the fission products are rare gases, such as xenon or krypton. Furthermore, helium is produced in large quantity by alpha disintegration. Standard DFT fails to describe the van der Waals (vdW) interactions formed by rare gases because the LDA and GGA approximations are local or semi-local, whereas the vdW interactions are non-local [5]. To overcome this problem, some functionals have been developed (such as the van der Waals Density functional: vdW-DF) which allows a better description of vdW interactions by a non-local correlation term [6] (Fig. 1.).

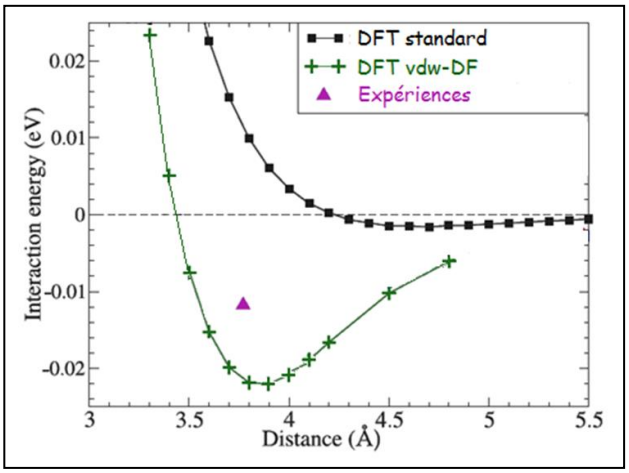

Fig. 1.: Interaction energy in function of the distance between two krypton atoms in DFT standard (black), DFT with van der Waals Density Functional (Green) and the experimental value (purple) [6]

We will first present more sophisticated methods allowing for a better description of strongly

correlated materials, in particular the combination of the DFT with the dynamical mean field theory (DFT+DMFT), which has recently been implemented in the code Abinit [7, 8]. This method allows one to describe the dynamical correlations by taking into account the possibility for localized electrons to change configuration among correlated orbitals. Moreover, the paramagnetic phase can be described with a small number of atoms. This method allows to better describe the electronic structure in UO_2 (Fig. 2.). We will present energetic, electronic and mechanical properties yielded by the DFT+DMFT in the Hubbard I approximation [8] and will compare them with the results obtained in standard DFT, DFT+U and experimental results. This comparison will allow us to evaluate the importance of taking into account the strong electronic correlations and the paramagnetic phase in the description of uranium dioxide.

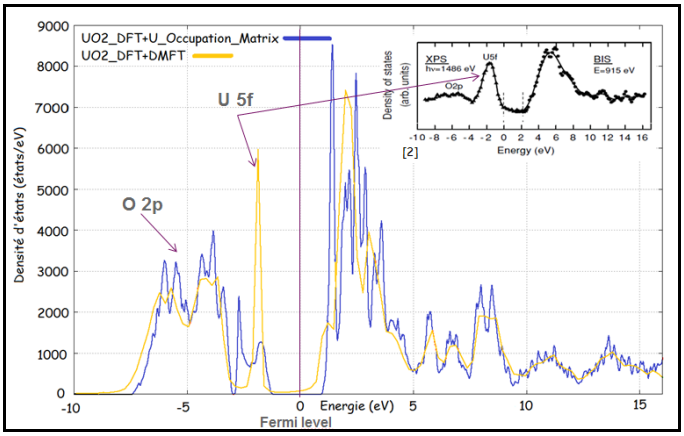

Fig. 2.: Density of states obtained in DFT+U (blue) and in DFT+DMFT (yellow) and experimental data (black) [1]

Second, results on the behaviour of rare gas atoms, such as helium, xenon and krypton, in UO_2 will be presented in order to evaluate the influence of the van der Waals interactions on their incorporation energies. This comparison will allow us to assess the accuracy of standard DFT for the calculation of incorporation energies of fission products in UO_2.

References

[1] Y. Baer, J. Schoenes, Solid State Commun. 33 (1980) 885.
[2] M. Freyss, T. Petit, J.-P. Crocombette, J. Nucl. Mater. 347 (2005) 44.
[3] V.I. Anisimov, J. Zaanen, O.K. Andersen, Phys. Rev. B 44 (1991) 943.
[4] B. Dorado, B. Amadon, M. Freyss, M. Bertolus, Phys. Rev. B 79 (2009) 235125.
[5] M. Bertolus, M. Major, V. Brenner, Phys. Chem. Chem. Phys. 14, 553 (2012) and references therein
[6] M. Dion, H. Rydberg, E.Schröder, D. C. Langreth, B. I. Lundqvist, Phys. Rev. Lett. 92 (2004) 24.
[7] B. Amadon, F. Lechermann, A. Georges, F. Jollet, T.O. Wehling, A.I. Lichtenstein, Phys. Rev. B 77 (2008) 205112.
[8] B. Amadon, J. Phys.: Condens. Matter 24 (2012) 075604.

Altering the hydriding behaviour of uranium metal by induced oxide penetration around carbonitride inclusions

N.J. Harker,[1] T. B Scott[1], C. P. Jones[1], J. R. Petherbridge & J. Glascott[2]

[1] *University of Bristol, Interface Analysis Centre, BS2 8BS, UK, e-mail: n.j.harker@bristol.ac.uk*
[2] *AWE, Aldermaston, Reading, UK*

Secondary Ion Mass Spectrometry (SIMS) and Focused Ion Beam (FIB) milling were used to examine the surfaces of uranium samples, both before and after limited hydride formation to identify surface features that could provide sites for preferential hydrogen attack. Two sets of cast uranium samples containing 600ppm carbon in the form of carbo-nitride inclusions were examined; one set was prepared by mechanically polishing to a fine grade and the other received a subsequent electropolishing step. SIMS analysis showed that the additional electropolishing resulted in oxide development along the inclusion metal interface that was not present after only mechanical polishing. These samples then underwent hydrogen exposure for a limited period under conditions expected to result in hydride formation. For uranium prepared by only mechanical polishing, the hydride growths were observed to occur in significant numbers and almost exclusively around exposed inclusions. Conversely, preparation involving electropolishing resulted in extremely limited numbers of hydride growth sites not obviously associated with inclusions. These differences in hydride formation behaviour are attributed to the presence of oxide formed along the inclusion-metal interface resulting from electropolishing, and highlight how the observed hydride-forming behaviours exhibited by uranium can be significantly altered by the method of surface preparation.

Characterization of uranium-molybdenum alloys and associated surface corrosion products

A M Adamska, T B Scott, R Springell, P J Heard, K R Hallam and C M Younes

Interface Analysis Centre, University of Bristol, Oldbury House, Bristol, BS2 8BS, United Kingdom
e-mail: am.adamska@bristol.ac.uk

Uranium (U) is of great importance as a nuclear fuel. Uranium metal was used in early reactor systems but it has been largely replaced by uranium dioxide fuel in more recent commercial reactors. However, the next generation of nuclear reactors are currently thought to require a more uraniferous material for fuel elements. Uranium alloys with e.g. Nb, Mo or Zr are the most promising candidate materials. Metallic uranium has three crystalline phases: α-; β-; and γ-phase. The α-phase is the room temperature (RT) form of uranium. It is orthorhombic with space group *Cmcm* and unit cell parameters a = 2.854 Å, b = 5.87 Å, and c = 4.955 Å [1-2]. This phase exhibits poor irradiation stability in the form of thermal and irradiational expansion under typical reactor operating conditions, making it unsuitable as a fuel [3-5]. The β-phase of uranium exists between 668 and 775°C. It has a complex structure with six crystallographically independent atoms in a tetragonal unit cell [6]. The high temperature (T > 775°C) uranium γ-phase (γ-U), having body-centred cubic (*bcc*) structure with space group *Im*3*m* and cell parameter a = 3.524 Å, is more resistant to irradiation effects than the α-phase. However, it is not thermodynamically stable under preparation and irradiation conditions. The γ-U phase may be stabilized at RT by the addition of selected transition metals, such as Mo, Nb or Zr.

In the current study, a series of U-Mo alloy thin films and their corrosion products, i.e. α-UH_3, UO_2 and UO_{2+x}, have been prepared by a sputter deposition technique on various substrates (glass or silicon for polycrystalline samples and sapphire for single crystals) and at different temperatures. All uranium thin films were capped with a 20-50 nm thick protective layer of Nb or Mo to prevent oxidation. The crystal structure of the films has been investigated by means of X-Ray Diffraction (XRD). Energy-Dispersive X-ray analysis was used to find the elemental composition of the materials. The thickness of the films was measured from cross-section analysis using Focused Ion Beam (FIB) and Scanning Electron Microscopy techniques. The thickness of the polycrystalline U-Mo films was also determined using Secondary Ion Mass Spectrometry (SIMS). The recorded SIMS spectra and depth profiles for $U_{0.78}Mo_{0.22}$ single crystal (Fig. 1) show well defined layers deposited by the PVD system.

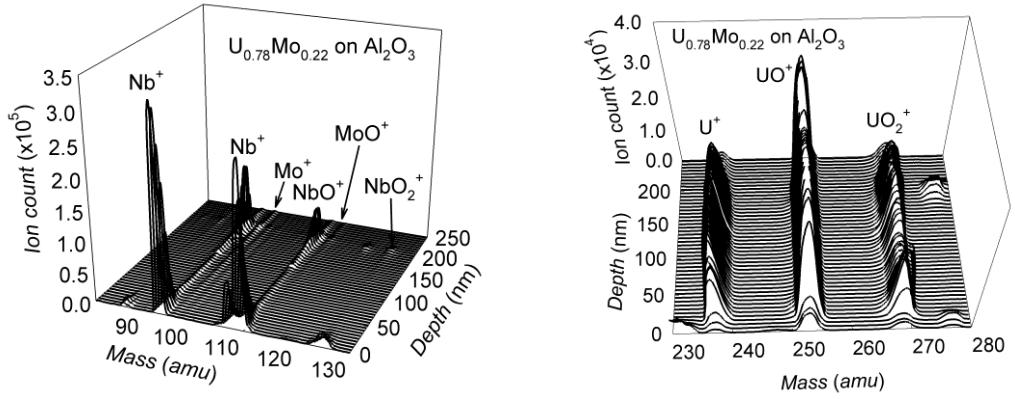

Fig. 1. Mass spectra from U-Mo thin film. (a) Ion signals from Nb cap/interface and Mo. (b) Ion signal from U and its oxide growing during the ion etching.

For oxidation studies the protective capping layer was removed using gallium FIB or Ar^+ sputtering. The subsequent oxidation behaviour was then studied using SIMS, Auger Electron Spectroscopy and X-ray Photoelectron Spectroscopy.

The arising results provide new insights into the phase stability in the U-Mo thin film systems (Fig. 2) in comparison to bulk alloying studies. Results suggest a subtle phase stability difference between polycrystalline and single crystal thin film systems.

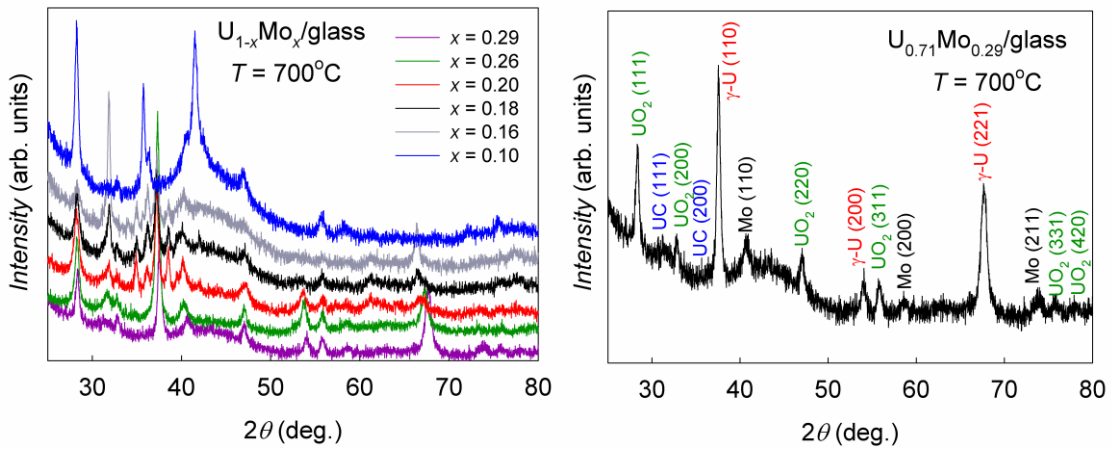

Fig. 2. (a) XRD patterns for $U_{1-x}Mo_x$ alloys capped with Mo. (b) XRD pattern of $U_{0.71}Mo_{0.29}$ sample showing the presence of γ-U phase (lattice parameter: a = 3.39(2) Å in comparison to a = 3.48 Å calculated from the equation a(Å) = 3.4808 – 0.00314x_{Mo}, where x_{Mo} is at.% of Mo [7-8]), UO_2, UC and Mo.

References

[1] C. S. Barrett et al., *Phys. Rev.* **129**, 625 (1963).
[2] G. H. Lander et al., *Acta Cryst.* **B26**, 129 (1970).
[3] A. N. Holden, *Physical Metallurgy of Uranium*, Addison-Wesley Publishing Co., Inc., USA, (1958).
[4] G. Ostberg et al., *J. Nucl. Mater.* **10 (4)**, 329 (1963).
[5] D. D. Keiser Jr et al., *J. Nucl. Mater.* **393**, 311 (2009).
[6] J. Donohue et al., *Acta. Cryst.* **B27**, 1740-1743 (1971).
[7] J. Rest et al., *U-Mo Fuels Handbook*, Argonne National Laboratory and Idaho National Laboratory (2006).
[8] A. E. Dwight et al., *Journal of Nuclear Materials* **2**, 81-87(1960).

The influence of surface topography on the initiation of uranium hydriding

Camilla Stitt[1], Richard A Crane[1], Christopher Jones[2], Thomas B Scott[2]

[1, 2] *Interface Analysis Centre, University of Bristol, Oldbury House, 121 St.Michael's Hill BS2 8BS Bristol, United Kingdom, e-mail: Camilla.stitt@bristol.ac.uk*

The safe long term containment of radioactive waste is an essential goal for the UK nuclear community. Safe packaging of legacy intermediate level wastes (ILW) in cement-based wasteforms for continued storage or disposal is reliant on research focused on the corrosion of uranium metal, particularly the hydriding potential and behavior in the storage environment. In the past 20 years the investigations into uranium hydriding has significantly advanced to determine kinetics, mechanisms, morphology and more recently the factors influencing hydride initiation sites. So far, it has been suggested that grain boundaries [1], oxide thickness [2] [3], carbides or inclusions [2] and the presence of external gases such as O_2 and CO [4] have a considerable effect on the location and incubation period of hydride initiation. In our work we have extended this research further to include the effects of the uranium surface topography, essentially examining geometrical effects on the initiation of hydride formation.

For the UK, waste containing natural uranium metal, largely contained in streams containing the waste arising from the reprocessing of first-generation nuclear fuel (Magnox swarf), are significant contributors to the overall inventory of ILW. After cooling, the Magnox fuel undergoes a decanning process by which the uranium rod is scraped out of the magnesium AL80 alloy cladding and separated for further processing and encapsulation. Due to the inefficiency of this method, residual uranium lumps can remain attached to the Magnox swarf, which exhibits variable morphology and a relatively high surface area. It is expected that uranium in waste storage environments is unlikely to consist of the flat coupons used in laboratory experiments, but instead present a rough surface featuring ridges, scratches and irregular topographical disturbances, arising as a result of previous mechanical handling associated with fuel reprocessing.

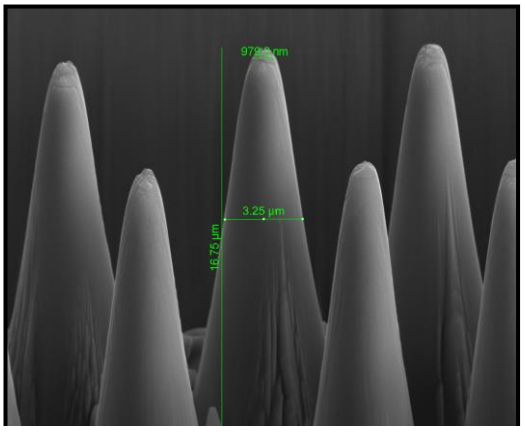

Fig 1. Ion beam milled pillars in natural uranium prior to hydriding

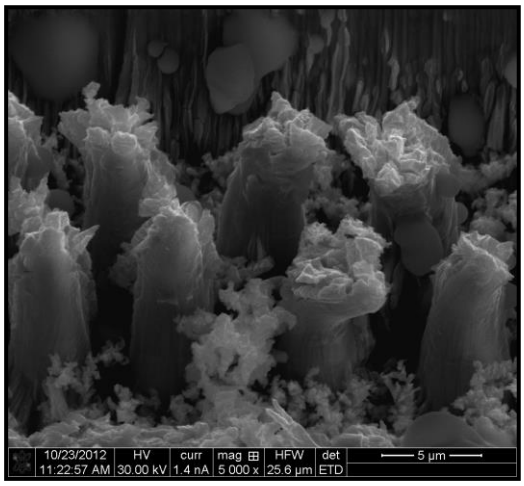

Fig 2. Natural uranium ion beam milled pillars after hydriding

We have carried out a fundamental study to further expand our understanding of the factors that affect hydride nucleation mechanisms and rates. The results presented clearly suggest that the surficial geometry of a metallic surface will influence the location of hydride nucleation centres and subsequently the rate at which these nucleation centres grow compared to a geometrically flat homogeneous surface. To investigate this, an array

of geometrically similar pillars was milled into a flat uranium surface using a Helios NanoLab 600i focused ion beam instrument (Fig. 1), and subsequently partially hydrided. The study aim was to determine the location of the first hydride nucleation sites. With a 1.5 mbar drop in the gas pressure of hydrogen, the uranium hydrides were first observed to initiate at the apex of the pillars (Fig. 2). With further exposure to hydrogen, the pillars were subsequently engulfed by the rapidly growing hydride before any of the bulk geometrically flat material had begun to nucleate visible hydride growths.

These findings are crucial, as they suggests that the incubation period for irregularly surfaced uranium found in nuclear waste is likely to be much shorted than previous laboratory results suggest. Furthermore, these rapidly growing growth centres may contribute to an overall faster corrosion rate than previously proposed, as the growth centres potentially become early, low energy pathways for further hydride formation.

References

[1] T.B. Scott et al., *Philosophical Magazine***177-187**, 87:2 (2007)
[2] R. Arkush et al., *Journal of Alloys and Compounds* **187-205**, 244 (1996)
[3] R.M. Harker, *Journal of Alloys and Compounds***106-117**, 426 (2006)
[4] J. Bloch et al., *Journal of Less-Common Metals* **371-383**, 139 (1988)

The influence of the temperature of preparation on the alpha/beta phase ratio of uranium hydride and on its rate of hydrolysis

Christopher John Broan,[1] David T. Goddard[1], Robin Orr[2], Hugh Godfrey[2], Andrew Diggle[3]

[1] *National Nuclear Laboratory: Building A709, Salwick Site, Preston, Lancashire PR4 0XJ, United Kingdom; cjb10@nnl.co.uk*
[2] *National Nuclear Laboratory*
[3] *Sellafield Limited*

The formation and properties of uranium hydride has been of interest within the nuclear industry for a considerable time owing to its relevance to storage and handling of uranium metal. Uranium hydride can form as either the α-UH_3 or β-UH_3 structure, with α-UH_3 only being formed as a significant fraction at low temperatures. Examination of the differences in the properties of these two phases has previously received relatively little attention.

In this study uranium hydride has been prepared by the reaction of dilute hydrogen with clean, bulk metal at temperatures between 30°C and 200°C and the resulting hydride characterised. The temperature of formation has been shown to have a significant effect on the fraction of the α-UH_3 phase which was produced. The alpha/beta ratio was found to vary smoothly and reproducibly with formation temperature (figure 1).
New results concerning the reaction kinetics of uranium hydride with liquid water under isothermal conditions will be presented. These show significant differences in the reaction kinetics of UH_3 samples formed at different temperatures. The rate of hydrolysis was consistently higher for hydride samples prepared under conditions which give rise to a higher proportion of α-UH_3. Evidence will also be presented that indicates the α-UH_3 phase is depleted preferentially during the initial stages of the reaction.

The results highlight that extrapolation of results obtained using uranium hydride prepared at high temperatures to hydride formed at temperatures more typically experienced during, for instance, uranium storage may need to be carried out with caution.

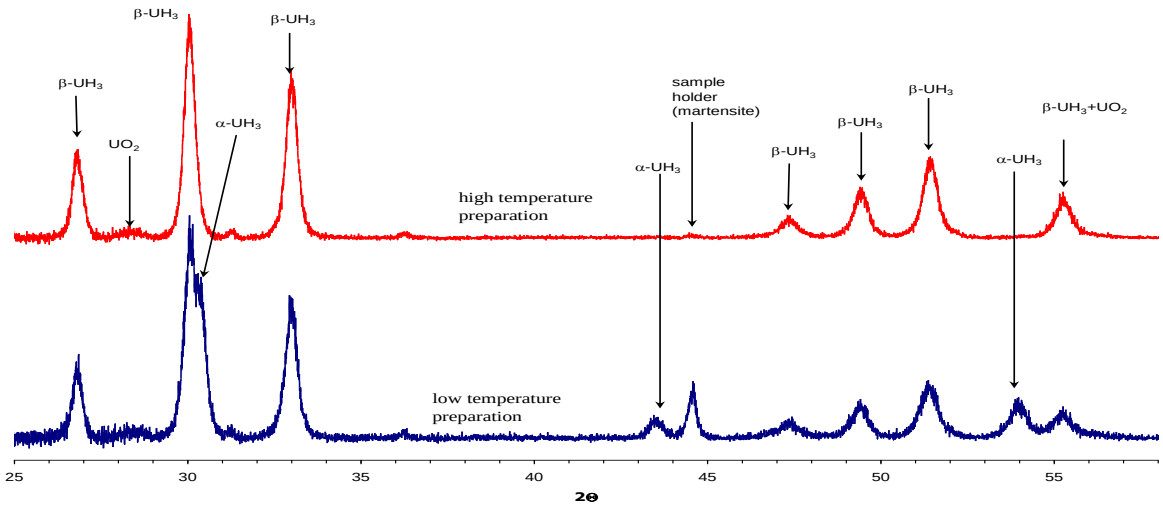

Figure 3: powder X-ray diffraction results for uranium hydride prepared at high and low temperature

A New Concept in Radiation Damage Studies: System Model for Self-Irradiation Experiments in Th-doped PbSe and PbS Thin Films

Michael Shandalov[1], Itzhak Kelson[2] and Eyal Yahel[1]

[1]*Department of Physics, Nuclear Research Center Negev, POB 9001 Beer Sheva 8419001, Israel, e-mail: michash@outlook.com*
[2]*School of Physics, Tel Aviv University, POB 39040 Tel Aviv 6997801, Israel*

In this work we present a new concept for investigating radiation damage in thin films by using internal radiation source rather than external radiation source. The common way to alloy metals with radioactive actinides is melting two or more pure elements in an arc furnace, which requires considerable amounts of actinide metals with high activity. High activity of actinides and their toxicity require sealed enclose such as glovebox for their handling. Controlled doping of the thin films with small amounts (100-200 ppm) of radioactive elements such as thorium is expected to provide a unique path for studying radiation damage in materials without need of sealed enclosure. At the first stage of this work, we developed a chemical bath deposition (CBD) process[1-3] for controlled doping of PbSe and PbS thin films (~100 nm thick) with the stable isotope ($t_{1/2}$~10^6 years), ^{232}Th. This was achieved by altering deposition parameters such as temperature, reagent concentrations and time. The resulting Th-doped films were characterized using x-ray diffraction, which indicated a single phase material. Energy dispersive spectroscopy (EDS) mapping in the analytical transmission electron microscope (A-TEM), x-ray photoelectron spectroscopy (XPS) and secondary ion mass spectroscopy (SIMS) depth profiles indicated that the Th ions were homogeneously distributed throughout the film, suggesting Pb substitution by Th ions in the crystal lattice. In conclusion, a simple, controllable and cost-effective process for doping of PbSe and PbS thin films with Th has been successfully developed. In the next stage of the research, substitution of the stable isotope of Th with radioactive ^{228}Th should provide a novel route to radiation damage studies.

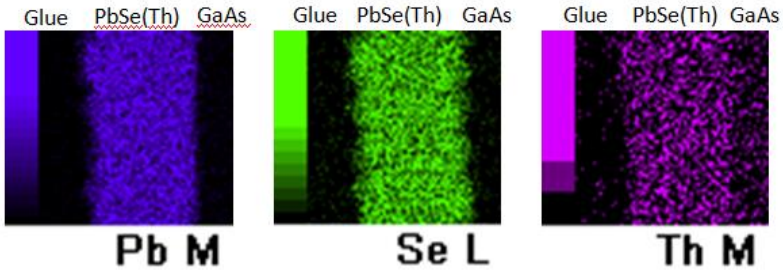

Fig. 1. EDS composition maps of Th-doped PbSe thin film showing homogeneous Th distribution throughout the film.

References

[1] G. Hodes, Chemical Solution Deposition of Semiconductor Films, M. Dekker, New-York, 12-225 (2003).
[2] M. Shandalov and Y. Golan, *The European Physics Journal - Applied Physics*, **24**, 13 **(**2003).
[3] A. Osherov and Y. Golan, Chemical Epitaxy of Semiconductor Thin Films, *MRS Bulletin*, **35**, 790 (2010).

Evidence for persistent spin-fluctuations in uranium sesquicarbide

R. Eloirdi[1], A.J. Fuchs[1], J.-C. Griveau[1], E. Colineau[1],
A. B. Shick[1,2], D. Manara[1] and R. Caciuffo[1]

[1] European Commission, Joint Research Centre, Institute for Transuranium Elements, Postfach 2340, D-76125 Karlsruhe, Germany, e-mail: rachel.eloirdi@ec.europa.eu
[2] *Institute of Physics, ASCR, Na Slovance 2, CZ-18221 Prague, Czech Republic*

The low-temperature magnetic susceptibility, heat capacity and electrical resistivity of uranium sesquicarbide have been estimated down to 2 K by combining measurements carried out on samples of U_2C_3, containing UC as minority phase, and on pure UC specimens. The presence of spin fluctuations [1-2] with characteristic temperature T_{SF} = 7 K is revealed by a nonanalytic contribution to the specific heat behaving (well below T_{SF}) as $T^3 ln(T=T_{SF}$), and confirmed by a T^2 increase of the electrical resistivity and a 1 - κT^2 decrease of the low-temperature magnetic susceptibility. The analysis of the specific heat data above T_{SF} provides a Debye temperature $\Theta_D \approx$ 256 K and a moderately high value of the Sommerfeld coefficient, $\gamma \approx$ 42.4 mJmol $_U{}^{-1}$ K^{-2}. The zero-temperature many-body enhancement of the electron mass is found to be $m^*/m \approx$ 2.7. Our data rule out the occurrence of magnetic ordering in U_2C_3. First principles electronic structure calculations [3] (Figure 1) support the absence of a magnetically ordered ground state but suggest that dynamical spin fluctuations are responsible for the electron mass enhancement.

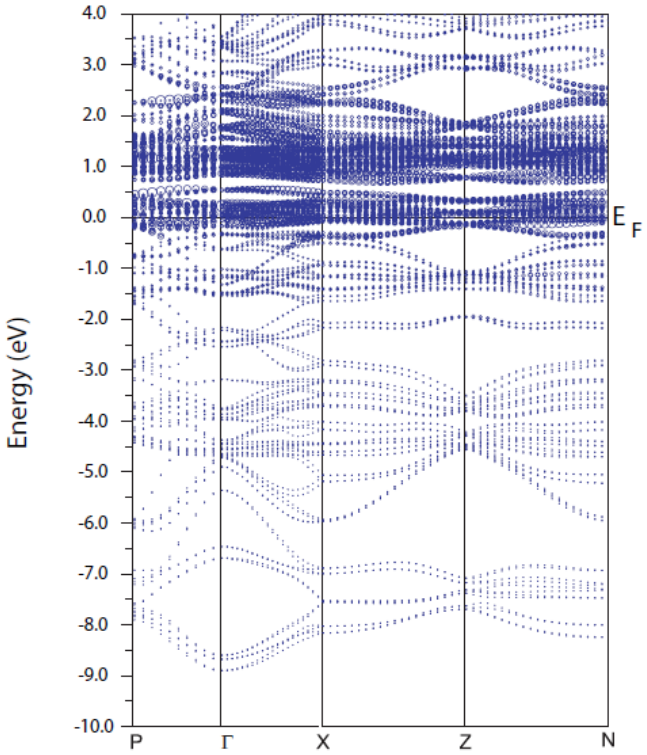

Fig. 1. Band structure with f-weight fatbands for U_2C_3.

References

[1] R.J. Trainor, M.B. Brodsky, H.V. Culbert, Phys. Rev. Lett. **34**, 1019 (1975).
[2] M.B. Brodsky, Rep. Prog. Phys., **41**, 1547 (1978).
[3] A.B. Shick, D.L. Novikov and A.J. Freeman, Phys. Rev. B **56**, R14259 (1997).

X-ray magnetic circular dichroism experiments and theory of transuranium Laves phase compounds

F. Wilhelm[1], R. Eloirdi[2], J. Rusz[3], R. Springell[1,4], E. Colineau[2], J.-C. Griveau[2], P. M. Oppeneer[3], R. Caciuffo[2], A. Rogalev[1] and G. H. Lander[2]

[1]*European Synchrotron Radiation Facility (ESRF), B.P.220, F-38043 Grenoble, France*
e-mail: wilhelm@esrf.fr
[2]*European Commission, Joint Research Centre, Institute for Transuranium Elements, Postfach 2340, D-76125 Karlsruhe, Germany*
[3]*Department of Physics and Astronomy, Uppsala University, Box 516, S-75120 Uppsala, Sweden*
[4]*Royal Commission for the Exhibition of 1851 Research Fellow, Interface Analysis Centre, University of Bristol, Bristol BS2 8BS, United Kingdom*

The actinide cubic Laves compounds $NpAl_2$, $NpOs_2$, $NpFe_2$, and $PuFe_2$ have been examined by X-ray magnetic circular dichroism (XMCD) at the actinide $M_{4,5}$ absorption edges and Os $L_{2,3}$ absorption edges. They have the interesting feature that the An−An spacing is close to the so-called Hill limit so that substantial hybridization between the 5*f* states on neighboring atoms is expected to occur. The XMCD experiments performed at the $M_{4,5}$ absorption edges of Np and Pu allow us to determine the spectroscopic branching ratio, which gives information on the coupling scheme in these materials. In all materials the intermediate coupling scheme is found appropriate. Comparison with the SQUID data for $NpOs_2$ and $PuFe_2$ allows a determination of the individual orbital and spin magnetic moments and the magnetic dipole contribution m_{md}. The resulting orbital and spin magnetic moments are in good agreement with earlier values determined by neutron diffraction [1-3], and the values of m_{md} are non-negligible, and close to those predicted for intermediate coupling. There is a comparatively large induced moment on the Os atom in $NpOs_2$ such that the Os contribution to the total moment per formula unit is ∼30% of the total. The spin and orbital moments at the Os site are parallel, in contrast to the anti-parallel configuration anticipated from Hund's 3rd rule. Calculations using the LDA+U technique are reported. The *ab initio* computed XMCD spectra show good agreement with experimental spectra for small values (0-1eV) of the Hubbard U parameter, which underpins that 5*f* electrons in these compounds are relatively delocalized. The calculations confirm the sign and magnitude of the experimentally determined induced magnetic moments on the Os site in $NpOs_2$.

References

[1] A. T. Aldred, B. D. Dunlap, and G. H. Lander, *Phys. Rev. B* **14**, 1276 (1976).
[2] G. H. Lander, A. T. Aldred, B. D. Dunlap, and G. K. Shenoy, *Physica B* **86-88**, 152 (1977).
[3] M. Wulff, G. H. Lander, J. Rebizant, J. C. Spirlet, B. Lebech, C. Broholm, and P. J. Brown, *Phys. Rev. B* **37**, 5577 (1988).

Exchange bias in UO_2/Fe_3O_4 bilayers

Zhaohui Bao[1], Evgeniya Tereshina[2], Christian Kübel[3], Stanislav Daniš[4], Ladislav Havela[4], Thomas Gouder[1], Roberto Caciuffo[1]

[1] *European Commission, Joint Research Centre, Institute for Transuranium Elements, Postfach 2340, DE-76125 Karlsruhe, Germany*

[2] *Institute of Physics ASCR, Na Slovance 2, 18221 Prague, Czech Republic e-mail: teresh@fzu.cz*

[3] *Institute of Nanotechnology, Karlsruhe Institute of Technology, Hermann-von-Helmholtz-Platz 1, 76344 Eggenstein-Leopoldshafen, Karlsruhe, Germany* [4] *Faculty of Mathematics and Physics, Charles University, Ke Karlovu 5, 12116 Prague, Czech Republic*

Magnetic properties of uranium-based compounds range between localized and itinerant depending on the character of the 5*f* electronic states (for overview see e.g. Ref. [1]). Despite the fact that U metal itself is non-magnetic, preparation of it in a form of a multilayer allowed observation of a significant polarization of U 5*f* electrons in e.g. U/Fe [2]. Large magnetic anisotropy together with other fascinating properties of uranium-based compounds imply that an important fundamental work can be done on the studies of "exchange anisotropy" effects while using the magnetic uranium-based layer/s in the antiferromagnetic/ferromagnetic (AFM/FM) bilayers. This "exchange anisotropy" is commonly known as an exchange bias (EB) effect [3] and consists of a shift of the hysteresis loop along the magnetic field axis in the AFM/FM (or ferrimagnetic) systems.

This work focuses on the low-dimensional magnetic properties of uranium dioxide UO_2 - an important material in science and technology. Bulk magnetism of UO_2 has been largely investigated [4]. The U^{4+} magnetic moments of UO_2 are localized and the compound orders antiferromagnetically below the Néel temperature T_N = 30.8 K. The transition metal oxide Fe_3O_4 (Curie temperature T_C = 858 K) was chosen as the ferrimagnetic component of the multilayer due to a reasonable mismatch of the lattice constants a_{UO2} and Fe_3O_4 (~1.9% in the [110] direction). The samples with various thicknesses of the layers have been grown by reactive sputter deposition. In addition, the single layers of magnetite were also obtained. The stoichiometry of deposited layers was confirmed by X-ray Photoelectron Spectroscopy. The samples were attested using High-Resolution X-ray Diffraction, X-ray reflectivity and High-Resolution Transmission Electron Microscopy. The magnetic study on UO_2/Fe_3O_4 bilayers has been performed using a vibrating sample magnetometer on PPMS9 installation (Quantum Design). The exchange coupling mechanism was investigated by measuring the temperature evolution of the hysteresis

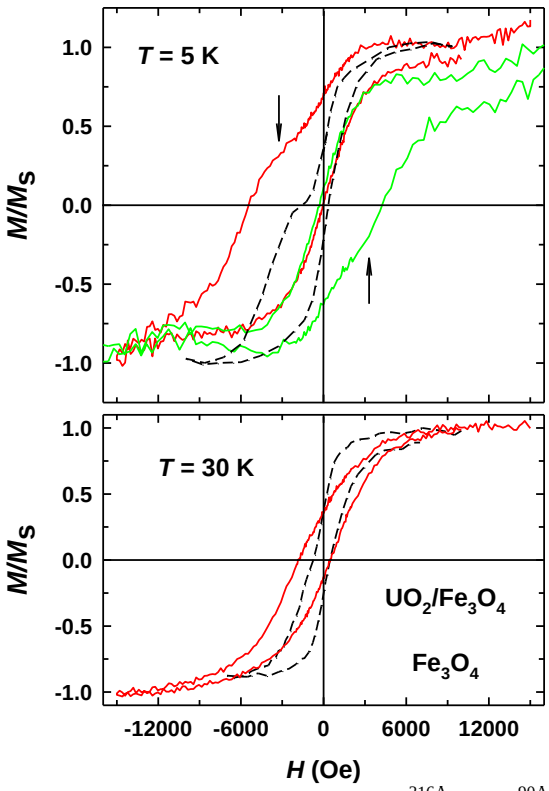

Fig. 1. FC magnetization data for $UO_2^{316Å}/Fe_3O_4^{90Å}$ at 5 and 30 K (red and green lines correspond to + 1 and –1 T cooling field). FC data for $Fe_3O_4^{90Å}$ (broken line) is shown for comparison.

loops under various cooling conditions. The standard torque magnetometry was employed for the study of magnetic anisotropy variation in the bilayers at different temperatures.

The magnetic study showed that the UO_2/Fe_3O_4 systems are exchange-biased with the largest values of exchange bias field (H_{EB}) reaching out ~2000 Oe at 5 K in the sample with the thinnest Fe_3O_4 layer (Figs. 1 and 2). The study of a single magnetite layer of the same thickness suggests that up to ~600 Oe of H_{EB} in UO_2/Fe_3O_4 might "come" from the magnetite itself that is plausibly caused by different magnetic behavior of a large fraction of surface spins in Fe_3O_4 as compared to those within the layer. H_{EB} is roughly inversely proportional to the thickness of a ferromagnetic layer t_{Fe3O4} (Fig. 2) Strongly asymmetric hysteresis loops both in zero-field cooling (ZFC) and field-cooling modes (FC) were observed that can be possibly connected with different magnetization reversal mechanisms during the magnetizing-demagnetizing process. Kinks in the magnetization curves (shown with arrows in Fig. 1) are found for various film orientations. The field/magnitude of the observed kinks does not depend significantly on the cooling field value.The work has been supported by the grant GACR reg. number 13-25866P of the Czech Science Foundation.

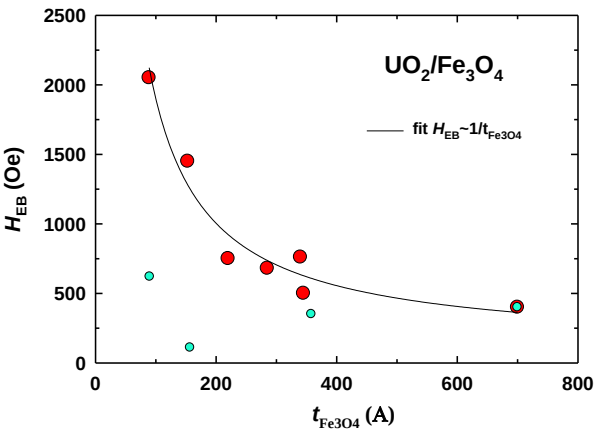

Fig. 2. Dependence of exchange bias field on the Fe_3O_4 layer thickness in UO_2/Fe_3O_4 bilayers (red dots) at 5 K and the H_{EB} values for the corresponding Fe_3O_4 monolayers (green dots).

References

[1] V. Sechovsky, L. Havela, in: *Magnetic Materials*, K.H.J. Buschow (Ed.), Elsevier, Amsterdam, 1998, Vol. 11, p. 1.
[2] R. Springell et al., Phys. Rev. B **77**, 064423 (2008).
[3] W. H. Meiklejohn and C. P. Bean, Phys. Rev. B **102**, 1413 (1956).
[4] P. Santini et al., *Rev. Mod. Phys.* **81**, 807 (2009).

New ternary compounds $U_3Si_2H_{1.8}$ and UNiZn and their properties

Maskova S.[1], Havela L.[1], Danis S.[1]

[1] *Department of Condensed Matter Physics, Charles University, Ke Karlovu 5, 12116 Prague 2, The Czech Republic, e-mail: maskova@mag.mff.cuni.cz*

We have been studying crystal structure, magnetic properties and possibility of hydrogen absorption in many U_2T_2X compounds [1]. As U_3Si_2 intermetallic compound is a "mother compound" of highly studied U_2T_2X compounds, as their crystal structure is the ordered variant of U_3Si_2 type, we also tried to hydrogenate this compound. During the study of U_2T_2X -family of compounds new unreported compound UNiZn was found.

U_3Si_2 is often used as a nuclear fuel in Low-Power Research Reactors, that is why its stability, mainly to hydrogen, is so important. We have studied its stability against hydrogen and also the change of crystal structure and magnetic properties. Uranium compounds usually need high H pressure (≈ 100 bar) for hydrogenation [2], it was therefore suprizing to see that the parent compound U_3Si_2 can be hydrogenated at very low H_2 pressure, yielding $U_3Si_2H_{1.8}$. This fact was found during the controlled temperature-induced desorption experiment on $U_3Si_2H_{1.8}$, which was placed in an evacuated calibrated volume and heated using a constant heating rate 2 K/min. After the sample is heated it is left to spontaneously cool down. In the case of $U_3Si_2H_{1.8}$, decreasing temperature leads evidently to a re-absorption even if the H pressure is low, on the scale of mbar (fig.1). The H concentration corresponds to U_2T_2X compounds with H concentration slightly below the nominal 2 H/f.u., achieved when filling adjacent U_3T tetrahedra up to 50 %.

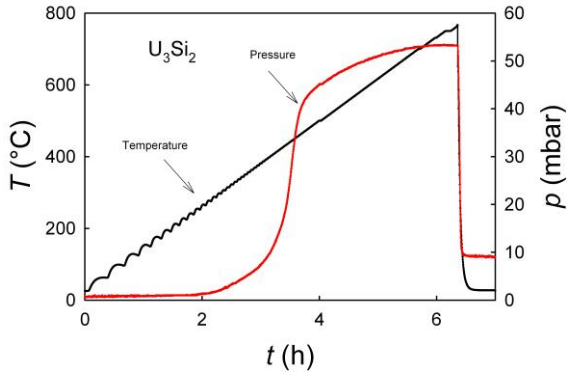

Fig. 1. The record of development of temperature and pressure during the desorption experiment performed on $U_3Si_2H_x$.

The shortest inter-uranium distance in the parent compound is found in the basal plane (d_{U-U} = 3.319 Å). This value is much lower than the Hill limit (3.4 – 3.6 Å) corroborating the results of previous experiments which show that U_3Si_2 is a weak Pauli paramagnet [3,4]. In the hydride the shortest d_{U-U} is expanded reaching the value close to the Hill limit. The hydride was found to be a spin fluctuator with temperature dependent magnetic susceptibility much higher than for the parent compound. The temperature dependence of magnetic susceptibility (fig. 3.) shows a field-dependent upturn at low temperatures. On field dependence of magnetization (fig. 2) formation of weak remnant magnetization is visible. Absence of well-defined T_C (either intrinsic or impurity) gives impression of ferromagnetic clusters due to randomness of H occupancy.

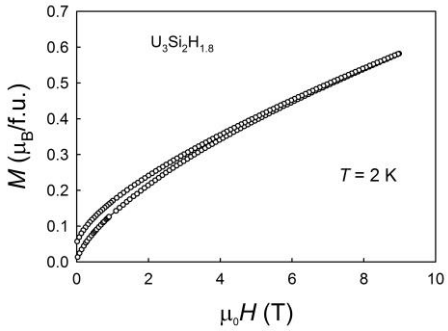

Fig. 2. Field dependence of magnetization of $U_3Si_2H_{1.8}$ measured at T = 2 K.

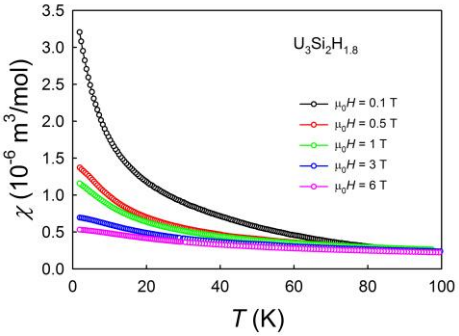

Fig. 3. Temperature dependence of magnetic susceptibility of $U_3Si_2H_{1.8}$ measured in various magnetic fields.

The new compound UNiZn crystallizes in hexagonal ZrNiAl type of structure (d_{U-U} = 3.430 Å in the basal plane). It was found to have a paramagnetic ground state. It can be considered as a spin fluctuator with low but temperature dependent susceptibility (fig.4.). Hydrogenation of UNiZn was found to be extremely sensitive to the temperature. The high-temperature synthesis leads to so called HDDR process (hydrogenation – disproportionation – desorption – recombination). Upon hydrogenation the sample was decomposed to β-UH_3, Zn and another so far unknown phase. After the hydrogen is desorbed, the initial UNiZn compound is restored. On the other hand the low-temperature synthesis is irreversible. The crystal structure is changed upon hydrogenation to AlB_2 structure type (space group *P*6/*mmm*). Upon hydrogenation the crystal lattice is expanded in such way that the shortest U-U distance (d_{U-U} = 3.95 Å) is now much higher than the Hill limit what allows magnetic ordering in the hydride. The low-temperature hydride is antiferromagnet with the Néel temperature approx. 50 K (fig.5.).

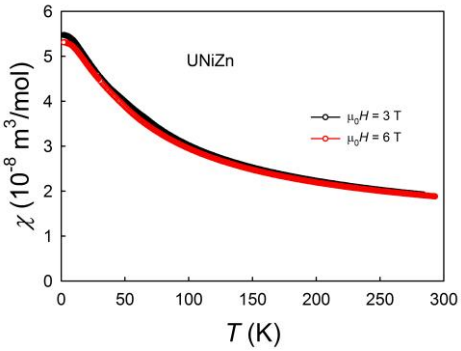

Fig. 4. Temperature dependence of magnetic susceptibility measured in μ_0H = 3 and 6 T.

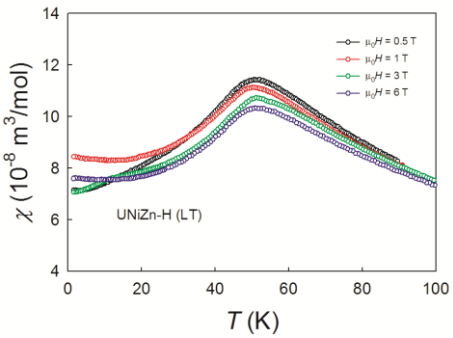

Fig. 5. Temperature dependence of magnetic susceptibility of "low temperature" hydride UNiZn-H measured in various magnetic fields.

References

[1] L. Havela, V. Sechovsky, P. Svoboda, H. Nakotte, K. Prokes, F.R. de Boer, A. Seret, J.M. Winand, J. Rebizant, J.C. Spirlet, A. Purwanto, R.A. Robinson, J. Magn. Magn. Mat. 140-144, 1367 (1995).
[2] K. Miliyanchuk, L. Havela, A.V. Kolomiets, A.V. Andreev, *Phys.* B 359–361, 1042 (2005).
[3] K. Remschnig, T. Le Bihan, H. Noel and P. Rogl, J. Solid State Chemistry 97, 391 (1992).
[4] T. Miyadai, H. Mori, T. Oguchi, Y. Tazuke, A. Amitsuka, T. Kuwai and Y. Miyako, J. Mag. Mag. Mat. 104-107, 47 (1992).

A single crystal study of $U_3Fe_4Ge_4$

D.I. Gorbunov[1,2], M.S. Henriques[3], J.C. Waerenborgh[3], L. Havela[2], A.V. Andreev[1], Y. Skourski[4], A.P. Gonçalves[3]

[1]*Institute of Physics, Academy of Sciences of the Czech Republic, Na Slovance 2, 182 21 Prague, Czech Republic, e-mail:* gorbunov@fzu.cz
[2]*Department of Condensed Matter Physics, Faculty of Mathematics and Physics, Charles University, Ke Karlovu 5, 121 16 Prague, Czech Republic*
[3]*IST/ITN, Instituto Superior Técnico, UTL, CFMC-UL, Estrada Nacional 10, 2686-953-Sacavém, Portugal*
[4]*Dresden High Magnetic Field Laboratory, Helmholtz-Zentrum Dresden Rossendorf, D-01314 Dresden, Germany*

The magnetism of intermetallic compounds based on uranium and 3*d* metals *T* is mainly determined by the 5*f*-3*d* hybridization. It acts to delocalize the 5*f* electrons leading to a reduction or even disappearance of the U magnetic moment. Simultaneously, the 3*d* magnetic moment might vanish as well (see, e.g., UFeAl [1] or UFeGe [2] which display paramagnetic behavior down to the lowest temperatures). Nevertheless, U-*T* compounds exist where at least one sublattice is magnetic. An example is provided by a hexagonal Laves phase U_2Fe_3Ge found recently in the ternary U-Fe-Ge phase diagram at 900°C [3,4]. In spite of the shortest U-U distances $d_{U\text{-}U} \leq 3.2$ Å in U_2Fe_3Ge, the compound is a ferromagnet with the magnetism originating entirely from the U sublattice, and thus constitutes an exception to the Hill rule. Another compound discovered in the U-Fe-Ge system is a ferromagnet $U_3Fe_4Ge_4$ crystallizing in the orthorhombic $Gd_3Cu_4Ge_4$ structure type (space group *Immm*) [5]. The present work reports magnetic, thermal and transport properties of a $U_3Fe_4Ge_4$ single crystal.

The magnetization curves along the principal crystallographic directions of the $U_3Fe_4Ge_4$ single crystal measured in steady (up to 14 T) and pulsed (up to 60 T) fields are shown in Fig. 1. Along the *a* axis the compound displays a spontaneous magnetic moment equal to M_s = 1.2 μ_B/f.u., and there are no spontaneous components along the other axes. There is also anisotropy between the *b* and *c* axes, the *c* axis is the hard-magnetization direction. As typical of intermetallics with two-ion hybridization-induced anisotropy, the magnetic moments in $U_3Fe_4Ge_4$ are oriented perpendicular to the shortest U-U links $d_{U\text{-}U}$ = 3.637 Å which are along the *c* axis. Different behavior of magnetization along the *a*, *b* and *c* axes reflects high magnetic anisotropy in $U_3Fe_4Ge_4$ also characteristic of uranium intermetallics. The magnetization *M* along the easy *a* axis still grows rather intensively after the domain-wall motion is completed, and a tendency towards saturation appears in a high field. In 60 T the average magnetic moment per U atom is about 1 μ_B. Almost the same value is observed along the *b* and *c* axes due to the high susceptibility d*M*/d*H*. Such a high susceptibility may be understood within the

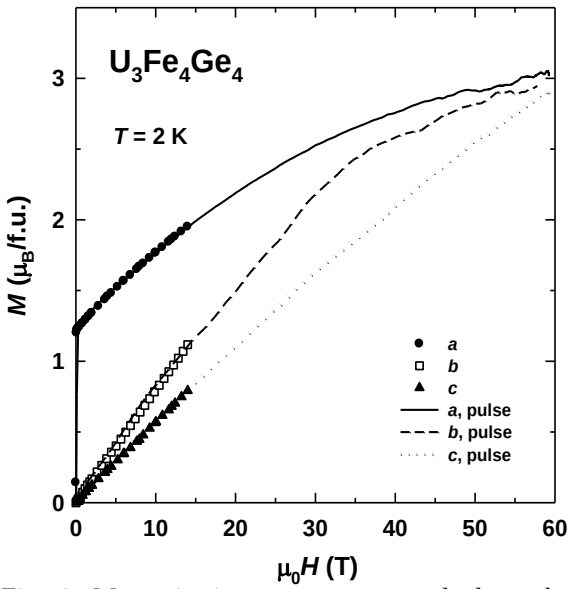

Fig. 1. Magnetization curves measured along the principal axes of the $U_3Fe_4Ge_4$ single crystal in pulsed magnetic fields at *T* = 2 (lines). The symbols represent steady-field results.

framework of itinerant magnetism of $U_3Fe_4Ge_4$ as additional splitting of spin-up and spin-down subbands in an external field.

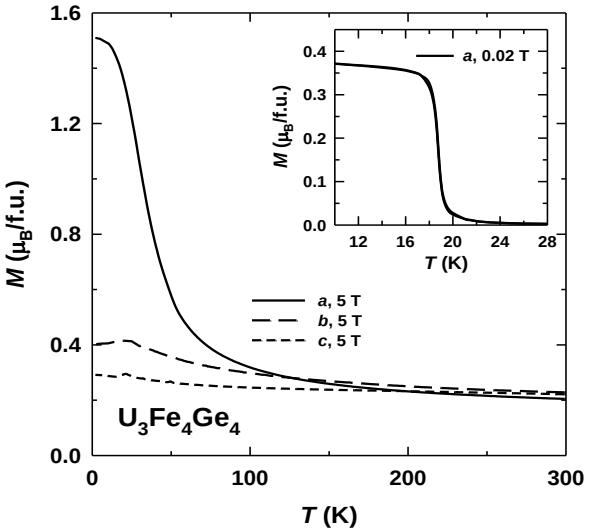

Fig. 2. Temperature dependence of magnetization along the principal axes of the $U_3Fe_4Ge_4$ single crystal in a magnetic field of 5 T. The inset shows the temperature dependence of magnetization along the *a*

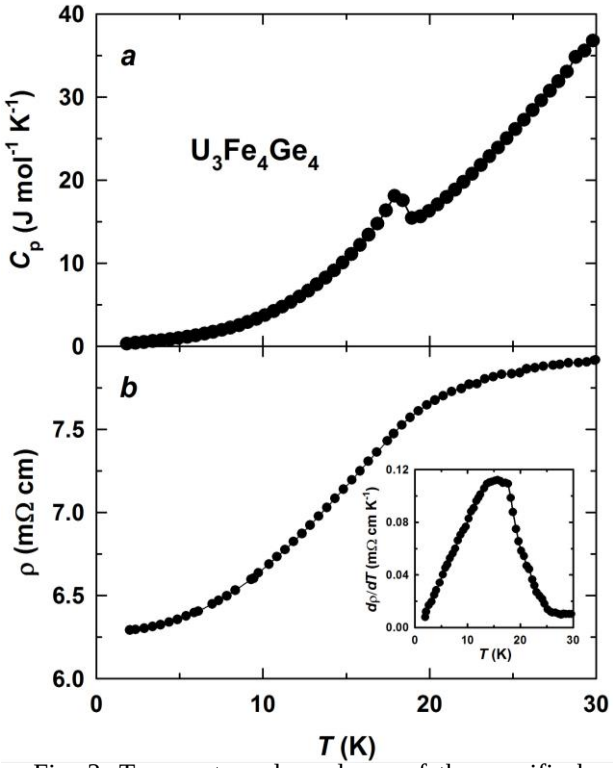

Fig. 3. Temperature dependence of the specific heat (*a*) and of the electrical resistivity (*b*) of the $U_3Fe_4Ge_4$ single crystal. The inset shows the first temperature derivative of the electrical resistivity.

The *a*-axis magnetization measured as a function of temperature in a field of 5 T strongly increases at low temperatures (Fig. 2), indicating the onset of ferromagnetic order. The Curie temperature of $U_3Fe_4Ge_4$ is T_C = 18 K, found as the inflexion point in the $M(T)$ dependence in 0.02 T (inset in Fig. 2). The magnetization along the *b* and *c* axes displays much lower values.

The low magnetic ordering temperature and the high magnetic anisotropy suggest that the magnetism of $U_3Fe_4Ge_4$ is to a great extent associated with uranium. Moreover, Mössbauer spectroscopy also performed in the present work excluded long-range magnetic ordering as well as spin-glass behavior within the Fe sublattice**.**

The specific heat C_p of $U_3Fe_4Ge_4$ displays a λ-type anomaly related to the magnetic phase transition at T_C = 18 K (Fig. 3*a*). At $T < T_C$ the magnetic contribution to the specific heat shows a gap excitation behavior with Δ = 4 meV. The electronic contribution to C_p is γ = 57 mJ/(mol-U K^2) in the magnetically-ordered state and much higher in the paramagnetic state, γ = 145 mJ/(mol-U K^2). The electrical resistivity ρ, albeit very high, decreases in the vicinity of the magnetic phase transition (Fig. 3*b*). The first temperature derivative, $d\rho/dT$, shows that the phase transition occurs at T_C = 18 K (inset in Fig. 3*b*), in agreement with the magnetization and specific heat data.

References

[1] R. Troć, V. H. Tran, F. G. Vagizov, H. Drulis, *J. Alloys Compd.* **200**, 37 (1993).
[2] L. Havela, A. Kolomiets, V. Sechovský, M. Diviš, M. Richter, A.V. Andreev, *J. Magn. Magn. Mater.* **177-181**, 47 (1998).
[3] M.S. Henriques, O. Tougait, H. Noël, L.C.J. Pereira, J.C. Waerenborgh, A.P Gonçalves, *Sol. State Commun.* **148**, 159 (2008).
[4] M.S. Henriques, D. I. Gorbunov, J.C. Waerenborgh, L. Havela, A.B. Shick, M. Diviš, A.V. Andreev, A.P. Gonçalves, *J. Phys.: Cond. Matter* **25**, 066010 (2013).
[5] D. Berthebaud, O. Tougait, M. Potel, E.B. Lopes, J.C. Waerenborgh, A.P. Gonçalves, H. Noël, *J. Alloys Compd.* **554**, 408 (2013).

Electronic and Magnetic Properties of $NpNi_5$.

A. Hen,[1,2] E. Colineau,[1] R. Eloirdi,[1] J.-C. Griveau,[1] J.-P. Sanchez,[5]
A. B. Shick,[1,6] I. Halevy,[2,3,4] I. Orion,[2] and R. Caciuffo[1]

[1]*European Commission, Joint Research Centre, Institute for Transuranium Elements, Postfach 2340, D-76125 Karlsruhe, Germany*
E-mail: halevyi@caltech.edu
[2]*Nuclear Engineering Department, Ben Gurion University, IL84105 Beer-Sheva, Israel*
[3]*Physics Department, Nuclear Research Center Negev, P.O. Box 9001, IL84190 Beer-Sheva, Israel*
[4]*California Institute of Technology, W. M. Keck Laboratory 138-78, Pasadena, California 91125, USA*
[5]*SPSMS, UMR-E CEA/UJF-Grenoble 1, INAC, FR-38054 Grenoble, France*
[6]*Institute of Physics, Academy of Sciences of the Czech Republic, Na Slovance 2, CZ-182 21 Prague, Czech Republic*

The physical properties of binary actinides and transition metal alloys are of great importance for the safety assessment of nuclear fuels. Since transition metals are major components of the cladding material of fuel rods (stainless steel, HT-9 etc.), the physical properties of those compounds formed by accidental fuel-cladding interactions could have limiting factors on the fabrication, life time operation and disposal of nuclear fuels. Binary compound of the form ReT_5 (Re = rare earth, T = Transition metal) has been in the focus of interest mainly because of their magnetic properties (small Re to T stoichiometric ratio, large spontaneous magnetization and high Curie temperature) and their ability to store large amount of hydrogen per formula unit (f. u.)

Reported in 1997 [1], $NpNi_5$ was synthesized and identified to have hexagonal (D_2d) $CaCu_5$ crystallographic structure, with room-temperature lattice parameters a = 8.3107(1) Å and c = 8.1058(1) Å. In the present study, $NpNi_5$ has been synthesized and characterized by means of powder x-Ray diffraction (**Errore. L'origine riferimento non è stata trovata.** left panel), Superconducting – Quantum – Interference – Device magnetometry (SQUID, **Errore. L'origine riferimento non è stata trovata.** right panel), ^{237}Np Mössbauer spectroscopy [2] (**Errore. L'origine riferimento non è stata trovata.** left panel) and specific heat measurements (**Errore. L'origine riferimento non è stata trovata.** right panel).

Magnetization curves indicate that $NpNi_5$ is a ferromagnet (T_C ~ 16 K), fit of the paramagnetic part to the Curie–Weiss law (C~1.7 emu·K/mol, θ_P ~ 14.6 K) gives an effective moment μ_{eff} ~ 3.7 μ_B per f.u. – no magnetization hysteresis was observed. The isomer shift (δ_{IS} ≈ -11.1 mm/s vs. $NpAl_2$) observed in Mössbauer spectra suggests a tetravalent Np state, but considering the influence of conduction electrons we determine a Np^{3+} ($5f^4$ configuration) oxidation state. The hyperfine field determined by fitting of the spectra (~439T) gives an ordered moment at the Np site μ_{Np} ~ 2 μ_B per Np ion (1 μ_B = 215 T [3]). The magnetic transition is clearly visible in the temperature dependence of the specific heat, and a magnetic phase diagram as a function of temperature and external magnetic field was generated.

In this communication we will present the results obtained and discuss them in the light of theoretical considerations.

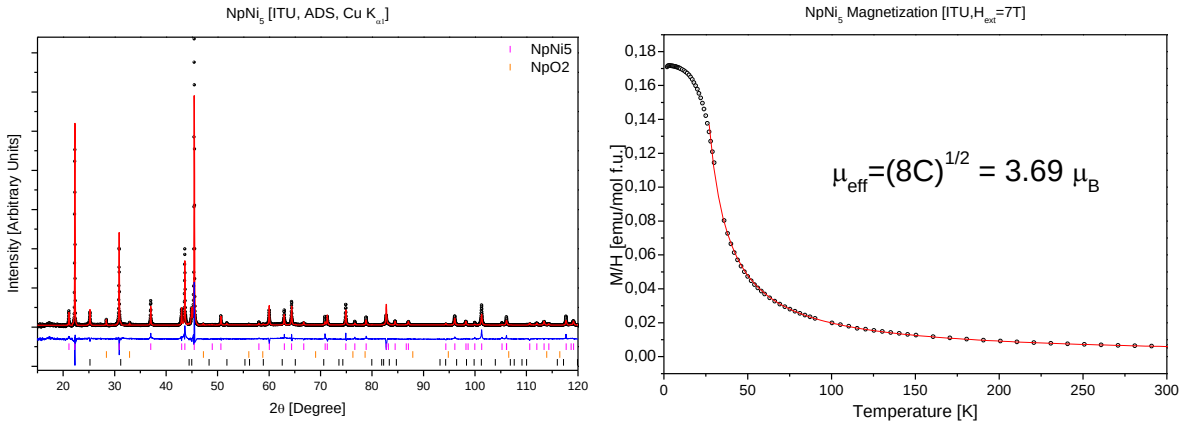

Fig. 1 Left: Powder x-ray diffraction pattern of $NpNi_5$, black dot – measured data, red line – fitted profile, blue line – difference profile, vertical tick – angular position of Bragg peaks. Right: Temperature dependence of the magnetic susceptibility, red line – fit to the Curie-Weiss law.

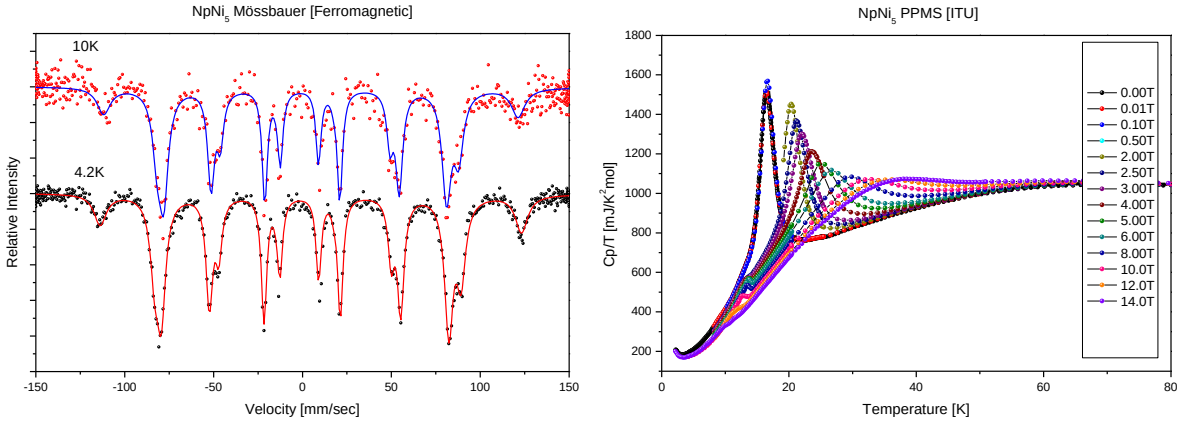

Fig. 2 Left: Mössbauer spectra taken in the ferromagnetic region, dots – measured data, lines – fits of hyperfine fields to the measured data, spectrum is composed of one hyperfine field as expected from the crystallography.

Right: Normalized heat capacity as a function of temperature in various external magnetic fields.

Acknowledgements

The high purity Np metals required for the fabrication of the compound were made available through a loan agreement between Lawrence Livermore National Laboratory and ITU, in the frame of a collaboration involving LLNL, Los Alamos National Laboratory and the US Department of Energy.

References

[1] M. Akabori et al. , Journal of Alloys and Compounds 257 (1997) 268-272.

[2] R.L. Mössbauer., Zeitschrift für Physik, Bd. 151, S. 124-143 (1958).

[3] B. D. Dunlap and G. M. Kalvius, in Handbook on the Physics and Chemistry of the Actinides,

edited by A. J. Freeman and G. H. Lander (North-Holland, Amsterdam, 1985), Vol. 2, p. 32

Observations and characterisation of a Pu-0.18 wt. % Ga alloy

D.W. Wheeler, R.F.E. Jenkins, P. Roussel, R.K.B. Gover, M.B. Matthews

AWE, Aldermaston, Reading, Berkshire, RG7 4PR, U.K.

Since the Plutonium-Gallium (Pu-Ga) phase diagram was first published in 1964 [1], Ga has become one of the most widely studied δ-stabilising elements. Approximately 0.3 wt. % Ga is required to retain the δ-Pu phase to ambient temperature [2]; however, the stability of the δ-Pu phase in an alloy of this composition is tenuous. Transformation to the α-Pu phase will take place if the alloy is cooled to sub-ambient temperatures [3] or subjected to deformation, for example uniaxial or hydrostatic compression [4]. For Pu-Ga alloys containing less than approximately 0.3 wt. % Ga the alloying element content is insufficient to retain a wholly δ-Pu phase at ambient temperature, though the precise composition is unclear. Although a number of studies [5-10] have examined the δ→α' transformation in Pu-Ga alloys, the nature and properties of Pu alloys with a Ga content of less than 0.3 wt. % have not been reported so extensively. For this reason, the present study was carried out to examine a Pu alloy with a Ga content in this range in order to ascertain its structure and properties.

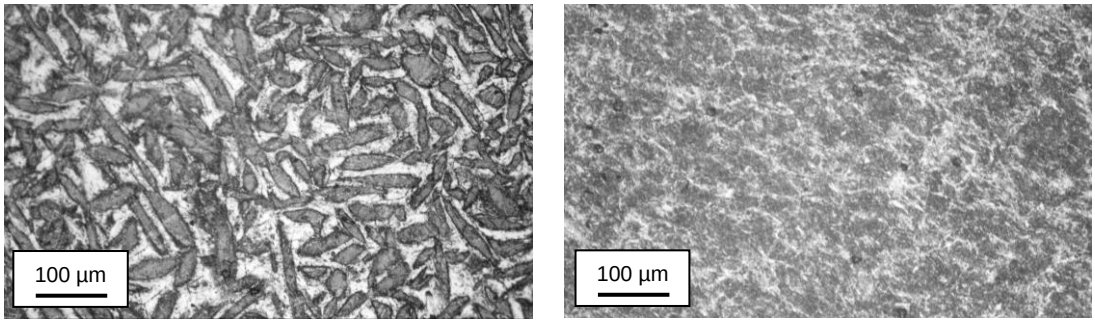

Fig. 1: Optical micrographs of the Pu-0.18 wt.% Ga alloy in the as-cast condition (left) and following a heat treatment at 450 °C for 250 hours (right).

A cast Pu-0.18 wt. % Ga alloy was characterised, both in the as-cast condition as well as following an homogenising heat treatment of 450 °C for 250 hours. The alloy was subjected to density, differential scanning calorimetry (DSC), dilatometry, optical microscopy, electron probe micro-analysis (EPMA), X-ray diffraction (XRD) and hardness measurements. Optical microscopy of the alloy in the as-cast condition (shown in Fig. 1) revealed a highly inhomogeneous structure with Ga-rich cores surrounded by regions depleted in Ga. Following the heat treatment, the microstructure was seen to undergo significant alteration to its appearance. Optical microscopy of the alloy following heat treatment (also shown in Fig. 1) revealed the microstructure to be composed of a more intimate two-phase mixture of α-Pu and α+δ Pu. These microstructural observations are mirrored in the EPMA maps (see Fig. 2) which showed Ga to have diffused from the Ga-rich cores seen in the as-cast alloy, resulting in a more homogeneous distribution seen in the heat-treated alloy.

The Ga content is insufficient to retain a wholly δ-Pu phase at ambient temperature. Instead, the alloy appears to be a mixture of α- and δ-Pu, a finding borne out by density, DSC and XRD observations. Good agreement has been observed between the α-Pu contents determined from density measurements, DSC and dilatometry; in all cases they were between 53 % and 63% for both the as-cast and heat-treated alloys. These measurements, together with the optical microscopy observations, which all point to the mixed α / δ nature of the alloy, are

supported by X-ray diffraction (see Fig. 3), which revealed the presence of both phases. The hardness of the heat-treated alloy was approximately 25% lower than that of unalloyed Pu.

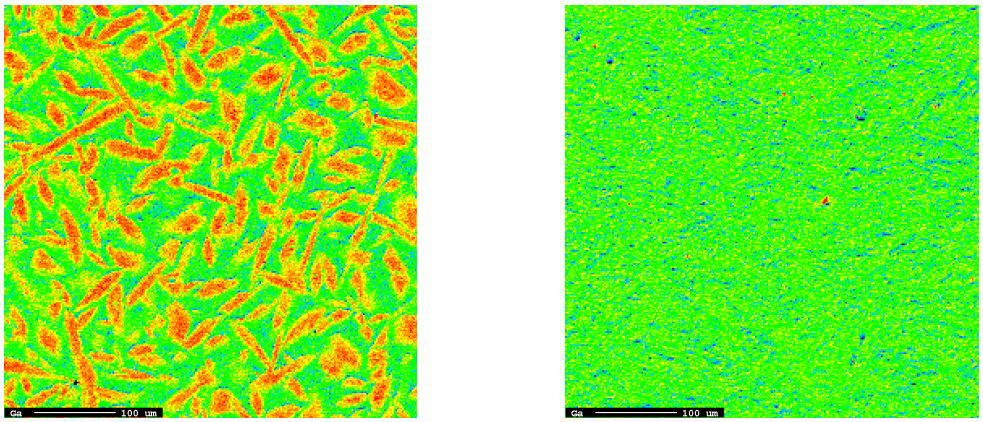

Fig. 2: Qualitative EPMA maps of the Pu-0.18 wt. % Ga alloy showing the Ga distribution in the as-cast (left) and heat-treated (right) conditions.

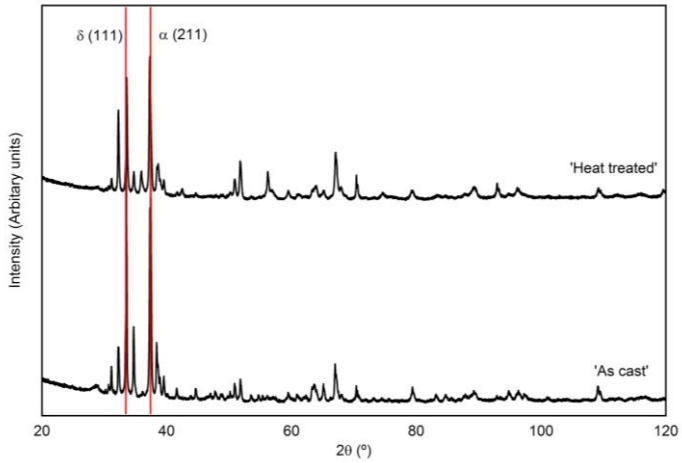

Fig. 3: X-ray diffraction patterns of Pu-0.18 wt. % Ga in both the as-cast and heat-treated conditions. For clarity, only the most prominent reflections for α-Pu and δ-Pu are shown.

References

[1] F.H. Ellinger, C.C. Land, V.O. Struebing, *J. Nucl. Mater*., 12 (1964), 226-236.
[2] D.C. Miller, J.S. White, *J. Nucl. Mater*., 17 (1965), 54-59.
[3] S.S. Hecker, E.G. Zukas, J.R. Morgan, R.A. Pereyra, *Solid-to-Solid Phase Transformations* (ed. H.L. Aaronson, D.E. Laughlin, R.F. Sekerka, C.M. Wayman), TMS, Warrendale, Pennsylvania (1982), pp. 1339-1343.
[4] E.G. Zukas, S.S. Hecker, J.R. Morgan, R.A. Pereyra, *Solid-to-Solid Phase Transformations* (ed. H.L. Aaronson, D.E. Laughlin, R.F. Sekerka, C.M. Wayman), TMS, Warrendale, Pennsylvania (1982), pp. 1333-1337.
[5] J.N. Mitchell, M. Stan, D.S. Schwartz, C.J. Boehlert, *Met. Mater. Trans. A*, 35 (2004), 2267-2278.
[6] K.J.M. Blobaum, C.R. Krenn, M.A. Wall, T.B. Massalski, A.J. Schwartz, *Acta Mater*., 54 (2006), 4001-4011.
[7] B.J.P. Oudot, K.J.M. Blobaum, M.A. Wall, A.J. Schwartz, *Mater. Res. Soc. Symp. Proc*., 893 (2006), 189-194.
[8] J.N. Mitchell, F.J. Freibert, D.S. Schwartz, M.E. Bange, *J. Nucl. Mater*., 385 (2009), 95-98.
[9] J.R. Jeffries, K.J.M. Blobaum, M.A. Wall, A.J. Schwartz, *Acta Mater*., 57 (2009), 1831-1842.
[10] J.R. Jeffries, K.J.M. Blobaum, M.A. Wall, A.J. Schwartz, *Phys. Rev. B*, 80 (2009), 094107.

Thermodynamic investigations of the (U, Am)O_2 solid solution

Octavian S. Vălu[1,2], Ondřej Beneš[1], Rudy J. M. Konings[1], Joseph Somers[1]

[1] *European Commission, Joint Research Centre, Institute for Transuranium Elements, Karlsruhe, 76125, Germany, e-mail: sorin.valu@ec.europa.eu*
[2] *Delft University of Technology, Faculty of Applied Sciences, Mekelweg 15, 2629 JB Delft, The Netherlands*

Studies on oxides of actinide elements such as thorium, uranium, plutonium and americium are of great interest in nuclear industry since most of these oxides are used or are planned to be used as nuclear fuels in various types of reactors [1]. The thermodynamic properties such as enthalpy and heat capacity of these materials are need in the form of mixed oxides for reactor design and safety calculations.

The most abundant transuranium elements found in the waste of nuclear power reactor fuels are Am and Np [2]. Because the two elements can be transformed by fast neutrons into shorter-lived fission products, recycling these elements in fast reactors would improve the efficiency and reduce the long-term hazard. The solid solution of the uranium and americium oxides is a possible chemical form for recycling americium. To understand the stability of the system with respect to the temperature the thermodynamic properties of mixed oxides needs to be investigated.

The main objective of this study is to investigate the heat capacity of the (U, Am)O_2 solid solution system. In this purpose we are using a Setaram multi detector high temperature calorimeter (MDHTC), operated in drop mode and the heat capacity is obtained by derivation of the measured enthalpy increments over temperature [3]. The enthalpy increments of (U_{1-y}, Am_y)O_2 solid solutions, with y = 0.1 and 0.2, were measured in the temperature range 400 – 1800 K and fitted using the least squares method as given in Figure 1.

The results of this study will be used to clarify if uranium and americium dioxides that form a continuous solid solution show an ideal behavior of the heat capacity (i.e. can be calculated by summing the proportional weights of their end-members) or if some excess contributions appear.

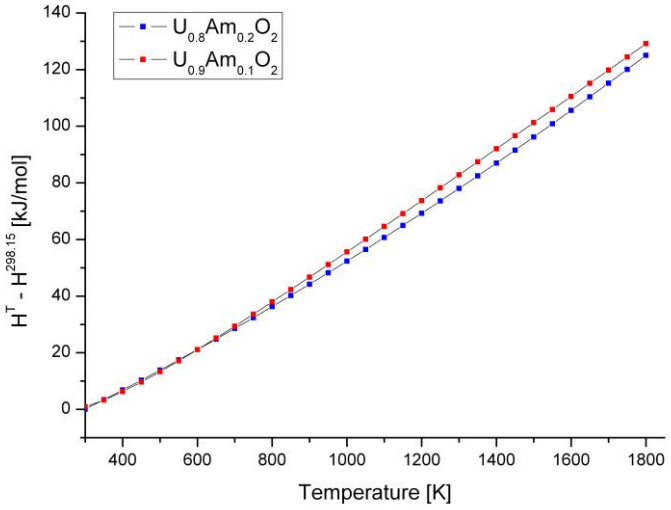

Fig. 1 The enthalpy fit according to the least squares method of the ($U_{0.8}Am_{0.2}$)O_2 and ($U_{0.9}Am_{0.1}$)O_2 intermediate compositions, measured in this study.

The results of the thus obtained C_P curves of $(U_{1-y}, Am_y)O_2$ solid solutions, in the temperature range 298 – 1800 K, show slight positive deviation from ideal behavior for $(U_{0.9}Am_{0.1})O_2$, while $(U_{0.8}Am_{0.2})O_2$ intermediate composition obey the Neumann-Kopp's molar additivity rule. The origin of this behavior will be discussed.

References

[1] C. Ganguly *IAEA-TECDOC* **107-127**, 352 (1985).
[2] W. Bartscher and C. Sari, *Journal of Nuclear Materials* **220-223**, 118 (1983).
[3] O. Beneš et al., *J. Chem. Thermodynamics* **651-655**, 49 (2011).

Using Autonomous Aerial Vehicles for Radiation Detection

Dr James MacFarlane

University of Bristol

Two years ago the nuclear industry was re-alerted to the severity of the repercussions of a large scale nuclear incident. Following a tsunami arising from a magnitude 9 earthquake, the Fukushima Daiichi nuclear power plant suffered a cooling failure which resulted in a runaway hydrogen explosion at the plant, and the wide spread radionuclide contamination of the surrounding areas. In the immediate disaster relief following the incident, there was a severe lack of information not only with the identity of radiation that was released from the plant, but also its radial extent and the regions that were affected. Indeed, emergency aid groups including the UN did not have sufficient data to accurately assign exclusion and evacuation zones surrounding the plant in the days and week following the incident. What is perhaps more concerning is that if a similar incident was to occur in the world, we would still not have an adequate method for reporting and translating the radiological information to make an informed response scenario. There is, therefore, a pressing and urgent need for low cost, rapidly deployable response units for the assessment of radiological hazards, following nuclear incidents. Moreover, the technology could be deployed to routinely monitor nuclear power plants, waste reprocessing units and mining operations. The ARM system was devised as a solution to this problem, and will allow for routine radiation monitoring in both the civil and military sectors as well as use as an emergency response device.

The Autonomous Radiological Monitoring (ARM) system is an autonomous low altitude aerial radiation detection device. Integrating lightweight gamma spectrometers with an unmanned aerial vehicle (UAV) it allows the operator to accurately assess a radiological hazard at a remote and safe distance, providing real-time information on the source isotopes, intensity and location of the radiation. The low weight, size and cost of the instrument combined with its capability for performing high spatial resolution aerial surveys makes it highly applicable and versatile for deployment across the nuclear industry.

Over a period of twelve months the instrument has been developed from a concept to a prototype with proven capability. Field demonstrations of the ARM prototype were performed at a Uranium mining site in the Banat District, southwest Romania. Data gathered by the ARM system was validated against traditional surveying methods. The prototype demonstrated the ability to produce accurate, high resolution radiation maps at a rate much greater rates than conventional techniques.

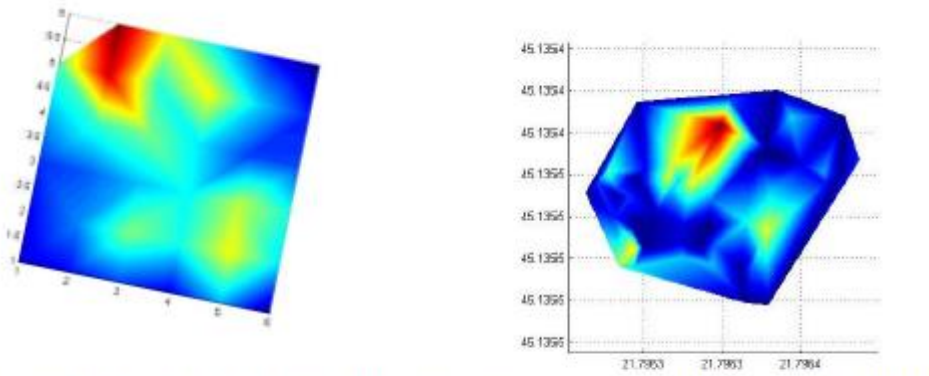

A comparison between recorded radiation intensity between a handheld survey (left) and an ARM system survey encompassing the same area (right).

Experimental Assessment Techniques for CANDU Pressure Tubes Degradation Mechanisms

Bogdan NEGULICI,[1] Valentin Paul GHEORGHE[2], Anca GHEORGHE[3]

[1] *Universitatea Politehnica Bucuresti, Splaiul Independentei nr.313, 060042 Bucuresti, Romania*
e-mail: negulicibogdan@yahoo.com
[2] *Universitatea Politehnica Bucuresti, Splaiul Independentei nr.313, 060042 Bucuresti, Romania*
e-mail: gheorghepaulvalentin@yahoo.com
[3] *Universitatea Politehnica Bucuresti, Splaiul Independentei nr.313, 060042 Bucuresti, Romania*

CANDU which stands for CANada Deuterium Uranium is a nuclear reactor designed by the Candu Energy Inc. the former AECL(Atomic Energy of Canada Limited). It uses natural uranium as fuel and heavy water as both cooling agent and moderator. This type of nuclear reactor is a special one because it doesn`t have a pressure vessel(like the majority of reactors)instead it has 380 fuel channels also known as CANDU Pressure Tubes(PT`s). The PT`s are critical components of this type of nuclear reactor and we have a special inspection program for our degradation mechanisms called fitness-for-service inspections. There are a series of possible degradation mechanisms:delayed hydride cracking(DHC), irradiation enhanced deformation(creep), corrosion, deuterium ingress and changes in material properties: reduction in ductility and fracture toughness. The inspections are visual, dimensional, ultrasonic, radiographic in order to discover this mechanisms. Pressure tube deformation has been managed such that it alone could not cause a safety or structural integrity concern for Cernavoda Nuclear Power Plant(NPP) fuel channels. Assessment methodology and prediction capacity enables Cernavoda NPP safe operation with certain conservatism. This paper presents the experimental assesment techniques for CANDU Pressure Tubes degradation mechanisms for the Cernavoda Nuclear Power Plant.

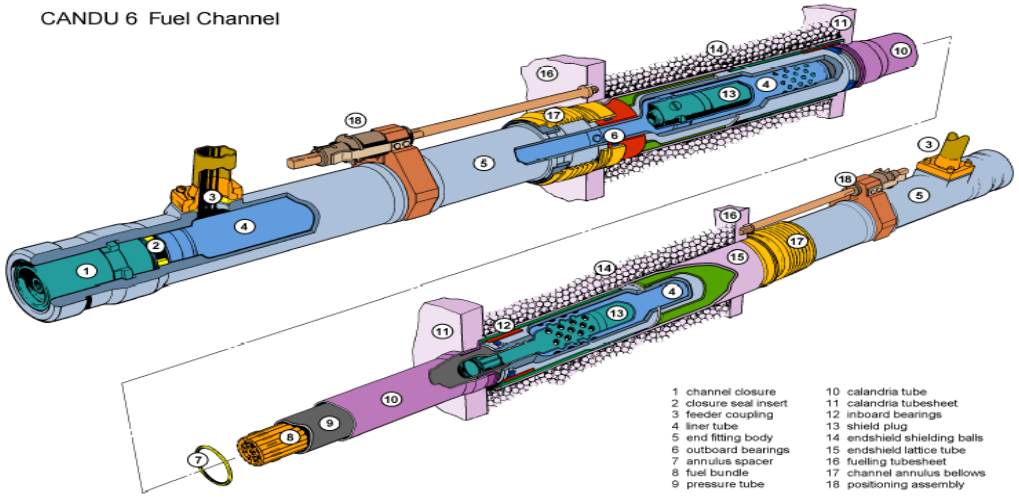

Fig.1 Cernavoda NPP Fuel Channel

References

[1] Canadian Standards Association(CSA) N285.4-09(2009)
[2]Yong-Zhi Wang „Management of Pressure Tube In-service Deformation in CANDU NPPs”(2011)

Interaction of U(VI) with Siderochelates by Affinity Capillary Electrophoresis

Vladimir Sladkov,[1] Michel Meyer,[2] Stéphane Brandès,[2] Jean-Claude Chambron,[2] Pawel Jewula[2]

[1] CNRS, Institut de Physique Nucléaire (IPN), UMR 8608, 91406 Orsay, France
Univ Paris-Sud, 91405 Orsay, France e-mail: sladkov@ipno.in2p3.fr
[2] Institut de Chimie Moléculaire de l'Université de Bourgogne (ICMUB), UMR 6302, 9 avenue A. Savary, 21078 Dijon Cedex, France

The bioavailability and mobility of uranium species can be affected by siderophores. Common in soil and marine environment, these strong iron chelators of microbial origin usually incorporate hydroxamate, catecholate, and/or carboxylate binding groups [1]. Endowed with hard oxygen donor atoms, these ligands exhibit high binding affinities towards other hard metal ions like the uranyl cation. To understand the impact of siderophores on the behavior of U(VI) species, it is important to study their coordination chemistry.

The interaction of uranyl with open-chain siderochelates (figure), such as dihydroxamic acids and desferrioxamine B, has been studied in aqueous perchloric acid solutions by affinity capillary electrophoresis (ACE) at pH values of 1.5, 2.0, and 2.5. The observed U(VI) mobility was found to decrease with increasing ligand concentration added to the background electrolyte solution (up to 0.05 M). Since metal-ion mobilities at different pH values reflect the chemical equilibria occurring in solution [2], the ACE data enabled us not only to confirm but also to complete the speciation model deduced from potentiometric titration experiments performed under 1:1 or 1:2 metal-over-ligand concentration ratios. The formation of two complexes, one being monoleptic and the second one dileptic, could be established for the three studied dihydroxamic acids and the trishydroxamic siderophore desferrioxamine B. Moreover, the values of the stability constants at 0.1 mol L^{-1} ionic strength ($NaClO_4$-$HClO_4$) were deduced by numerical data processing.

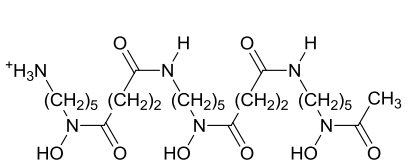

Desferrioxamine B

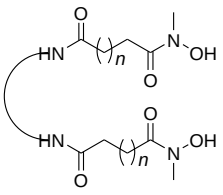

(*n* = 1 or 2)

Abiotic dihydroxamic acids

Figure. Open-chain siderochelates.

References

[1] H. Boukhalfa et al., *Inorganic Chemistry* **46**, 1018 (2007) and references therein.
[2] V. Sladkov, *Electrophoresis* **31**, 3482 (2010).

.

Time-Resolved Laser Induced Chemiluminescence Spectroscopy of Aqueous Actinide and Lanthanide Containing Solutions

I.N.Izosimov[1], N.G.Firsin[2], N.G.Gorshkov[2], V.A.Mikhalev[2], S.N.Nekhoroshkov[2]

[1]Joint Institute for Nuclear Research, 141980 Dubna, Russia,
e-mail: izig@mail.ru
[2] Khlopin Radium Institute, 194021 St. Petersburg, Russia

Of lanthanide or actinide properties analysis interest was to use advantages of luminescence procedure for detection of lanthanides and actinides having no self-luminescence, as an example, by initiation of luminescence of some agents through excitation of lanthanide or actinide element to be detected. An effort was made on initiation of luminol chemiluminescence through excitation of lanthanide and actinide ions with laser radiation [1,2]. Previously we showed a possibility of luminescence excitation in aqueous actinide-containing solutions, among them having no self-luminescence, by irradiation with nitrogen laser [1]. In this case chemiluminescence is caused by oxidation of luminescent agent (luminol) with hydroxyl radicals generated in deexcitation of excited actinide complexes. This chemiluminescence is not selective and proceeds at the background of luminol photoluminescence. The use of this type of chemiluminescence for detection of actinides is possible only in the case of selective excitation of chemiluminescence [2].

Chemiluminescence can be initiated selectively when using the absorption bands in visible range caused by transitions within the inner 5f electrons of actinide ions or 4f electrons of lanthanide ions. In this case chemiluminescence can be initiated only in absorption of two or more quanta of laser radiation since the energy of one light quantum in visible range is insufficient for chemiluminescence initiation. The possibility of selective initiation of luminol chemiluminescence in multi-quantum excitation of Sm(III), U(IV) and Pu(IV) in aqueous solutions with laser radiation was demonstrated in [3,4].

In this work the details of luminol chemiluminescence initiation through excitation of Sm(III), U(IV) and Pu(IV) ions with laser radiation are presented. Data on luminol chemiluminescence in solutions containing Sm(III), U(IV) and Pu(IV) are discussed. Chemiluminescence was induced by two-quanta excitation of lanthanide or actinide ions in the range of 4f or 5f electron transitions by the scheme *two steps-one color*, i.e. in irradiation of actinide-containing solution by one laser and by the scheme *two steps-two colors*, when a solution is irradiated by two lasers operating at different wavelengths. A multi-step scheme of chemiluminescence excitation makes this procedure not only highly sensitive but also highly selective procedure of detection of substances.

The experiments were performed on an installation involving a pulse nitrogen laser OBB 1010 with a pulse length of 1 ns and a pulse power of approximately 1.4 MW and two tunable dye lasers OBB 1011 and OBB 1012 with a pulse length of 1 ns and 800 ps respectively. The pulse power 300 kW was reached for dye lasers. A delay time for luminescence registration was 2 μs.

The spectra of chemiluminescence initiation as a result of excitation of Sm^{3+} ions with dye laser by using two steps-one color scheme (two photons absorbed during one laser pulse) is shown in fig.1. There is no complete similarity between the spectrum of chemiluminescence excitation and Sm^{3+} ions absorption spectrum. This experimental fact connected with the difference in the selection rule for single-quantum and multi-quantum absorption.

The spectrum of chemiluminescence excitation obtained in tuning of generation wavelength of the first laser (two steps-two colors scheme) is similar to the absorption spectrum of

uranium (Fig. 2). The presence of absorption band of U(IV) in the range of retuning of the second laser results in appearance of a peak of luminol chemiluminescence. This fact undeniably confirms the selective mechanism of chemiluminescence excitation.

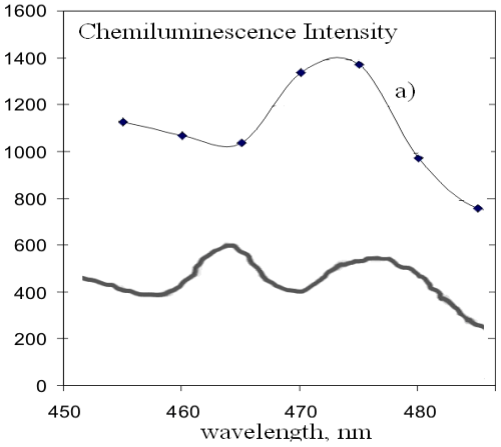

Fig.1. Two-steps one-color excitation of chemiluminescence. Excitation spectrum (a) of luminol chemiluminescence with dye laser in the range of absorption bands of Sm^{3+}. Chemiluminescence is detected at the wavelength of 460 nm. Absorption spectrum of Sm^{3+} is shown below.

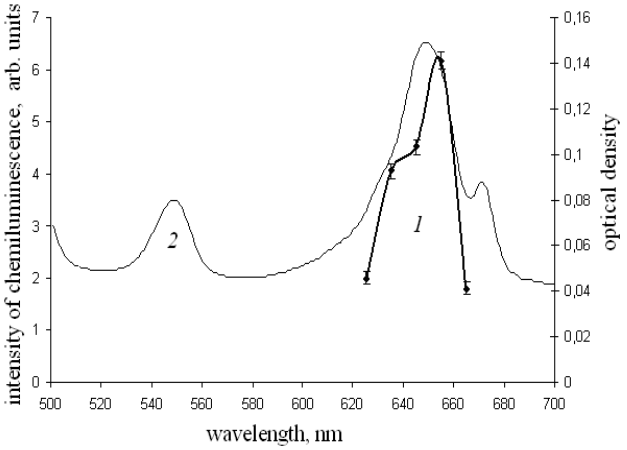

Fig.2. Two-steps two-colors excitation of chemiluminescence in solution luminol+U(IV)+HCl.
1.Chemiluminescence intensity dependence on the wavelength of laser radiation at the first excitation step. The wavelength of laser radiation at the second step was fixed at 500 nm.
2.Absorption spectrum of U(IV)+HCl solution.

Initiation of chemiluminescence as a result of excitation of Pu(IV) with two dye lasers was demonstrated for a solution containing CsF, luminol, and Pu(IV). A choice of solution composition was made based on an attempt to provide favorable conditions for observation of luminol chemiluminescence and to avoid formation of colloidal species of hydrolyzed Pu(IV). The spectrum of chemiluminescence excitation in both two steps-one color and two steps-two colors schemes correlated with absorption spectrum of Pu(IV). In both schemes we realized selective excitation of chemiluminescence and this selectivity is caused by the features of absorption spectra of Pu(IV) solutions.

Appropriate selectivity was reached in our experiments when chemiluminescence was initiated by transitions within 4f or 5f electron shell of lanthanide or actinide ions, which correspond to visible spectral range. Since the energy of one-quantum excitation in visible range is insufficient for initiation of luminol chemiluminescence, we selectively excited lanthanide or actinide ion by multi-quantum absorption of visible light. This fact allows using highly sensitive chemiluminescence procedure for selective detection of various valence lanthanide or actinide species in solutions based on individual features of their absorption spectra.

References

[1] I.N. Izosimov et al., *Proc. Int. Conf. Actinides 2005*, Manchester, UK, 2005, p.779.
[2] I.N. Izosimov, *Phys. Part. Nucl.*, **38**, 177 (2007).
[3] I.N. Izosimov et al., *Preprint of the Joint Institute for Nuclear Research, E6-2012-62*, Dubna, 2012. http://www1.jinr.ru/Preprints/Preprints_index.html
[4] N.G. Gorshkov et al., *Radiochemistry*, **6**, 525 (2012).

POSTERS

High-field magnetization and magnetoacoustics of a U_2Ni_2Sn single crystal

A.V. Andreev[1], S. Yasin[2], Y. Skourski[2], S. Zherlitsyn[2],
J. Wosnitza[2], S. Mašková[3], L. Havela[3]

[1] *Institute of Physics, Academy of Sciences, Na Slovance 2, 182 21 Prague, Czech Republic, e-mail: andreev@fzu.cz*
[2] *Dresden High Magnetic Field Laboratory, Helmholtz-Zentrum Dresden Rossendorf, D-01314 Dresden, Germany*
[3] *Department of Condensed Matter Physics, Faculty of Mathematics and Physics, Charles University, Ke Karlovu 5, 121 16 Prague, Czech Republic*

Uranium intermetallic compound U_2Ni_2Sn belongs to a wide group U_2T_2X (T is a late 3*d*-, 4d- or 5d- electron metal; X is a *p*-electron metal, Al Ga, In or Sn) with tetragonal crystal structure of the Mo_2FeB_2 type, an ordered ternary variant of binary U_3Si_2 type (space group P4/mbm) [1]. It is an antiferromagnet with T_N = 26 K. Three metamagnetic-like transitions were observed on free-to-rotate powders in high magnetic fields [2]. They were confirmed by magnetization study performed on a single crystal where the transitions at 30, 40 and 52 T (at 1.5 K) were observed in fields applied along the *c* axis [3].

In this work we present the results of study of influence of magnetic phase transitions, both the spontaneous ordering and the field-induced transitions, on the acoustic characteristics (sound velocity and sound attenuation) of a U_2Ni_2Sn single crystal.

The crystal was grown by the Czochralski method in tri-arc furnace. The magnetization curves were measured at 1.5-30 K in pulsed fields up to 60 T along the *c* axis (at 1.5 K, also along the *a* axis) using a non-destructive pulsed-field magnet with pulse duration of 25 ms. A detailed description of the setup is given elsewhere [4]. The absolute values of the magnetization were calibrated by steady-field measurements up to 14 T in a PPMS-14 magnetometer. For the ultrasound measurements, two piezoelectric film transducers were glued onto parallel polished facets perpendicular to the *a* axis of the crystal and the measurements were performed using a pulse-echo technique [5] in a He^4-flow cryostat in pulsed magnetic fields up to 60 T above 1.5 K. Sound propagation and sound polarization vectors were along to the *a* axis.

Temperature dependence of sound velocity in zero magnetic field exhibits an anomaly of $0.2*10^{-3}$ at 25 K which corresponds well to T_N. All three metamagnetic transitions are accompanied by pronounced anomalies in acoustic characteristics. Despite the transitions look similar in magnetization curves, acoustic anomalies are rather different (Fig. 1). The first transition at μH_{cr1} = 30 T (it is practically temperature-independent and seen up to T_N) produces a step down in sound velocity and is not seen at all in sound attenuation. The second (μH_{cr2} = 40 T, also temperature-independent) and third (μH_{cr3} = 52 T at 1.5 K and decreases with increasing temperature) transitions exhibit a deep minimum in sound velocity and an anomaly in attenuation.

Both effects are especially large at the second transition. Moreover, their temperature evolution is strongly non-monotonous (Fig. 1). Depth of the minimum in sound velocity $\Delta v/v$ starts from $2*10^{-3}$ at 1.5 K, passes through maximum value $22*10^{-3}$ at 12 K and then vanishes approaching T_N. Similarly, peak in sound attenuation is 4 dB/cm (1.5 K), 60 dB/cm (12 K) and 2 dB/cm at 20 K. Enhanced attenuation at H_{cr2} indicates that the 1st order transition (which has phase separation but not critical fluctuations) changes at elevated temperatures into 2nd order with diverging critical fluctuations.

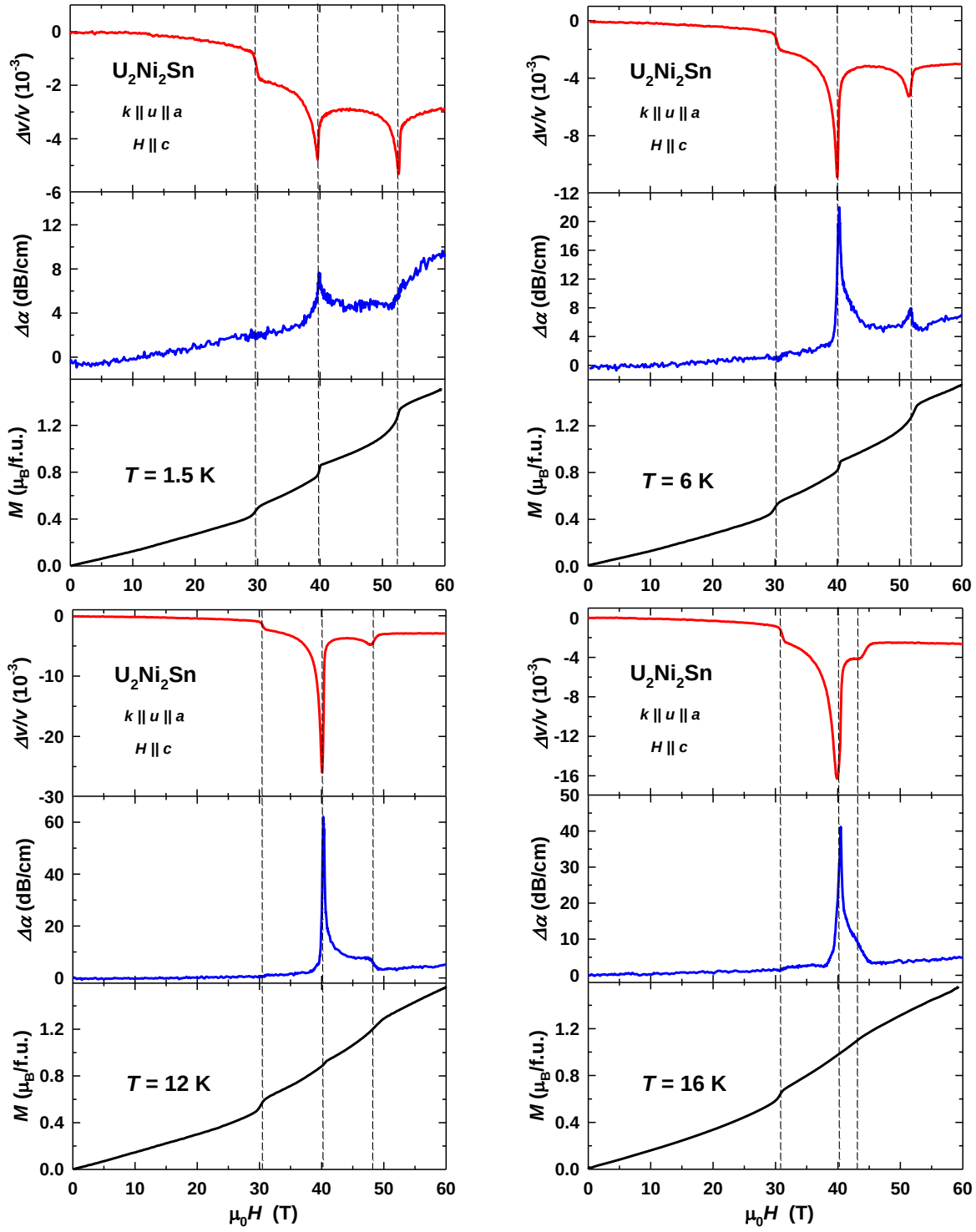

Fig. 1. Field dependences of magnetization M, change of sound velocity $\Delta v/v$ and change of sound attenuation $\Delta\alpha$ at 1.5 K, 6 K, 12 K and 16 K. Dashed lines indicate critical fields of metamagnetic transitions. Note different vertical scale for acoustic characteristics at different plots.

References

[1] V. Sechovský and L. Havela, in *Handbook of Magnetic Materials*, edited by K.H.J. Buschow (North Holland, Amsterdam, 1998), Vol. 11, p. 1 and references therein.
[2] K. Kindo, T. Fukushima, T. Kumada et al., J. Magn. Magn. Mater. 140-144 (1995) 1369.
[3] S. Mašková, L. Havela, A. V. Andreev et al., Proc. JdA-2011, Stara Lesna, Slovakia, 1O7.
[4] Y. Skourski, M.D. Kuzmin, K.P. Skokov et al. Phys. Rev. B 83 (2011) 214420.
[5] B. Wolf, B. Lüthi, S. Schmidt et al., Physica B 294-295 (2001) 612.

Effect of Rare Earths Addition on Al-Si Hypoeutectic Alloys: Mechanical and Corrosion Behaviour, Thermal Analysis Results

Anna Maria Cardinale[1], Daniele Macciò[1], G. Luciano [2], Pierluigi Traverso[2]

[1] *Dipartimento di Chimica e Chimica Industriale, Università di Genova, Via Dodecaneso 31, 16146 Genova, Italy*
cardinal@chimica.unige.it
[2] *C.N.R.-I.S.MAR. – U.O.S. di Genova, Via de Marini 6-Torre di Francia,16149 Genova,Italy*

Aluminium casting alloys containing silicon show great potential for industrial applications for their excellent castability, low density and good mechanical properties [1,2].
The Al-Si is a simple eutectic system with the eutectic composition at 12.6 mass % Si [3]. At room temperature, hypoeutectic alloys consist of a soft and ductile primary aluminum phase and a hard and brittle eutectic mixture in which the eutectic silicon crystallizes in an acicular or lamellar morphology.
In order to improve their technological properties alloying elements, such as copper, magnesium, manganese, zinc, iron and rare earth metals (mischmetal) are usually added to these alloys. Alloying elements can form fine precipitates, refine grain size and modify silicon phase morphology, increasing both fatigue and wear resistance.
As far as the corrosion behaviour is concerned, the lanthanides, for their chemical characteristics and chemical-physical properties, are considered as strong candidates in the research for new corrosion inhibitors. These elements have often been used in contact with Al-based materials in order to promote, in aqueous solution, the formation of a surface passivation layer composed by their insoluble oxides and hydroxides, as an alternative method to the chromating process.
Aim of this work is the investigation of the effect, on the properties described above, of the different rare earth metals additions to hypoeutectic Al-Si alloys; we will try also to assess whether the corrosion behavior improvement occurs even if the lanthanides are directly alloyed with aluminum and silicon.
Furthermore the addition of alloying elements to a cast Al-Si alloy modifies its microstructure inducing a lowering of the eutectic temperature. This lowering has been proposed as a method to control the eutectic modification level in the alloy microstructure by means of thermal analysis measurements [4].
Alloys were analyzed by means of differential thermal analysis (DTA), scanning electron microscopy (SEM) and electron probe microanalysis based on energy dispersive X-ray spectroscopy (EDXS). Vickers hardness was measured on alloy slices of appropriate shape.
As for the corrosion measurements, were carried out by means of potentiodynamic polarization curves, using as corrosive environment a solution of NaCl 3.5% (w/w) in unstirred medium, under the following experimental conditions: T = 25° C, P =1 atm, immersion time of 2 hours by using an electrochemical cell with three electrodes.

References

[1] Slattery B.E., Perry T., Edrisy A., *Mat. Sci. and Eng.* A **512**, 76 (2009).
[2]Ye H. J. *Mat. Eng. and Performance* **12**, 288 (2003).
[3] Massalski T.B., Okamoto H., Subramanian P.R., Kacprzak L. *"Binary Alloy Phase Diagrams,"* ASM International, Materials Park, OH, 1990.
[4] Heusler L., Schneider W. *J. Light Metals* 2, 17 (2002).

Experimental Assessment Techniques for CANDU Steam Generators Degradation Mechanisms

Anca Gheorghe,[1] Roxana-Georgiana Manea[2], Bogdan Negulici[3]

[1] *Universitatea Politehnica Bucuresti, Splaiul Independentei nr.313, 060042 Bucuresti, Romania*
e-mail: gheorghe.anca86@yahoo.com
[2] *Universitatea Politehnica Bucuresti, Splaiul Independentei nr.313, 060042 Bucuresti, Romania*
e-mail: roxana_georgiana_87_89@yahoo.com
[3] *Universitatea Politehnica Bucuresti, Splaiul Independentei nr.313, 060042 Bucuresti, Romania*

The Steam Generators are critical components of a CANDU(CANada Deuterium Uranium) Nuclear Power Plant. These components are part of the primary pressure boundary and are subjected to several degradation mechanisms which must be prevented or controlled otherwise they could lead to radioactive emissions. For preventing or controlling these degradation mechanisms we have several type of inspections: specific and random inspections, inaugural and periodic inspections. The areas that need focus are: Piping, Joints, Nozzle welds, Vessel welds . The inspections are visual, dimensional, ultrasonic, radiographic in order to discover the possible degradation mechanisms: corrosion, erosion, wear, leakage, defects, fractures. The limited knowledge regarding the causes of the degradation may lead to susceptible areas that are not inspected. The scope and frequency of these inspections are determined based on the results of a fitness for service assessment and taking into account the relative susceptibility of Steam Generators to each specific degradation mechanism. This paper presents the experimental assesment techniques for CANDU Steam Generators degradation mechanisms for the Cernavoda Nuclear Power Plant.

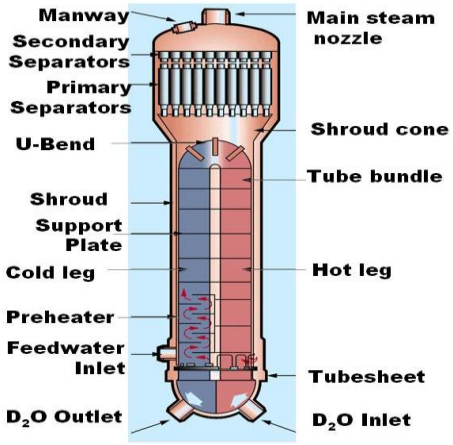

Fig.1 Cernavoda NPP Steam Generator

References

[1] Canadian Standards Association(CSA) N285.4-09(2009).

.

Reentrant quantum criticality in $Yb_2Pd_2(In,Sn)$ and Yb_2Pd_2Sn under pressure

M. Giovannini,[1] E. Bauer[2], H. Michor[2], T. Muramatsu[3], K. Shimizu[3], A. Amato[4]

[1] *CNR-SPIN and Dipartimento di Chimica e Chimica Industriale, Università di Genova, I-16146, e-mail: giovam@chimica.unige.it*
[2] *Institute of Solid State Physics, Vienna University of Technology, A-1040 Austria*

[3] *Kyokugen, Osaka University, Toyonaka, Osaka 560-8531, Japan*

[4] *Laboratory for Muon-Spin Spectroscopy, PSI, CH-5332 Villigen Switzerland*

In many rare-earth intermetallic compounds, in particular in those with Ce and Yb, the strength of the conduction-electron f-electron exchange interaction (J) can be tuned by composition, pressure or magnetic field, giving rise to either dominant Kondo or RKKY interactions. This offers the possibility to induce a zero-temperature quantum phase transition (QPT) between magnetic and non-magnetic ground states. In proximity to a QPT, non-Fermi liquid (NFL) behavior manifests itself as a strong deviation of thermodynamic and transport properties from Fermi liquid (FL) predictions.
Here we report the first example of a Yb-based heavy fermion, namely Yb_2Pd_2Sn, which is driven by pressure through two consecutive magnetic instabilities. The system evolves first from a nonmagnetic to an antiferromagnetic state and then back to a nonmagnetic one. The two instabilities emerge in a non-Fermi liquid environment at the origins of a dome-like single magnetic phase at pressures $p_{c1} \sim 1$ GPa and $p_{c2} \sim 4$ GPa [1]. This is shown by the inflection points of resistivity measurements taken at various pressures. In order to check magnetic order on a microscopic scale, muon spin rotation (μSR) measurements have been performed and these measurements corroborate the magnetic dome.

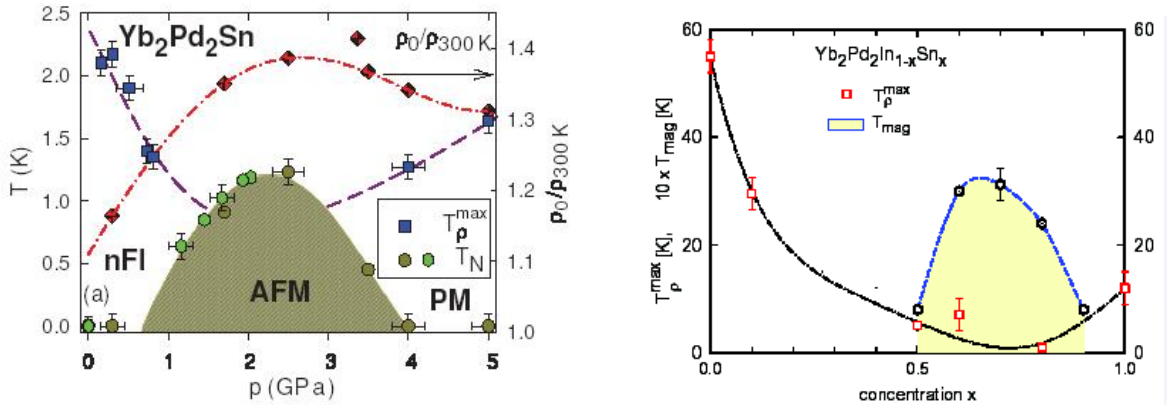

Fig. 1 Magnetic dome in the phase diagram for Yb_2Pd_2Sn:
(left) temperature vs. pressure (right) temperature vs. Sn/In doping

At ambient pressure Yb_2Pd_2Sn behaves as a Kondo lattice with no magnetic order down to 50 mK and non Fermi liquid behaviour as evidenced by specific heat and resistivity measurements. Magnetic order is triggered in the compound either applying pressure than by In/Sn substitution in a narrow concentration range.

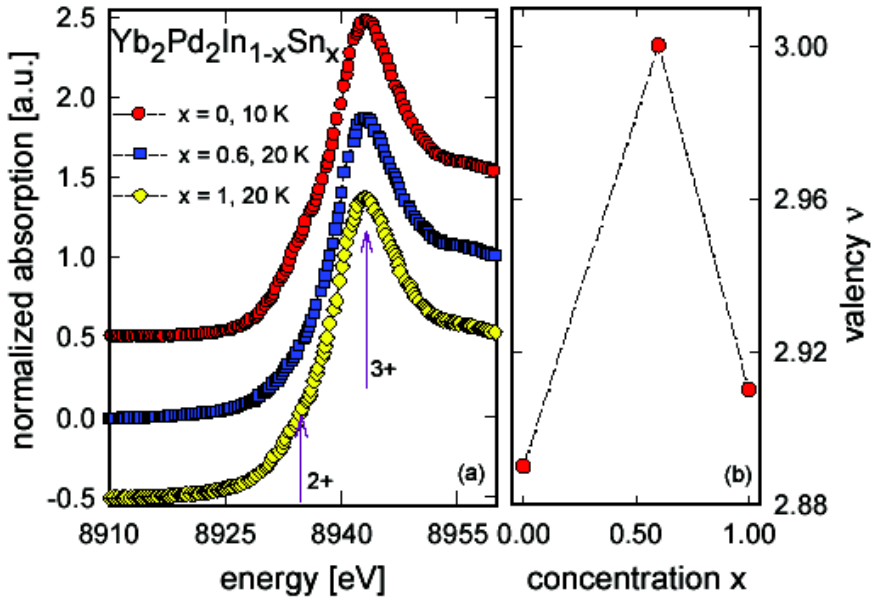

Fig. 2 L_{III} absorption edge spectra of $Yb_2Pd_2(In,Sn)$

In fact in a previous study [2] we demonstrated the occurrence of long range magnetic order in a dome-like phase space for a narrow concentration range of Sn-rich samples in $Yb_2Pd_2In_{1-x}Sn_x$. Ordered moments of the order of 1 μB are attained and the transition temperature reveals values above 3 K, although both Yb_2Pd_2In and Yb_2Pd_2Sn exhibit paramagnetic ground states. Results deduced from L_{III} absorption edge spectra carried out on different compositions (see Fig. 2) indicate a slight variation of the valency of the Yb ions from a value of 2.9 for the border compounds to a valency of 3 for at x=0.6. This variation triggers the magnetic order in a narrow concentration region, while both border compounds remain non-magnetic. In fact it is well known that Yb systems exhibiting valencies of about 2.9 or smaller do not show long range magnetic order.

References

[1] T. Muramatsu et al. *Phys. Rev. B* **83**, 180404R (2011).
[2] E. Bauer et al. *J. Phys.: Condens. Matter* **17** **S999-S1009** (2005).

Altering the hydriding behaviour of uranium metal by induced oxide penetration around carbonitride inclusions

N.J. Harker,[1] T. B Scott[1], C. P. Jones[1], J. R. Petherbridge[2] & J. Glascott[2]

[1] *University of Bristol, Interface Analysis Centre, BS2 8BS, UK, e-mail: n.j.harker@bristol.ac.uk*
[2] *AWE, Aldermaston, Reading, UK*

Secondary Ion Mass Spectrometry (SIMS) and Focused Ion Beam (FIB) milling were used to examine the surfaces of uranium samples, both before and after limited hydride formation to identify surface features that could provide sites for preferential hydrogen attack. Two sets of cast uranium samples containing 600ppm carbon in the form of carbo-nitride inclusions were examined; one set was prepared by mechanically polishing to a fine grade and the other received a subsequent electropolishing step. SIMS analysis showed that the additional electropolishing resulted in oxide development along the inclusion metal interface that was not present after only mechanical polishing. These samples then underwent hydrogen exposure for a limited period under conditions expected to result in hydride formation. For uranium prepared by only mechanical polishing, the hydride growths were observed to occur in significant numbers and almost exclusively around exposed inclusions. Conversely, preparation involving electropolishing resulted in extremely limited numbers of hydride growth sites not obviously associated with inclusions. These differences in hydride formation behaviour are attributed to the presence of oxide formed along the inclusion-metal interface resulting from electropolishing, and highlight how the observed hydride-forming behaviours exhibited by uranium can be significantly altered by the method of surface preparation.

3D ion mapping of nitro-carbide impurities in uranium metal using Magnetic Sector Secondary Ion Mass Spectrometry (MS-SIMS)

N.J. Harker,[1] T. B Scott[1], G. C. Allen[1], J. R. Petherbridge[2] & J. Glascott[2]

[1] *University of Bristol, Interface Analysis Centre, BS2 8BS, UK, e-mail: n.j.harker@bristol.ac.uk*
[2] *AWE, Aldermaston, Reading, UK*

Carbon and nitrogen have extremely limited solubility in α-uranium (<0.001 wt%). As a result, these impurities are found separate to the bulk metal as uranium nitro-carbide phase inclusions. These take the form of <10 micron euhedral bodies and are dispersed throughout the material. Where they appear at the surface, these features have been seen to exhibit distinct concentric banding and so have been imaged using Secondary Ion Mass Spectrometry ion mapping to determine their chemical speciation.

.

Using EBSD to look for deformation in uranium metal surrounding carbide inclusions

N.J. Harker,[1] T. B Scott[1] & J. R. Petherbridge[2]

[1] *University of Bristol, Interface Analysis Centre, BS2 8BS, UK, e-mail: n.j.harker@bristol.ac.uk*
[2] *AWE, Aldermaston, Reading, UK*

Contaminant inclusions, namely uranium carbo-nitrides, are a common feature in uranium metal. Where these bodies are exposed at the metal surface, they directly disrupt the ubiquitous oxide layer that naturally forms on uranium. This oxide layer provides a barrier preventing direct contact between the metal and the atmosphere that surrounds it. If uranium becomes exposed to hydrogen gas at conditions suitable for hydride (UH_3) formation, the perimeter of these inclusions, i.e. the carbide-metal interface, has been shown to provide favoured sites for the nucleation of UH_3 [1-3].

Due to the disparity between the thermal expansion coefficients for uranium and uranium carbide, it has been proposed that the metal surrounding these bodies possesses a greater level of residual stress relative to the bulk likely due to cooling after casting of the metal or from any subsequent annealing procedure. This implication has also lead to the suggestion that localised stress fields caused by these inclusions may increase the susceptibility of the metal in this region to hydrogen attack [4, 5]. Electron backscatter diffraction (EBSD) has been used to look for localised misorientation within the uranium crystal lattice at these sites as an indicator of residual stress. This data has also been trialled with 'cross correlation' EBSD, a processing technique that has the capacity to provide direct stress and strain measurements from the EBSD patterns recorded from a crystal lattice.

References

[1] R. Arkush et al., *Journal of Alloys and Compounds*, **197-205**, 244 (1996).
[2] L.W. Owen, R.A. Scudamor, *Corrosion Science*, **461,** 6 (1966).
[3] D. Moreno et al., *Journal of Nuclear Materials*, **181-186,** 230 (1996).
[4] A. Venkert et al., *Journal of Nuclear Materials*, **254-256,** 231 (1996).
[5] R.J.J. Hanrahan et al., *Conference: Materials Research Society, San Francisco, CA (United States)*, Nov 1998

Rare-earth electrospun carbides – model for submicron and nanostructured uranium carbides

M.S. Henriques[1], A. Cruz[1], M. Kratochvílová[2], J. Marçalo[1], L. Havela[2], T. Stora[3], A.P. Gonçalves[1]

[1]*IST/ITN, Technical University of Lisbon, CFMC-UL, 2686-953-Sacavém, Portugal, e-mail: mish@ctn.ist.utl.pt*
[2]*Dept. Condensed Matter Physics, Faculty of Mathematics and Physics, Charles University, 121 16 Prague, The Czech Republic*
[3]*CERN- European Organization for Nuclear Research, CH-1211 Genève 23, Switzerland*

Radioactive ion beams at ISOLDE, the CERN Isotope Separator On-Line Device, are produced when a pulsed proton beam of 1.4 GeV hits a target. The target material undergoes fragmentation, fission and spallation, yielding a wide variety of isotopes that must at first diffuse from the interior of the target to the surface and evaporate from it. Minimum delay times for the diffusion can be achieved for shorter diffusion lengths in highly-permeable, low-density, open-structure targets and by operating at high temperatures to minimize the releasing time of the isotopes of interest [1].

Uranium carbide based materials meet the target requirements for an efficient isotope release, and ISOLDE operation has been mostly based on UC_x targets for the last decades. Recent investigations have proven that submicron and nanostructured porous materials could significantly improve the release and yields of exotic isotopes [2].

The goal of this work is to produce submicron and nanostructured carbides of U to be tested at ISOLDE. To achieve this, an exploratory work is being carried out with lanthanide (Ln) elements via electrospinning, a suitable technique to prepare fine inorganic nanofiber precursors of ceramic materials [3].

Lanthanide acetylacetonates Ln(*acac*)$_3$ were synthesized for Ln = Eu, Er and Yb and mixed with cellulose acetate [3]. These solutions were electrospun at positive voltages between 15 and 27 kV, a working distance of 10 cm, and flow rates of 1–5 ml/h. The dried electrospun precursors were subsequently heat-treated in a furnace at 700 or 800 °C for 2 h in a flowing argon atmosphere.

Scanning electron microscopy (SEM) images of the electrospun precursors show that, for the same ratio Ln/C = 4, the spinnability of the solutions is different for each element. For Er, micrometric fibers are well formed, while for Eu the fibers are nanometric and exhibit many and large beads (Fig. 1a and b). In the case of the Yb, no fibers were formed.

The heat treatment of the electrospun precursors lead to the densification of the material and to the formation of highly porous samples. SEM micrographs showed that the porosity is open and that the distribution of pores sizes is very large (Fig. 1c and d). Furthermore, X-ray diffraction of these samples clearly indicates the formation of LnC_2 for all the studied samples at both temperatures. The estimated average crystallite sizes were 13, 4, and 3 nm for ErC_2, EuC_2 and YbC_2, respectively, without any significant change between the two temperatures. Crystallinity can be improved by heat treating the as-spun materials at higher temperatures. The cell volume decreases in accordance with the trend of the covalent radius of the lanthanide.

All these results point to the possibility of shaping uranium carbide or mixed carbides through electrospun precursors, which can be used as targets at ISOLDE and further efforts are ongoing into this direction.

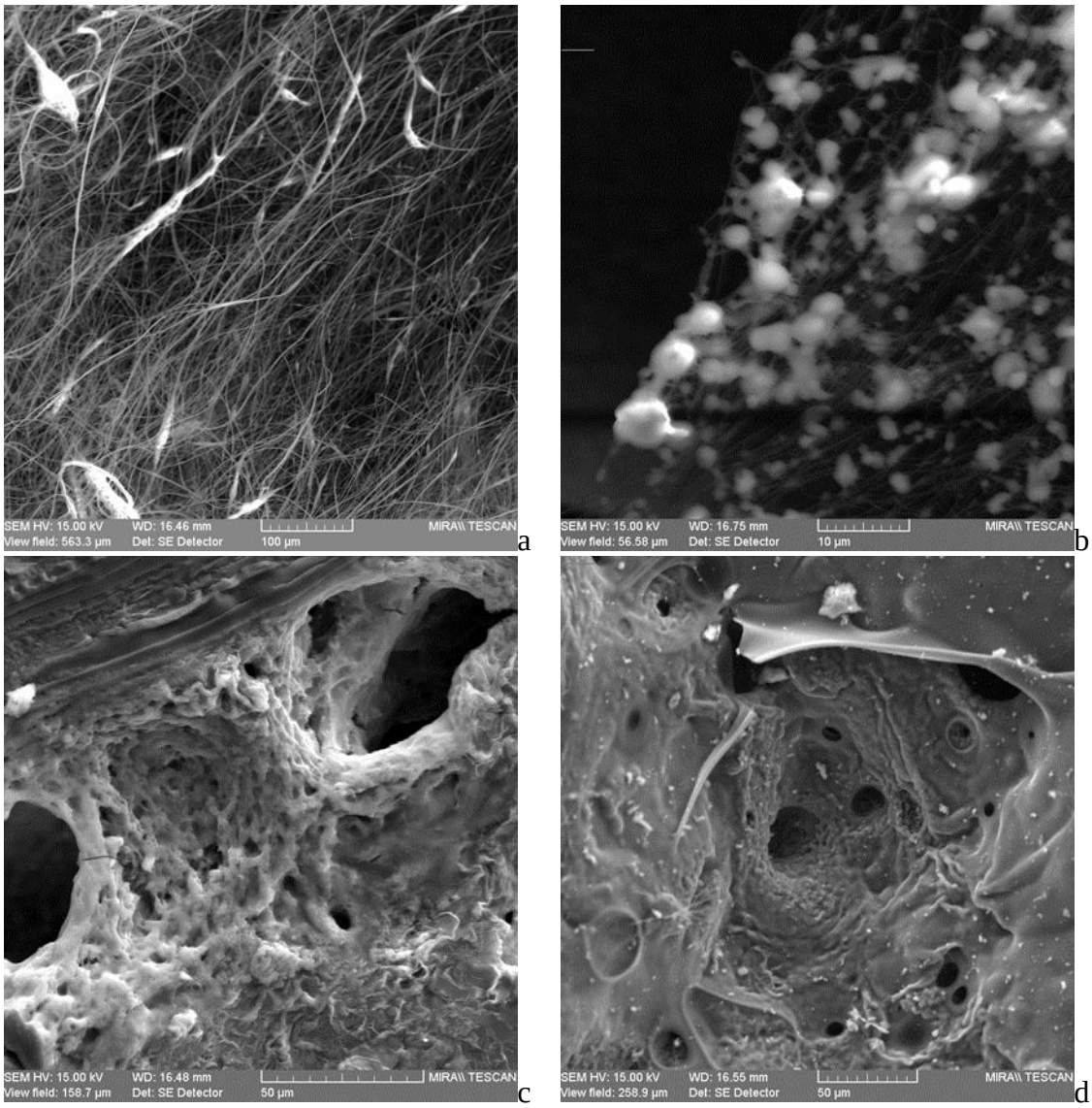

Fig. 1 – SEM images of the as-spun fibers of Er (a) and Eu (b) and of the heat treated samples of Er (c) and Eu (d) at 800ºC. Micrometric fibers were produced for the Er precursor, while for Eu beaded nanofibers were formed. The heat treatment of the precursors leads to a highly porous carbide structure.

Acknowledgments
This work was partially supported by FCT, Portugal, under the contract CERN/FP/123588/201 and the grant SFRH/BD/66161/2009 (M.S. Henriques).

References
[1] http://isolde.web.cern.ch/ISOLDE/
[2] S. Fernandes, PhD Thesis, CERN/EPFL (2010).
[3] Y.S. Nam et al., *Thin Solid Films* **517**, 6531 (2009).

Magnetic Studies on CoU_2O_6 and NiU_2O_6 by Magnetic Susceptibility, Specific Heat and Neutron Diffraction Measurements

Yukio Hinatsu[1], Yoshihiro Doi[1], Akio Nakamura[2]

[1]*Division of Chemistry, Hokkaido University, Sapporo 060-0810, Japan*
e-mail: hinatsu@sci.hokudai.ac.jp
[2]*Japan Atomic Energy Agency (JAEA), Tokai-mura, Ibaraki 319-1195, Japan*

Ternary uranium transition metal oxides CoU_2O_6 and NiU_2O_6 were prepared and their magnetic properties were investigated [1].

Crystal structures

X-ray and neutron diffraction measurements show that both compounds crystallize in the hexagonal Na_2SiF_6 structure (space group: *P*321), in which both cobalt (nickel) and uranium ions are in the distorted octahedral crystal field by six oxygen ions. Figure 1 shows the crystal structure of CoU_2O_6.

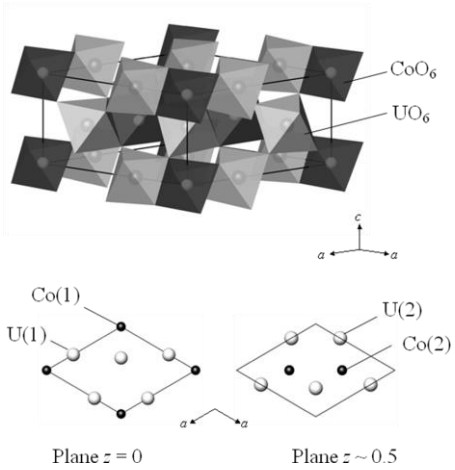

Fig. 1. The crystal structure of CoU_2O_6.

Magnetic properties

Figure 2 shows the temperature dependence of the reciprocal magnetic susceptibilities for CoU_2O_6 and NiU_2O_6. The antiferromagnetic transitions are observed at 32.5 and 35.3 K, respectively. The Curie-Weiss law fits to the magnetic susceptibilities in the temperature region between 150 and 400 K. The analysis of the magnetic susceptibility data indicates that the ionic models $Co^{2+}U^{5+}{}_2O^{2-}{}_6$ and $Ni^{2+}U^{5+}{}_2O^{2-}{}_6$ are valid.

Figure 3 shows the variation of the specific heat (*C*p) as a function of temperature in the temperature range between 1.8 and 300 K. One clear λ-type specific heat anomaly was observed for each compound, which indicates that both the magnetic moments of Co (Ni) and U order at the same temperature. This anomaly corresponds to the antiferromagnetic transition found in the magnetic susceptibility.

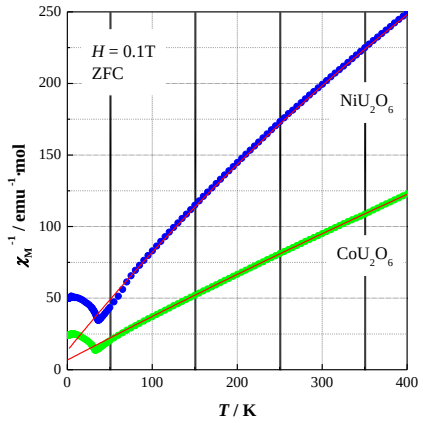

Fig. 2. Temperature dependence of the reciprocal magnetic susceptibility for MU_2O_6 (M = Co, Ni). The solid lines are the Curie-Weiss fitting.

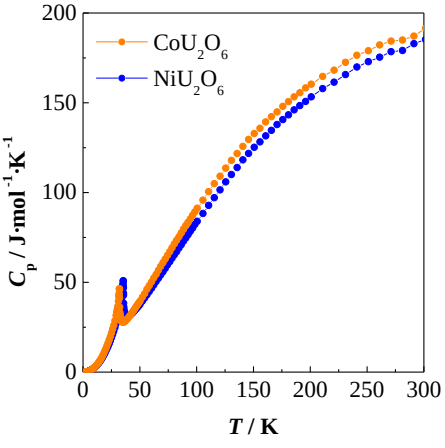

Fig. 3. Temperature dependence of the specific heat C_p for MU_2O_6 (M = Co, Ni).

IIn order to estimate the magnetic entropy change due to the magnetic ordering, we subtracted the lattice specific heat contribution from the total specific heat. It was estimated by using a polynomial function of the temperature f (T) = $aT^3 + bT^5 + cT^7$[2].The magnetic entropy changes due to the antiferromagnetic ordering for CoU_2O_6 and NiU_2O_6 are about 7.0 and 7.5 J/mol K, respectively. The results for the magnetic entropy change indicate that the degeneracy of the ground states for the M^{2+} ion and U^{5+} ion in MU_2O_6 should be both twofold.

Magnetic structure

Figure 4 shows the magnetic structure for CoU_2O_6 determined by neutron diffraction measurements at 10 K. It is a multi-sinusoidal structure with a propagation vector (0, 0, 1/6), in which the magnetic moments of the Co ions are parallel to a (1 1 0) direction and the magnetic moments of the U ions have a component of 0.46 μ_B along the (1 1 0) direction and a component of 0.25 μ_B along the (0 0 1) direction.

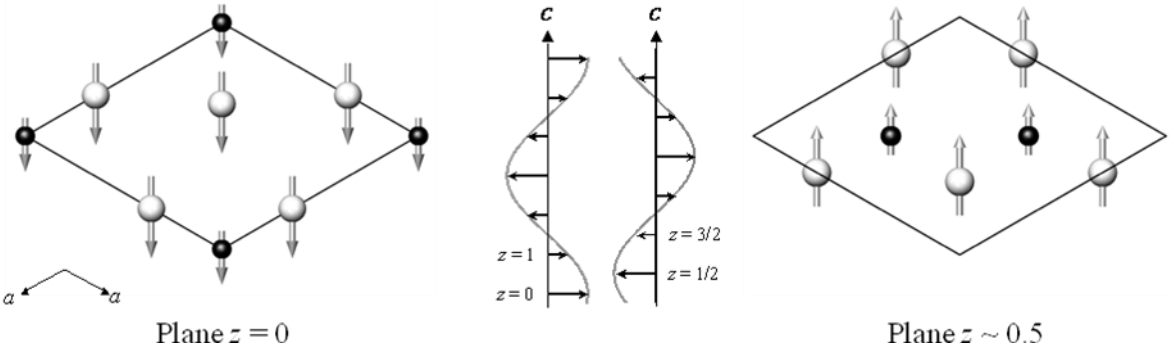

Fig. 4. The magnetic structure of CoU_2O_6.

References

[1] Y. Hinatsu, Y. Doi and A. Nakamura, *J. Nucl. Mater.*, **385**, 49 (2009).
[2] J. E. Gordon, R. A. Fisher, Y. X. Jia, N. E. Phillips, S. F. Reklis, D. A. Wright, A. Zettle, *Phys. Rev., Materials*, **B59**, 127 (1999).

Synthesis and Characterization of Nanostructured Cerium Nitride

Hayao Imamura, Masahiro Kawazoe, Yoshihisa Sakata

Graduate School of Science and Engineering, Yamaguchi University,
2-16-1 Tokiwadai, Ube 755-8611 Japan,
e-mail: hi-khm@yamaguchi-u.ac.jp

There has been a growing interest in fundamental investigations and technological applications of lanthanide and actinide elements and compounds. We have studied catalytic properties of these important and fascinating classes of elements [1-4]. It was found that nitrides showed an interesting catalysis [2-4]. In this study, attention has been directed to the synthesis of nanostructured cerium nitride (CeN) with high surface areas as an active catalyst.

By the use of the thermal decomposition of cerium amide to nitride, the synthesis of active and nanostructured cerium nitride was extensively studied with search for optimal conditions. In this method, the synthesis of the amide as an effective precursor of the nitride was similarly of importance and the amide used here was obtained by the following manners; one is reactive ball milling of cerium hydrides under 0.3 MPa ammonia pressure and the other one the ammoniation of cerium hydrides in an autoclave at 483 K. CeN was successfully prepared by the thermal decomposition of the cerium amides or amide-like compounds formed by the reaction of cerium dihydride or trihydride with ammonia. Active nanocrystalline CeN was obtained by the decomposition of cerium amide around 873 K. The thermal decomposition processes of cerium amide to nitride were studied by XRD and temperature-programmed desorption techniques.

References

[1] H. Imamura, in: *Handbook on the Physics and Chemistry of Rare Earths*, K. A. Gschneidner, Jr., L. Eyring (Eds.), Vol. 29, North-Holland, Amsterdam, 2000, pp. 45-74.
[2] H. Imamura, T. Nuruyu, T. Kawasaki, T. Teranishi, Y. Sakata, *Catal. Lett.* **96**, 185 (2004).
[3] H. Imamura, Y. Sakata, T. Nuruyu, and T. Imahashi, *J. Alloys Compd.*, **418**, 251 (2006).
[4] H. Imamura, T. Kuhara, M. Furutachi, T. Sakamoto, and Y. Sakata, *Chem. Lett.*, 744 (2002).

Structural deformation of metallic uranium surrounding hydride growth sites

Dr Christopher Jones,[1] Dr Tom Scott[1], Dr James Petherbridge[2], Dr Joseph Glascott[2]

[1] *Interface Analysis Centre, University of Bristol, BS2 8BS, England. e-mail: cj0810@bristol.ac.uk*
[2] *AWE, Reading, RG7 4PR, England*

Uranium is known to corrode when stored in environments containing gasses such as water, oxygen or hydrogen. This is particularly true in the case of hydrogen. Although the reactions responsible for forming uranium hydride are well defined the processes leading to the nucleation of hydride growth sites are not. Thus, the primary goal of the research was to provide a better understanding of the initial stages of hydrogen corrosion on uranium surfaces by identifying and investigating the key structural and chemical controls that determine the location of initial hydrogen attack. The following work investigated how vertical stress and related microstructures penetrate deeper into the body of the metal and was achieved using new focussed ion beam (FIB) surface preparation techniques for electron backscatter diffraction (EBSD) analysis. Figure 1 shows an example of a sectioned, evacuated, hydride site, as a combination EBSD inverse pole figure map and secondary electron image.

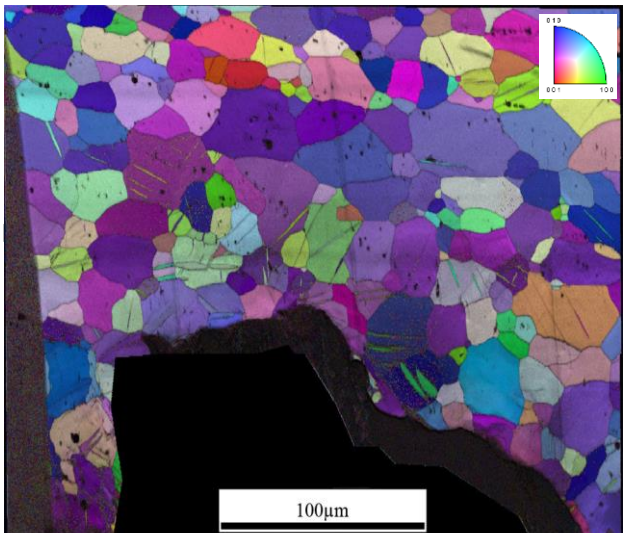

Fig 1. Electropolished section of a hydride pit on low carbon uranium. a) a secondary electron image of the surface where the contrast between grains is clearly seen. b) an EBSD map of the hydride pit overlaying crystal orientation (colour) with a secondary electron image (greyscale).

Chemical Heterogeneity in Uranium Ore deposits: A case study South-West England

Anya Keatley[1], Tom Scott[1]

[1]*Interface Analysis Centre, University of Bristol, 121 St.Michaels Hill, Bristol, BS2 8BS, United Kingdom e-mail: a.keatley@bristol.ac.uk*
[1]*Interface Analysis Centre, Bristol, BS2 8BS, United Kingdom*

Nuclear forensics is a growing field; starting in the early 1990's when the first seizures of illicit nuclear material were reported. For any such material an initial characterisation is performed prior to more detailed investigations relating to intended use, trafficking route and origin [1].

To determine material origin, the seized material is analysed for characteristic signatures or "fingerprints", in comparison to a database of representative samples of known origin [1]. Identifying the sample attributes that are specific to geographic origin has been worked on by a number of institutes, focusing generally on yellowcake [2,3,4]. However only a few studies have looked at unprocessed uranium ore [5,6], the precursor material.

The database contains only a small mass of each representative sample (several grams or tens of grams), which is supposed to adequately represent in some cases the fingerprint of an entire mining site or mining region. The database assumes complete homogeneity of the ore deposit in terms of mineralogy, elemental and isotopic composition. In reality the mineralogy of an ore deposit often varies laterally and with depth, with a primary lode often surrounded by secondary ore minerals. Certain parameters such as age, uranium concentration, lead and uranium isotope ratios are also likely to change [7,8]. This is because deposits may take millions of years to form and the uranium may subsequently be remobilized within the deposit to form new minerals and at the same time leaving daughter elements behind.

We have sought to test this aforementioned assumption of homogeneity by comparing and contrasting uranium ore extracted from different mines in the same region; South-West England.

The geology of South-West of England is dominated by a large granite batholith complex divided into a number of different intrusions, proven to differ in age, composition and texture [9, 10]. These granites have important associated mineralization; tin and copper with arsenic, tugsten molybdenum and fluorite are found lodes which strike primarily E-W and younger crosscourse lodes commonly containing cobalt, nickel and uranium are found which strike N-S [11]. Uranium ores have previously been mined in this area from the late nineteenth to the early twentieth century.

This study will extract samples from uranium deposits associated with these different granite intrusions. We will harvest multiple samples from different positions within each mineral lode (within the same mine) to determine in-mine variation of ore character in addition to regional variations related to differences in the source rocks.

A chemical fingerprint for each sample will be made by analysing for concentration of different elements, by looking at Pb:U, $^{207}Pb/^{208}Pb$, $^{206}Pb/^{208}Pb$, $^{18}O/^{16}O$, $^{87}Sr/^{86}Sr$ and $^{235}U:^{238}U$ isotope ratios.

References

[1] K.Mayer et al., *Journal of Alloys and Compounds* **444-445**, 50 (2007)
[2] E.Keegan et al., *Applied Geochemistry* **27**, 1600 (2012)
[3] Z.Varga et al., *Talanta* **80**, 1744 (2010)
[4] E.Keegan et al., *Applied Geochemistry* **23**, 777 (2008)

[5] J. Švedkauskaitė-LeGore et al., *Journal of Radioanalytical and Nuclear Chemistry* **278**, 201 (2008)
[6] S.Richter et al., *International Journal of Mass Spectrometry* **193**, 9 (1999)
[7] C.Bopp et al., *Geology* **37**, 611 (2009)
[8] Z.Varga et al., *Analytical chemistry* **81**, 8327 (2009)
[9] B.Chappell et al., *Rescource Geology* **56**, 203 (2006)
[10] M.Stone., *Proceedings of the Ussher Society*, 206 (1997)
[11] P.Simpson et al., *Philosophical Transactions of the Royal Society A: Mathematical, Physical and Engineering Sciences* **291**, 385 (1979)

Study of the U(Vl) Sorption on Layered Double Hydroxides under Different Conditions

S. A. Kulyukhin, E. P. Krasavina

Frumkin' Institute of Physical Chemistry and Electrochemistry, Russian Academy of Science, Leninskii prospekt, 31, 119071 Moscow, Russia, E-mail: kulyukhin@ipc.rssi.ru

The development of novel materials for localizing radionuclides from different media including liquid media is currently an acute issue. These materials can be various minerals (bentonite, clinoptilolite, and montmorilllonite), as well as layered double hydroxides - synthetic analogs of hydrotalcite, supramolecular dimeric systems, and compounds of the composition $[(M^{2+})_{1-x}\cdot(M^{3+})_x(OH)_2][(A^{n-})_{x/n}\cdot mH_2O]$, where M^{2+} and M^{3+} are cations in the 2+ and 3+ oxidation states, respectively, and A^{n-} is virtually any anion or anionic complex.

We studied the sorption of U(VI) on layered double hydroxides (LDH) of Mg, Al, and Nd, as well as on layered double oxides (LDO) of Mg and Al from aqueous solutions of different compositions. We found that the sorption of the carbonate complex $[UO_2(CO_3)_3]^{4-}$ by LDH-Mg-Al, which arose upon contact of LDO-Mg-Al with water, was poor. For $3.3\cdot10^{-3}$ mol/l solutions of $[UO_2(CO_3)_3]^{4-}$, K_d were not higher than 1.0 ml/g at V/m = 50 ml/g after 24-hour contact between the liquid and solid phases (τ). The sorption of U(VI) on LDH-Mg-Al-NO_3 from aqueous nitrate solutions was poor (K_d for U(VI) were not higher than 1.0 ml/g at τ = 24 hours and V/m = 50 ml/g). On the other hand, U(VI) effectively sorbed on LDH-Mg-Al and LDH-Mg-Nd, with CO_3^{2-} and OH^- being in the interlayer space, from 10^{-3} mol/l aqueous solutions of $UO_2(NO_3)_2$ (K_d for U(VI) were $>5\cdot10^3$ ml/g at τ = 15 min). Increasing the UO_2^{2+} concentration to 10^{-1} mol/l led to a significant decrease in K_d (to <25 ml/g) for U(VI), which, however, increased to ~150 ml/g, when τ was increased to 24 hours.

The K_d values for U(VI) on LDH-Mg-Al-EDTA were 100-120 ml/g at τ =15 min and V/m = 50 ml/g. Under analogous conditions, no sorption of U(VI) on LDH-Mg-Al-C_2O_4 from aqueous solutions occurred. The sorption of U(VI) on LDH -Mg-Nd-CO_3 and LDH-Mg-Al-CO_3 from aqueous solutions containing H_2EDTA^{2-}, $C_2O_4^{2-}$, and CO_3^{2-} strongly depended on the concentration of complex-forming agents in the solution. Thus, for 10^{-3} mol/l aqueous solutions of UO_2^{2+}, increasing $[C_2O_4^{2-}]$ from 10^{-3} to $5\cdot10^{-2}$ mol/l K_d for U(VI) decreased from $>5\cdot10^3$ ml/g to 70 ml/g for LDH-Mg-Al-CO_3 and from 170 ml/g to ~0 ml/g for LDH-Mg-Nd-CO_3. In the aqueous solution containing 10^{-3} - $5\cdot10^{-2}$ mol/l CO_3^{2-}, hardly any sorption of U(VI) on LDH-Mg-Nd-CO_3 took place (K_d were not higher than 16 ml/g at V/m = 50 ml/g). For LDH-Mg-Al-CO_3, the sorption of U(VI) abruptly decreased (K_d dropped from $>5\cdot10^3$ to ~0 ml/g at V/m = 50 ml/g).

We also studied the influence of Sr^{2+} ions on the sorption of U(VI) microquantities, as well as the influence of UO_2^{2+} ions on the sorption of ^{90}Sr and ^{90}Y microquantities from aqueous solutions on LDH-Mg-Nd-CO_3. In addition, we investigated the effects of Na^+, Ca^{2+}, Cl^-, and SO_4^{2-} ions, as well as of the pH of the initial solution on the sorption of U(VI) on LDH-Mg-Al-CO_3 from aqueous solutions of $UO_2(NO_3)_2$.

The obtained results allow us to conclude that natural minerals referring to hydrotalcites of the composition $Mg_nAl(OH)_6[(CO_3)_{1/2}\cdot mH_2O]$ can accumulate U(VI) by sorbing UO_2^{2+} from aqueous media, and LDH-Mg-Nd-CO_3 may find use for withdrawing ^{90}Sr and radionuclides of the trivalent *f*-elements, and also U(VI) from aqueous solutions of complex chemical compositions.

Method of plutonium preconcentration during sea water sampling

S. A. Kulyukhin[1], I. E. Veleshko[2], A. N. Veleshko[2]

[1] *Frumkin' Institute of Physical Chemistry and Electrochemistry, Russian Academy of Science, Leninskii prospekt, 31, 119071 Moscow, Russia, E-mail: kulyukhin@ipc.rssi.ru*
[2] *Russian National Scientific Center "Kurchatov' Institute", Kurchatov sq., 1, 123812 Moscow, Russia*

During the development of the method of Pu preconcentration, a quantitative assessment of the physicochemical state of Pu in sea water was carried out. It is known that depending on the solution pH, actinides and especially Pu occur in solutions in ion disperse, molecular, pseudocolloid, colloid, and coarsely dispersed forms of different particle sizes. Colloid particles in solutions can be identified using the ultrafiltration method, which separates ion disperse and colloid fractions by filtering solutions through ultrafilters with different pore diameters. Radioactive elements occurring in solutions in coarsely dispersed and pseudocolloid states are identified using centrifugation [1].

At first, we measured the quantity of Pu occurring in solutions in ionic and colloid forms. ^{239}Pu was added as mark to 100 ml of Barents Sea water sample. The sample was mixed, allowed to stand for 24 h, and then filtered. The filtrate was subjected to ultracentrifugation (18000 revo/min). The ^{239}Pu content was then measured in each fraction. The obtained data on the Pu distribution shows that about 38% of it is sorbed on suspended particles, and 20.9% is in the ionic form. The remaining Pu is either in the colloid state, or sorbed on other colloid particles to form pseudocolloids [2]. Therefore, the flocculation precipitation of colloids and suspended particles on freshly precipitated chitosan could be an effective method to concentrate plutonium.

The obtained results on the Pu and U coprecipitation on low-molecular chitosan (LMC) in salt solutions allowed us to consider the possibility of using LMC for Pu preconcentration in sea water with its simultaneous separation from U. Using LMC already forming a bulk precipitate at pH 6 excluded the possibility of its simultaneous coprecipitation with Ca^{2+} and Mg^{2+} occurring in sea water in microquantities (0.39 and 1.23 g/l, respectively) [3].

To develop the method, we studied the influence of the LMC content in the 0-1 g/l concentration range on the Pu and U coprecipitation degree in the Barents Sea water. The data on the kinetics of the Pu and U coprecipitation from the Barents Sea water show that the kinetic equilibrium on LMC was reached over 20-30 min for either element. Also it was found that coprecipitation degree for Pu was 92% at [LMC] = 0.2 g/l, and it increased insignificantly (95%) in the 0.2-0.7 g/l concentration range. Increasing the chitosan concentration further on had hardly any effect on the Pu coprecipitation efficiency. In contrast to Pu, the U coprecipitation degree increased monotonically over the entire LMC concentration range studied. Thus, coprecipitation degree for U was 50% at [LMC] = 0.2 g/l, whereas at [LMC] = 1.0 g/l, it increased to 70%; i.e., virtually 1.5-fold. Therefore, the investigations were carried out at [LMC] = 0.2 g/l, at which the difference in coprecipitation degree for U and Pu was the highest.

Based on the obtained results, we proposed a method of sea water analysis for Pu concentration. The method was tested in expeditions in the Kara and Barents seas. The water samples were taken at different sea levels. The sample volumes were 60 to 100 l. Two liters of an LMC solution ([LMC] = 10 g/l and pH 3) was added to the sample. The coprecipitation of Pu on LMC was carried out by adding an ammonium solution during vigorous mixing and varying pH to 6. The resultant chitosan precipitate obtained after settling (12 h) and decanting was filtered and dried at 95^{o}C in the air. The LMC precipitate containing Pu and U was burnt in a mixture of H_2O_2 and concentrated HNO_3 taken at a volume ratio of 1:5. The obtained

small mineral residue was dissolved in 20 ml of 7 M HNO_3 solution. The radiochemical separation of Pu and U was carried out using extraction with trioctylamine (TOA) followed by reducing re-extraction with a solution of hydrochloric-acid hydroxylamine. The dry solid after evaporation was dissolved in 5 ml of a 7 M HNO_3 solution. The obtained solution was used for making the target for alpha-spectrometry.

The experiments carried out using the proposed method showed that the chemical yield of Pu from the samples taken in the Stepovoi Bay of the Novaya Zemlya Archipelago was as high as 84% versus 43% obtained by the traditional methods using $Fe(OH)_3$ as a coprecipitator [4, 5]. The alpha-spectra of these samples show the presence of ^{238}Pu, ^{239}Pu, and ^{240}Pu isotopes.

Thus, the usage of chitosan for concentrating radionuclides during the ecological monitoring of natural waters showed wide prospects for its practical uses. One of the options could be the reprocessing of low-level salt waste.

The research was carried out using financial support by the Russian Fund for Fundamental Research (Grand N 11-03-00106).

References

[1] I.E. Starik *Osnovy Radiokhimii*, Nauka, Leningrad, 423 (1969).
[2] Yu.V. Kuznetsov, V.N. Schcebetkovskii, A.G. Trusov *Osnovy Ochistki Vody Ot Radioactivnykh Zagryaznenii*, Atomizdat, Moscow, 360 (1974).
[3] V.A. Avramenko, V.V. Zheleznov, E.V. Kaplun, T.A. Sokol'nitskaya, A.A. Yukhkam *Radiokhimiya (Russia)*, **43**, 381 (2001).
[4] T.A. Goryachenkova, V.V. Emel'yanov, I.E. Kazinskaya, K.V. Barsukov, O.V. Stepanets, B.F. Myasoedov *Radiokhimiya (Russia)*, **42**, 264 (2000).
[5] F.I. Pavlotskaya *Russian Z. Analyt. Khimii*, **52**, 126 (1997).

Optimization of mechanical systems with abnormal functioning through the example of a precipitation centrifugation of powder precipitates

M.A. Kuzin,[1] O.I. Dreganov [1]

[1] *JSC "State Scientific Center – Research Institute of Atomic Reactors", 433510 Dimitrovgrad-10, Russia, e-mail: adm@niiar.ru*

The vertical submersible centrifuges are widely used in the chemical processes to separate suspensions, remove precipitates from chemical reactors and filtration. However, these devices have some disadvantages in terms of reliability and reproducibility of data on the mass of precipitates removed from a chemical reactor as well as of the prime cost of the in situ tests. The remedial can be done using the mathematical and simulation modeling so as to optimize and assess the parameters of reliability, efficiency and performance of the centrifuges. The calculation experiments will thus decrease the number of in situ tests and their prime cost. Due to the above said, the topic of examination is urgent and of applied importance.

Object of examination: new type of vertical submersible centrifuge

Subject of examination: models and methods to assess the performance, reliability, durability and efficiency of a vertical submersible centrifuge.

Goal: to develop new methods to assess the reliability, durability and performance of devices for suspension separation – centrifuges.

Scientific issue: plotting of centrifuge models for calculations, designing and operation by a theory of reliability and random processes as well as criteria and conditions of performance and efficiency.

The following tasks were fulfilled to achieve the goal:

- review of processes and designs of centrifuging systems;
- two models were plotted for precipitation centrifuging and vibration reliability of the vertical submersible centrifuge. The models allow decreasing the of number of experiments as well as the cost of research and design works in justification of technologies,
- criteria were set and quantitative method was developed to define an optimal rotation frequency of the vertical submersing centrifuge shaft,
- new software was developed, patented and implemented allowing a safe operation mode to be defined from the vibration reliability viewpoint.

The work is both theoretical and applied. The proposed methods, models and software can be used when designing, manufacture and operating vertical submersible centrifuges as well as other devices of the similar design.

Some Problems of Spent Fuel Reprocessing

Alexander Ochkin[1], Dmitry Gladilov[1] and Sergey Nekhaevskiy[1]

D.Mendeleev University of Chemical Technology of Russia, Miusskay Sq. 9, 125049, Moscow, Russia, e-mail: ochkin@rctu.ru

Introduction

The content of the spent fuel of WWER-440 at burn rate 33,4 MW*d/kg was published in [1]. It includes about 957 kg of uranium, 0.445 kg of neptunium-237, 9.2 kg plutonium, 124 g of americium and curium and 33.4 kg of fission products. The development of the nuclear energetics came the burn rate to 50 MW*d/kg and the reprocessing of MOX fuel can increase of plutonium concentration. Then the content of americium and curium increases more quickly than the burn rate. The aim of this report is an estimation of tendency in the fuel reprocessing.

Extraction system

The fuel reprocessing is based at PUREX process. The composition of the organic phase can be expressed as H_2O-HNO_3-$UO_2(NO_3)_2$-$Pu(NO_3)_4$-TBP-diluent. The concentration of neptunium is very small and is neglected. The aqueous phase contented HNO_3 and nitrates of fission products (FP), americium and curium. Residual concentrations in the aqueous phase are equal to 0.01% of uranium, 0.025% of plutonium and 0.5% of neptunium [2]. The problem of removal of americium and curium from HLW is very important (see e.g. [3]).

The system H_2O-HNO_3-$UO_2(NO_3)_2$-$Pu(NO_3)_4$-TBP-diluent has been explored many times. The molar concentrations were used during calculations of the equilibrium. The determination of thermodynamic activities of components of the organic phase is impossible in this case.

The alternative approach was demonstrated in [4]. The calculations have been made for the system H_2O-HNO_3-$UO_2(NO_3)_2$-TBP-diluent. The Pu effect can be considered afterwards. Equilibrium concentrations for considered systems are given here [5-7].

The mole fractions are used always as the concentration scale. Gibbs-Duhem equation is used to calculate activity of a component "i" on concentrations of other components

$$x_i d\ln a_i + \sum x_j d\ln a_j = 0 \qquad (1)$$

The following equation is true in all the cases

$$x_i d\ln x_i + \sum x_j d\ln x_j = 0 \qquad (2)$$

The other form of Gibbs-Duhem equation can be got after deduction of equation (2) from (1)**:**

$$x_i d\ln f_i + \sum x_j d\ln f_j = 0 \qquad (3)$$

It is impossible to change the rational activity coefficients f_i for the molar ones y_i or the molal ones γ_i. It should be noted that a cross differentiation relation has been used to calculate effect of water concentration on activity coefficients of other components

$$(\partial \ln a_i/\partial m_j)_{mi.mk} = (\partial \ln a_j/\partial m_i)_{mj.mk} \qquad (4)$$

where the first derivative is calculated when m_i = constant and m_k = constant. A similar equation can be obtained when activities a_i and a_j are replaced by rational activity coefficients f_i and f_j correspondingly.

There are three groups of interaction that should be taken into account during the calculations of activity coefficients. The interaction of components 1 and 2 can be taken into account as

$$\ln f_1 = b_1 \varphi_2^{\,n} \quad \text{or} \quad f_1 = \exp(b_1 \varphi_2^{\,n}) \qquad (5)$$

where φ_2 is a volume fraction of second component. $2.0<n\leq 2.2$. At first the interaction of H_2O with TBP was described with the equation

$$x_w = K_t \cdot \varphi_t \cdot a_w \cdot \exp(b_1 \cdot \varphi_t^{\,n}) + k_2 \cdot [K_t \cdot \varphi_t \cdot a_w \cdot \exp(b_1 \varphi_t^{\,n})]^2 + K_d \cdot \varphi_d \cdot a_w \qquad (6)$$

where the indexes “t” and “d” are related to TBP and the diluents respectively. An interaction between water and TBP is taken into account in equation (6) in accordance with equation (5) and the linear additively of the water solubility is presumed.

The mass action law has been used to calculate the formation of solvates from i acid molecules and j TBP molecules is calculated as

$$x_{ij} = K_{11} \cdot a_a \cdot a_t^j / f_{11} \quad (7)$$

where a_a is an activity of the acid. f_{ij} is an activity coefficient of the solvate and can be calculated as

$$f_{ij} = \exp[h_{ij}(a_{ij} - 1)] \quad (8)$$

where h_{ij} is a hydration ratio of the solvate.

The concentrations of di-solvate of uranyl nitrate can be calculated as

$$K_{ex} = a_{ds}/(a_{UN} \cdot a_t^2) \quad (9)$$

where a_{ds}. a_{UN} and a_t are activities of di-solvate, uranyl nitrate and TBP respectively. Then

$$\boldsymbol{x}_{ds} = K_{ex} \cdot a_{UN} \cdot x_t^2 \cdot f_t^2 / f_{ds} \quad (10)$$

where the index “ds” is related to di-solvate. The interaction between molecules of di-solvate and TBP were taken into account through equation (5) when values of f_t and f_{ds} were calculated. A water activity a_w effects on f_t but do not effects on f_{ds}.

Results

Results of the calculation of systems: H_2O-HNO_3-TBP, H_2O-HNO_3-TBP-n-dodecane and H_2O-$UO_2(NO_3)_2$-TBP have been presented in Table 1.

Table 1. Main results (n is a number of points, s_i is an average relative error, δ_i is an average relative deviation of experimental and calculated data).

System	n	Component	s_i	δ_i
H_2O-HNO_3-TBP	31	H_2O	0.030	0.022
		HNO_3	0.012	0.023
		TBP	-	0.0036
H_2O-$UO_2(NO_3)_2$ - TBP	27	H_2O	0.066	0.074
		$UO_2(NO_3)_2$	0.070	0.061
H_2O-HNO_3-TBP-*n*-dodecane	94	HNO_3	0.025	0.041
		TBP	-	0.072

Conclusion

The results given in Table 1 show that average relative deviations and average relative errors are approximately near. More exact estimation of the results can be made after the comparison of the deviations of experimental and calculated data in all the considered systems. The example of the comparison of the results of H_2O-$UO_2(NO_3)_2$-TBP system will be given in the next paper. The plutonium effect perhaps is not too big due to its small concentration.

References

[1] A.G.Zelenkov et al., *Atomic Energy (Russ.)* **51**, 53 (1981).
[2] Y.V.Glagolenko et al., *Voproci radiacionnoy besopacnocti (Issus of radiation safety)* N 2, 3 (1997).
[3] C. Poinssot et al. Atalante 2012 - Nuclear Chemistry For Sustainable Fuel Cycles. Book of Abstracts. P. 71. 2012, Montpeller.
[4] A.Ochkin et al. *Ibid.* P. 68. 2012, Montpeller.
[5] W.Davis et al., *J. inorg. nuclear chem.* **28**, 2001 (1966).
[6] W.Davis et al. Proc. of the International Conference held at Gotheborg. Sweden. 27 August – 1 September 1966. North Holland Publishing Company. Amsterdam. 1967. p. 343.
[7] A.V.Ochkin et al., *Russ. J. of phys. chemistry* **84,** 1526 (2010).

Estimation of the radiation hazard of curium after reprocessing of spent fuel

A. Ochkin[1], D. Gladilov[1] and S. Stefanovsky[2]

[1] *D.Mendeleev University of Chemical Technology of Russia, Miusskay Sq. 9, 125049, Moscow, Russia, e-mail: ochkin@rctu.ru*
[2]*SIA «RADON», 7 Rostovsky 2/14, Moscow, Russia*

Introduction

The modern spent nuclar fuel (SNF) reprocessing is based on the PUREX-process. Resulting HLW contains less than 0.01% of uranium, 0.025% of plutonium and 0.5% of neptunium [1]. Other radionuclides remaining in HLW are americium, curium and fission products. Current situation requires highr safety level which can be achieved by either decreasing of americium and curium contents in HLW or extracting americium only (EXAM-process) [2].

Experimental data

Radionuclide composition in spent fuel of WWER-440 [3] is given in Table 1. These data are taken as a base. Then activities of 18 radionuclides are calculated for three periods: after SNF discharge, after storage for 5 years and after reprocessing. Decrease of the activities of ^{241}Pu, ^{242}Cm, ^{243}Cm and ^{244}Cm after storage for 5 years are given in Table 1.

Table 1. Composition of SNF of WWER-440 [3] and activities of actinides

Radio-nuclide	$T_{1/2}$, years	Dose coefficient $\varepsilon\cdot10^7$, Sv/Bq	Content, kg/t U [3]	Activity *A*, Bq/t U		
				After discharge	After storage for 5 years	After repro-cessing
^{232}U	68.9	3.3	$9.00\cdot10^{-7}$	$7.44\cdot10^{8}$	$1.59\cdot10^{9}$	$1.59\cdot10^{5}$
^{234}U	$2.45\cdot10^{5}$	0.49	0.215	$4.96\cdot10^{10}$	$5.09\cdot10^{10}$	$5.09\cdot10^{6}$
^{235}U	$7.04\cdot10^{8}$	0.47	11.2	$8.95\cdot10^{8}$	$8.96\cdot10^{8}$	$8.96\cdot10^{4}$
^{236}U	$2.34\cdot10^{7}$	0.47	4.50	$1.08\cdot10^{10}$	$1.08\cdot10^{11}$	$1.08\cdot10^{7}$
^{238}U	$4.47\cdot10^{9}$	0.45	941	$1.17\cdot10^{10}$	$1.17\cdot10^{10}$	$1.17\cdot10^{6}$
^{237}Np	$2.14\cdot10^{6}$	1.1	0.445	$1.16\cdot10^{10}$	$4.71\cdot10^{9}$	$2.35\cdot10^{7}$
^{236}Pu	2.85	2.0	$1.60\cdot10^{-6}$	$3.15\cdot10^{10}$	$9.41\cdot10^{9}$	$2.35\cdot10^{6}$
^{238}Pu	87.7	2.3	0.137	$8.67\cdot10^{13}$	$9.16\cdot10^{13}$	$2.29\cdot10^{10}$
^{239}Pu	$2.41\cdot10^{4}$	2.5	5.37	$1.23\cdot10^{13}$	$1.23\cdot10^{13}$	$3.08\cdot10^{9}$
^{240}Pu	$6.56\cdot10^{3}$	2.5	2.17	$1.82\cdot10^{13}$	$1.82\cdot10^{13}$	$4.56\cdot10^{9}$
^{241}Pu	14.4	0.048	1.06	$4.04\cdot10^{15}$	$3.18\cdot10^{15}$	$7.94\cdot10^{11}$
^{242}Pu	$3.76\cdot10^{5}$	2.4	0.430	$6.25\cdot10^{10}$	$6.25\cdot10^{10}$	$1.56\cdot10^{7}$
^{241}Am	432	2.0	0.0410	$5.20\cdot10^{12}$	$3.38\cdot10^{13}$	$3.38\cdot10^{13}$
^{242m}Am	152	1.9	$6.40\cdot10^{-4}$	$2.30\cdot10^{11}$	$2.25\cdot10^{11}$	$2.25\cdot10^{11}$
^{243}Am	$7.38\cdot10^{3}$	2.0	0.0490	$3.61\cdot10^{11}$	$3.61\cdot10^{11}$	$3.61\cdot10^{11}$
^{242}Cm	0.446	0.12	0.0136	$1.67\cdot10^{15}$	$9.29\cdot10^{11}$	$9.29\cdot10^{11}$
^{243}Cm	28.5	1.5	$3.80\cdot10^{-4}$	$7.26\cdot10^{11}$	$6.45\cdot10^{11}$	$6.45\cdot10^{11}$
^{244}Cm	18.1	1.2	0.0197	$5.89\cdot10^{13}$	$4.87\cdot10^{13}$	$4.87\cdot10^{13}$
^{245}Cm	$8.50\cdot10^{3}$	2.1	$1.03\cdot10^{-3}$	$6.54\cdot10^{9}$	$6.54\cdot10^{9}$	$6.54\cdot10^{9}$
^{246}Cm	$4.73\cdot10^{3}$	2.1	$6.90\cdot10^{-5}$	$7.84\cdot10^{5}$	$7.84\cdot10^{5}$	$7.84\cdot10^{5}$
		$\sum$	**967**	$\mathbf{5.89\cdot10^{15}}$	$\mathbf{3.38\cdot10^{15}}$	$\mathbf{8.57\cdot10^{13}}$

Radiation hazard

The activities of original radionuclides together with their decay products were calculated as a function of time. The radiation hazard of 18 radionuclides has been calculated as a product of $A\varepsilon$ where A is an activity of radionuclide and ε is a dose coefficient through ingestion [4]. The results of the calculation for 8 curium and americium radionuclides are given in Table 2. The results for other radionuclides are presented as a sum (1) ∑U+Pu**.** The data for the radiation hazard of ^{90}Sr and ^{137}Cs is also given in Table 2.

Table 2. Alteration of radiation hazard of actinides during HLW storage

Radio-nuclide	Radiation hazard $A\cdot\varepsilon$, Sv/t U after storage during						
	0 years	10 years	100 years	500 years	1000 years	10000 years	50000 years
(1) ∑U+Pu	**$1.10\cdot10^4$**	**$1.11\cdot10^4$**	**$8.94\cdot10^3$**	**$4{,}41\cdot10^3$**	**$2.89\cdot10^3$**	**631**	**217**
^{242}Cm	$1.11\cdot10^4$	$1.00\cdot10^3$	493	21,0	0.490	0.346	1.37
^{243}Cm	$9.66\cdot10^4$	$7.62\cdot10^4$	$9.10\cdot10^3$	193	189	146	46.2
^{244}Cm	$5.84\cdot10^6$	$3.99\cdot10^6$	$1.59\cdot10^5$	$3{,}19\cdot10^4$	$3.03\cdot10^4$	$1.17\cdot10^4$	173
^{245}Cm	$1.37\cdot10^3$	$1.39\cdot10^3$	$1.55\cdot10^3$	$2{,}03\cdot10^3$	$2.28\cdot10^3$	$1.23\cdot10^3$	51.9
^{246}Cm	0.165	0.164	0.162	0,153	0.143	0.0402	0.0023
(2) ∑Cm	**$5.95\cdot10^6$**	**$4.08\cdot10^6$**	**$1.80\cdot10^5$**	**$3{,}42\cdot10^4$**	**$3.57\cdot10^4$**	**$1.31\cdot10^4$**	**272**
^{241}Am	$6.76\cdot10^6$	$6.65\cdot10^6$	$5.76\cdot10^6$	$3{,}03\cdot10^6$	$1.36\cdot10^6$	824	$1.43\cdot10^3$
^{242m}Am	$4.26\cdot10^4$	$4.68\cdot10^4$	$4.93\cdot10^4$	$1{,}30\cdot10^4$	$1.29\cdot10^3$	26.1	105
^{243}Am	$7.22\cdot10^4$	$7.22\cdot10^4$	$7.18\cdot10^4$	$7{,}02\cdot10^4$	$6.82\cdot10^4$	$4.25\cdot10^4$	$9.74\cdot10^3$
(3) ∑Am	**$6.87\cdot10^6$**	**$1.09\cdot10^7$**	**$6.06\cdot10^6$**	**$3{,}12\cdot10^6$**	**$1.47\cdot10^6$**	**$4.34\cdot10^4$**	**$1.13\cdot10^4$**
^{90}Sr/^{90}Y	$9.21\cdot10^7$	$7{,}26\cdot10^7$	$8{,}51\cdot10^6$	621	**0**	**0**	**0**
^{137}Cs	$5.20\cdot10^7$	$4{,}13\cdot10^7$	$5{,}19\cdot10^6$	515	**0**	**0**	**0**

The radiation hazard coming from americium significantly surpasses the one from other radionuclides and its separation from HLW is necessary. The radiation hazard of curium after 500 years storage is about one hundredth of the hazard of americium. However curium should perhaps be moved off also after separation of daughter radionuclides of plutonium. The time of the separation can be chosen between 50 and 100 years. The residual activities of curium radionuclides after the separation of Pu after 100 years are given in Table 3.

Table 3. Residual activities of Cm radionuclides after 100 years storage and separation of Pu

Radio-nuclide	Radiation hazard $A\cdot\varepsilon$, Sv/t U after storage in					
	0 years	10 years	100 years	After separa-tion of Pu	500 years	1000 years
^{242}Cm	$1.11\cdot10^4$	$1.00\cdot10^3$	493	0	0	0
^{243}Cm	$9.66\cdot10^4$	$7.62\cdot10^4$	$9.10\cdot10^3$	$8{,}49\cdot10^3$	19	16
^{244}Cm	$5.84\cdot10^6$	$3.99\cdot10^6$	$1.59\cdot10^5$	$1{,}27\cdot10^5$	4	3
^{245}Cm	$1.37\cdot10^3$	$1.39\cdot10^3$	$1.55\cdot10^3$	$1{,}36\cdot10^3$	$1{,}85\cdot10^3$	$2.10\cdot10^3$
^{246}Cm	0.165	0.164	0.162	0,162	0,153	0.143
(2) ∑Cm	**$5.95\cdot10^6$**	**$4.08\cdot10^6$**	**$1.80\cdot10^5$**	**$1{,}38\cdot10^5$**	**$1{,}87\cdot10^3$**	**$2.12\cdot10^3$**

References.

[1] Y.V.Glagolenko et al. *Voproci radiacionnoy besopacnocti (Issus of radiation safety)*, N 2, 3 (1997).
[2] C.Marie et al. Atalante 2012 – Nuclear Chemistry for Sustainable Fuel Cycles. September 2-7, Montpellier, France. Book of Abstracts. 2012, CEA.
[3] A.G.Zelenkov et al. *Atomic Energy (Russ.)* **51**, 53 (1981).
[4] N.S.Babaev et al. *Atomic Energy (Russ.)* **98**, 123 (2005).

Calculation of Organic Phase Composition in H_2O-$UO_2(NO_3)_2$-TBP System

Alexander Ochkin[1], Sergey Nekhaevskiy[1] and Dmitry Gladilov[1]

D.Mendeleev University of Chemical Technology of Russia, Miusskay Sq. 9, 125049, Moscow, Russia, e-mail: ochkin@rctu.ru

Introduction

H_2O-HNO_3-$UO_2(NO_3)_2$-TBP-diluent system is the basic one for PUREX process. Usually this system is divided in some sub-systems separately. H_2O-$UO_2(NO_3)_2$-TBP system is one of the most important sub-systems. Two variants of the description of this system were presented [1,2]. The concentrations of uranyl nitrate c_{Uo} and water c_{wo} in the organic phase were determined in the experiment [3]. The concentration of free TBP c_{tf} had been calculated as

$$c_{tf} = c_{tt} - 2c_{Uo} \quad (1)$$

where c_{tt} is a total concentration of TBP. A dependence of c_{tf} on c_{Uo} should be taken into account. Two approaches of calculation of molar concentrations were compared.

Experimental data

Table 1. System H_2O-$UO_2(NO_3)_2$-TBP [1, 3] (initial concentrations of uranium c_{Uaq} and m_U, a_w and a_U are activities of water and uranium, x_2 and x_2 are activities of TBP and uranium)

№ ex.	c_{Uaq}, mol/L	c_{Uo}, mol/L	c_{wo}, mol/L	m_U, mol/kg	c_{tt}, mol/L	a_w	a_U	x_2	x_3
1	0.0394	0.0375	3.358	0.0396	3.413	0.9995	$5.97\cdot10^{-5}$	0.4955	0.0056
2	0.0403	0.0316	3.366	0.0405	3.411	0.9995	$6.33\cdot10^{-5}$	0.4964	0.0047
3	0.0497	0.0529	3.155	0.0500	3.420	0.9993	$1.08\cdot10^{-4}$	0.5081	0.0081
4	0.0534	0.076	3.295	0.0537	3.412	0.9992	$1.30\cdot10^{-4}$	0.4909	0.0115
5	0.0544	0.0672	3.196	0.0548	3.403	0.9992	$1.36\cdot10^{-4}$	0.5011	0.0103
6	0.0692	0.122	3.431	0.0697	3.378	0.9988	$2.52\cdot10^{-4}$	0.4687	0.0182
7	0.0754	0.163	3.120	0.0760	3.402	0.9986	$3.15\cdot10^{-4}$	0.4822	0.0257
8	0.079	0.149	2.933	0.0796	3.385	0.9985	$3.56\cdot10^{-4}$	0.5018	0.0241
9	0.0931	0.26	3.14	0.0939	3.351	0.9981	$5.46\cdot10^{-4}$	0.4543	0.0417
10	0.122	0.358	2.504	0.1235	3.361	0.9972	0.001127	0.4803	0.0650
11	0.129	0.418	2.504	0.1306	3.341	0.9969	0.001309	0.4615	0.0770
12	0.13	0.44	2.785	0.1315	3.314	0.9969	0.001335	0.4301	0.0777
13	0.153	0.53	2.436	0.1548	3.308	0.9960	0.00208	0.4311	0.1017
14	0.156	0.536	2.402	0.1581	3.307	0.9959	0.00221	0.4321	0.1036
15	0.184	0.66	1.933	0.1869	3.298	0.9947	0.00352	0.4327	0.1444
16	0.234	0.834	1.646	0.2386	3.258	0.9923	0.00712	0.3907	0.2049
17	0.244	0.862	1.416	0.2488	3.264	0.9918	0.00806	0.4034	0.2258
18	0.335	1.054	1.003	0.3439	3.227	0.9867	0.02184	0.3524	0.3318
19	0.409	1.15	0.738	0.4232	3.213	0.9820	0.04312	0.3259	0.4106
20	0.592	1.323	0.457	0.6209	3.173	0.9685	0.1688	0.2286	0.5734
21	0.634	1.349	0.461	0.6649	3.164	0.9653	0.2194	0.2049	0.5926
22	0.796	1.419	0.278	0.8441	3.153	0.9512	0.5780	0.1567	0.7052
23	0.812	1.427	0.31	0.8660	3.148	0.9495	0.6452	0.1449	0.7025
24	1.02	1.474	0.212	1.111	3.139	0.9286	2.031	0.1018	0.7853
25	1.042	1.49	0.208	1.132	3.134	0.9268	2.221	0.0831	0.8046
26	1.295	1.53	0.16	1.428	3.124	0.8999	7.572	0.0363	0.8725
27	1.727	1.548	0.15	1.979	3.118	0.8481	53.79	0.0129	0.8999

Results of calculation

The results of the calculations for two variants of optimization are presented in Table 2: a) set of molar concentrations of c_{Uo}, c_{wo} and c_{tt} and b) c_{Uo}, c_{wo} and c_{tf}.

Table 2. Results of calculation

№ ex.	Initial data			Variant 1			Variant 2		
	m_U, mol/kg	c_{Uo}, mol/L	c_{tf}, mol/L	c_{Uo}. mol/L	c_{wo}. mol/L	c_{tt}. mol/L	c_{Uo}. mol/L	c_{wo}. mol/L	c_{tf}. mol/L
1	0.0396	0.0375	3,351	0.0318	3.3356	3.420	0.0332	3.506	3.352
2	0.0405	0.0316	3,364	0.0336	3.3320	3.420	0.0351	3.497	3.348
3	0.0500	0.0529	3,328	0.0561	3.2878	3.417	0.0581	3.404	3.300
4	0.0537	0.076	3,265	0.0666	3.2668	3.416	0.0688	3.364	3.278
5	0.0548	0.0672	3,292	0.0696	3.2606	3.415	0.0718	3.353	3.271
6	0.0697	0.122	3,149	0.1215	3.1539	3.408	0.1236	3.176	3.161
7	0.0760	0.163	3,073	0.1469	3.1009	3.404	0.1485	3.098	3.108
8	0.0796	0.149	3,117	0.1624	3.0679	3.401	0.1635	3.052	3.076
9	0.0939	0.26	2,845	0.2278	2.9297	3.390	0.2259	2.870	2.942
10	0.1235	0.358	2,656	0.3742	2.6154	3.364	0.3610	2.508	2.649
11	0.1306	0.418	2,516	0.4095	2.5401	3.357	0.3930	2.427	2.579
12	0.1315	0.44	2,446	0.4143	2.5302	3.356	0.3973	2.416	2.570
13	0.1548	0.53	2,258	0.5265	2.2895	3.335	0.5135	2.195	2.312
14	0.1581	0.536	2,246	0.5421	2.2561	3.332	0.5120	2.135	2.319
15	0.1869	0.66	1,986	0.6677	1.9890	3.307	0.6248	1.873	2.072
16	0.2386	0.834	1,597	0.8551	1.5941	3.268	0.7966	1.499	1.694
17	0.2488	0.862	1,546	0.8868	1.5281	3.262	0.8262	1.437	1.629
18	0.3439	1.054	1,124	1.1119	1.0638	3.214	1.0460	1.005	1.142
19	0.4232	1.15	0,916	1.2307	0.8239	3.188	1.1699	0.778	0.8668
20	0.6209	1.323	0,529	1.3889	0.5039	3.153	1.3475	0.468	0.4713
21	0.6649	1.349	0,468	1.4093	0.4608	3.148	1.3719	0.427	0.4169
22	0.8441	1.419	0,316	1.4666	0.3360	3.136	1.4411	0.312	0.2623
23	0.8660	1.427	0,296	1.4713	0.3241	3.134	1.4472	0.302	0.2487
24	1.111	1.474	0,192	1.5094	0.2263	3.126	1.4950	0.222	0.1420
25	1.132	1.49	0,155	1.5115	0.2170	3.126	1.4977	0.218	0.1359
26	1.428	1.53	0,064	1.5331	0.1393	3.121	1.5255	0.169	0.0742
27	1.979	1.548	0,023	1.5492	0.0451	3.119	1.5465	0.121	0.0280
				δ_U=5.6%	δ_w=7.2%	δ_t= 0.46%	δ_U=6.4%	δ_w=7.4%	δ_t=9.9%

Conclusion

Variant 1: extraction constant K_{ex}= 316, parameter interaction of TBP and di-solvate b=0.426. The major problem with Variant 1 lies with results number 26 and 27, unfortunately the figures for c_{wo} in results achieved dramatically surpass the numbers in initial data thus making it use for calculations of reprocessing doubtful. As for Variant 2: K_{ex}= 315, b=0.429. Additionally, while the general error of calculations remain on the same level as in Variant 1 the error numbers for experiments 26 and 27 lie within acceptable range.

References

[1] A.Ochkin et al. 19th Intern. Solvent Extraction Conf. 3-7 October 2011 Santiago. Chile. 2011. Paper 131.
[2] A.Ochkin et al. Atalante 2012 - Nuclear Chemistry For Sustainable Fuel Cycles. Book of Abstracts. P. 68.
[3] W.Davis et al. Solvent Extraction Chemistry. Proceedings of the International Conference held at Gotheborg. Sweden. 27 August – 1 September 1966. North Holland Publishing Company. Amsterdam. 1967. p. 343-351.

First principles calculations of XMCD spectra of $NpOs_2$ and $PuFe_2$

Jan Rusz,[1] F. Wilhelm[2], P. M. Oppeneer[1], G. Lander[3]

[1] *Department of Physics and Astronomy, Uppsala University, Box 516, S-75120 Uppsala, Sweden, e-mail: jan.rusz@fysik.uu.se*
[2] *European Synchrotron Radiation Facility (ESRF), B.P.220, F-38043 Grenoble, France*
[3] *European Commission, Joint Research Centre, Institute for Transuranium Elements, Postfach 2340, D-76125 Karlsruhe, Germany*

The actinide cubic Laves compounds $NpAl_2$, $NpOs_2$, $NpFe_2$, and $PuFe_2$ have been examined by X-ray magnetic circular dichroism (XMCD) at the actinide $M_{4,5}$ absorption edges [1]. They have the interesting feature that the *An-An* spacing is close to the so-called Hill limit so that substantial hybridization between the 5*f* states on neighbouring atoms is expected to occur.

We have performed electronic structure calculations of these compounds using the WIEN2k package [2], which implements the full-potential linearized augmented plane waves method with local orbitals to solve the Kohn-Sham equations. To deal with the strongly correlated nature of unfilled 5*f*-electron shells, we have performed both local spin density approximation (LSDA) calculations as well as LSDA+*U* calculations, which include explicitly the strong onsite Coulomb interactions in the 5*f*-electron subsystem. We have tested both the most common variants of the LSDA+*U*, namely the around mean-field (AMF) and fully localized limit (FLL) formulations. The spin orbital (SO) interaction, which is essential for actinide atoms, was included in the second variational step, where also the orbital potential was introduced, including its spin cross-term. The structure parameters were set to 7.189 Å, 7.528 Å, 7.144 Å, and 7.785 Å for $PuFe_2$, $NpOs_2$, $NpFe_2$, and $NpAl_2$, respectively.

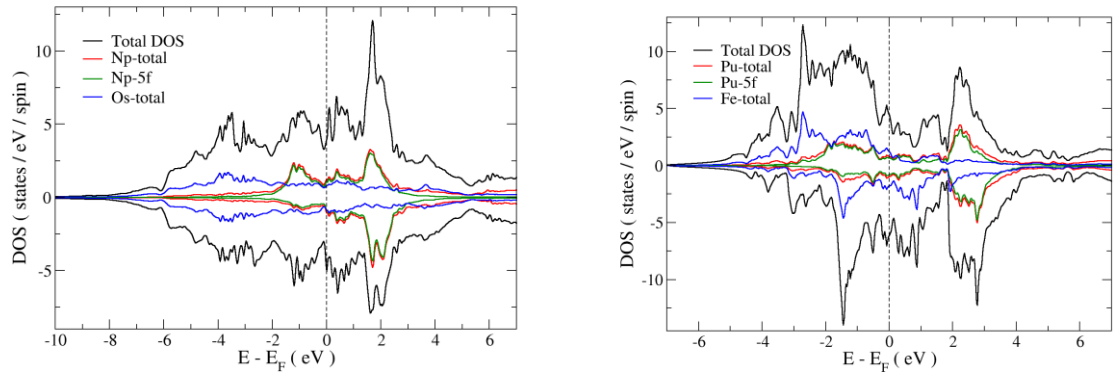

Fig.1: Spin-resolved and atom-projected density of states of $NpOs_2$ (left) and $PuFe_2$ (right).

Figure 1 shows calculated density of states for $NpOs_2$ and $PuFe_2$ compounds. For $NpOs_2$ (left panel) the calculations uses the AMF variant of LSDA+*U* with *U*=1eV and *J*=0.6eV and for the $PuFe_2$ (right panel) it shows results for an FLL calculations with *U*=2eV and *J*=0.6eV, respectively. These values turned out to agree most accurately with measured XMCD spectra, as is shown in Fig. 2, see below. The exchange splitting is very pronounced in $PuFe_2$ and that is caused by large magnetic moments on iron atoms. Contrary to that, the magnetic moments on Os atom in $NpOs_2$ are very small and of induced nature.

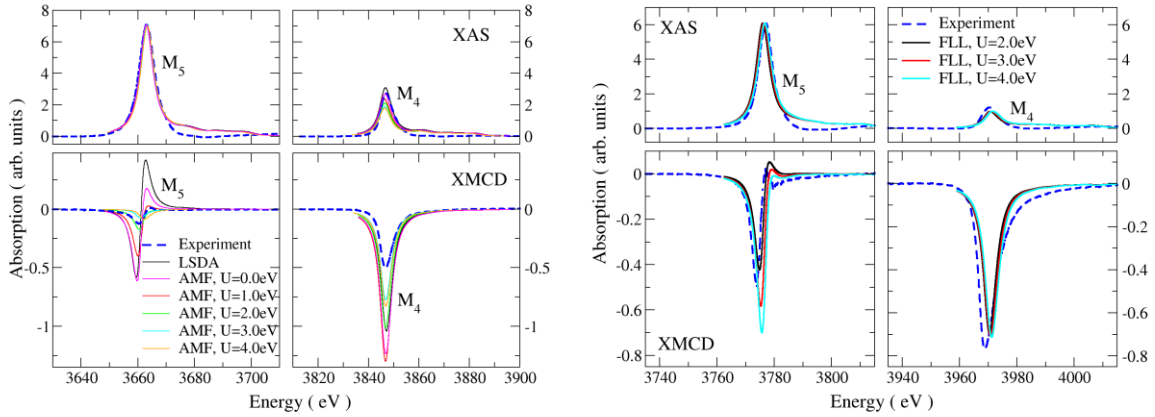

Fig.2: Summary of x-ray absorption spectra (XAS) and x-ray magnetic circular dichroism spectra on $M_{4,5}$ edge of Np in $NpOs_2$ (left panel) and $M_{4,5}$ edge of Pu in $PuFe_2$ (right panel). The experimental data are compared to theoretical calculations for various values of U parameter in LSDA+U exchange correlation potential.

The x-ray absorption spectra (XAS) have been simulated by the initial state approximation in which the absorption strength at the $M_{4,5}$ edges is a function of the projected density of states of unoccupied 5*f* states of the actinide element. The energy-dependent dipole transition matrix elements have been included. Figure 2 summarizes the resulting XAS spectra and their difference - the XMCD spectra. For every treated system we have performed several independent simulations - varying the strength of the onsite Coulomb repulsion characterized by the U parameter in the LSDA+U method. Typically we have calculated the spectra for U within the range from 0 to 4 eV. The value of J was set to 0.6 eV for both Np and Pu 5*f* electrons. Because of the strong influence of the spin-orbit interaction on the 3*d* core shell, the $3d_{3/2}$ and $3d_{5/2}$ core levels are split by approximately 200 eV.

Comparing the theoretical and experimental XAS spectra, the first-principles calculations reproduce the experimental findings with good qualitative accuracy with regard to the peak shapes, distance and branching ratio. These features are only very weakly sensitive to the chosen model of treatment of the 5f electrons. A certain degree of sensitivity on the strength of the onsite Coulomb correlations U can be seen on the intensity of the M_4 peak. Best agreement between theory and experiment is obtained for small values of U.

The XMCD spectra reveal much more details. Generally, the XMCD signal of $NpFe_2$ on the M_5 edge is very weak, compared to the XAS intensity. In the experimental spectra there is a sine-like oscillation, starting with negative values, switching the sign to a positive peak and monotonously decreasing to zero. The theoretical XMCD spectra at the M_5 edge show an interesting, rather strong sensitivity on the chosen model of the description of the 5*f* states. The sine-like signal is best reproduced by low U values.

For $PuFe_2$, it is the FLL variant of LSDA+U that provides the most satisfactory agreement with experimental spectra. The AMF LSDA+U calculations lead to a far too weak XMCD signal at the M_5 edge.

References

[1] F. Wilhelm, R. Eloirdi, J. Rusz, R. Springell, E. Colineau, P. M. Oppeneer, R. Caciuffo, A. Rogalev, and G. H. Lander, submitted.
[2] P. Blaha, K. Schwarz, G. K. H. Madsen, D. Kvasnicka, and J. Luitz, WIEN2k, *An Augmented Plane Wave + Local Orbitals Program for Calculating Crystal Properties*, Technische Universität Wien, Austria (2001).
[3] This work was supported by Swedish Research Council.

Recycling of Neodymium from Nd-Fe-B magnets

A. Saccone, S. De Negri, P. Solokha, M.Giovannini

Università di Genova, Dipartimento di Chimica e Chimica Industriale, Via Dodecaneso 31, 16146 Genova, Italy, e-mail: adriana.saccone@unige.it

Rare earth elements, although relatively abundant in the earth's crust, rarely occur in concentrated forms making them economically challenging to obtain. These elements are essential to critical components of many of modern-day technological devices and everyday electronics. Several "green" technologies depend on them since their unique properties can save weight and increase efficiency in products such as hybrid electric vehicles, generators in wind power plants, low energy light bulbs, etc. Today China stands for more than 95% of the world rare earths supply. Due to increasing global demand, the rare earth prices increased ten-fold between 2009 and 2011, and supplies, primarily in China, are in question due to quotas for China's internal use.

Of consequence, in order to promote a sustainable rare earth management there is a need to address strategies such as the improvement of alternative applications working without the use of rare earths, and the developing of recycling schemes, very uncommon issue until today [1], from scraps and end-uses. Moreover, the analysis of substitutions for rare earth elements has shown that a simple substitution of a rare earth compound with another compound is a quite rare case, since usually substitution requires a totally new product design. For this reason the recycling of rare earths should be taken into account to mitigate supply risk.

In particular in this communication the recycling of Nd (and Pr and Dy) from Nd-Fe-B permanent magnets will be considered. Several methods for recovering rare earths from magnet alloys have been investigated in the past, all based on the re-melting or oxidation of the alloy to recover Nd in the Nd_2O_3 form. An environmentally friendly recycling process, compared with the conventional chemical method, has been recently developed [2, 3]: the direct extraction and recovery of metallic Nd from Nd-Fe-B magnets by using liquid Mg as solvent, taking into account that Mg has very strong chemical affinity with Nd and hardly reacts with iron.

Experimental results obtained through scanning electron microscopy (SEM), energy dispersive X-ray spectroscopy (EDXS) and X-ray diffraction (XRD), on the diffusivity of Nd into Mg from Nd-Fe-B magnets will be presented and discussed highlighting the microstructural and the compositional change during the reaction.

References

[1] D. Schüler, M. Buchert, R. Liu, S. Dittrich, C. Merz, "*Study on Rare Earths and Their Recycling*" Öko-Institut e.V., Final Report The Greens/EFA Group in the European Parliament, Darmstadt, 2011. Öko-Institut e.V.

[2] K. Binnemans, P.T. Jones, B. Blanpain, T. Van Gerven, Y. Yang, A. Walton, M. Buchert, "*Recycling of Rare Earths: a Critical Review*", J. Cleaner Production (2013), doi:10.1016/j.jclepro.2012.12.037

[3] O. Takeda, T. H. Okabe, Y. Umetsu, "*Recovery of neodymium from a mixture of magnet scrap and other scrap*", J. Alloys and Compounds, 408-412 (2006) 387-390.

Acknowledgement

Fondazione CARIGE is kindly acknowledged for financial support (project "Riciclo di Neodimio da magneti permanenti per una sostenibilità energetica e ambientale", 2012).

The crystal structure peculiarities of novel R_4MgGe_{10-x} (R=La-Nd, Sm, Gd-Dy) germanides

P. Solokha[1], R. Freccero[1], S. De Negri[1], D. M. Proserpio[2], A. Saccone[1]

[1] *Università di Genova, Dipartimento di Chimica e Chimica Industriale, Via Dodecaneso 31, 16146 Genova, Italy, e-mail: pavlo.solokha@unige.it*
[2] *Università di Milano, Dipartimento di Chimica Strutturale e Stereochimica Inorganica, Via Venezian 21, 20133 Milano, Italy*

Ternary rare-earth metal silicides and germanides are of great interest in understanding the interplay among structure, chemical bonding and physical properties of polar and Zintl intermetallic phases [1]. During our previous investigations, two novel compounds of La_2MgGe_6 and La_4MgGe_{10-x} (x= 0.36) compositions have been revealed in the La–Mg–Ge ternary system [2]. The main goal of the current study was to ascertain the crystal structure model for La_4MgGe_{10-x} and to explore more on the constitutional peculiarities obtained by substituting La with other rare-earth (R) elements in the respective systems.

The alloys for analysis were synthesized in a resistance furnace. The thermal cycle steps were following: (1) fast heating up to 950 °C, (2) dwell for 20 min, (3) slow cooling to room temperature. Microstructure and phase compositions of the prepared alloys were checked by scanning electron microscopy (SEM) coupled with energy dispersive X-ray spectroscopy (EDXS). X-ray single crystal/powder diffraction techniques were used to determine/ensure crystal structures of the studied series.

On the contrary to La–Mg–Ge, the heavier lanthanides containing ternary systems form only the R_4MgGe_{10-x} ternary phase (R=La-Nd, Sm, Gd-Dy). At the same conditions, the rest of rare-earths do not form any ternary compound in the Ge-rich region of phase diagram.

The twinning phenomenon is still a serious problem when looking for a correct structural model. In the case of R_4MgGe_{10-x} series, the non-merohedral type of twinning takes place. All tested crystals (including those with diverse rare-earth constituents) show the same twin law describing mutual domains orientation. It corresponds to the twofold rotation axis along the monoclinic ***a*** axis (1 0 0 0 -1 0 -1/2 0 -1), what is a common case for monoclinic symmetry. When correctly accounted for a twinning law, the structure model solution and further the full-matrix least-squares refinement for R_4MgGe_{10-x} compounds were straightforward by using SHELX-97 [3]. The relevant structure refinement data along with atomic coordinates for La_4MgGe_{10-x} are shown in Table 1. All compounds are isostructural, crystallizing in the novel La_4MgGe_{10-x} structure type (*x* represents the compositional variation due to the partially occupied 8*j* site). The linear change (Fig. 1a) of the R_4MgGe_{10-x} unit cell volumes *vs.* the size of R^{3+} ions confirms well the effect of the lanthanide contraction and reflects the same chemical role of the electropositive component. The geometrical concept of liner intergrowth structural series [4] could be conveniently applied to R_4MgGe_{10-x} compounds. Following this approach the structure of title compounds could be viewed as composed of alternating slabs of RX_2 and RX_5 compositions. The general formula for this series (normalized per number of atoms in the unit cell) is $R_{4n+4m}X_{8m+20}$, where *m* and *n* stand for the number of RX_2 and RX_5 fragments respectively. For the idealized R_4MgGe_{10} composition, *m*=3, *n*=1 (to fit proposed earlier general formula, Mg and Ge species were not differentiated). The RX_2 fragment is topologically identical with the very common for intermetallics AlB_2-type atoms arrangement; instead, the RX_5 fragment may be described as a defect $CeRe_4Si_2$ structure type. A spatial distribution of these fragments along the stacking direction is shown in Fig. 1b.

Table 1. Crystallographic data for the $La_4MgGe_{9.64(1)}$ single crystal and experimental details of the structure determination.

Empirical formula	$La_4MgGe_{9.64(1)}$
EDXS composition	$La_{26.7}Mg_{10.0}Ge_{63.3}$
Space group	*C*2/*m* (№ 12)
Pearson symbol, Z	*mS*60-1.46, 4
Unit cell dimensions:	
a, Å	8.8403(8)
b, Å	8.6756(8)
c, Å	17.7092(16)
β, °	97.159(1)
V, Å^3	1347.6(2)
k (BASF)	0.47(1)
Data/parameters	2280/82
Final R indices [$I > 2\sigma(I)$]	R1 = 0.0374; wR2 = 0.0822
$\Delta\rho_{fin}$, e·Å^{-3}; GOF	3.54/-3.65; 1.03

Atom	Site	*x/a*	*y/b*	*z/c*
La1	4*i*	0.5995(3)	0	0.39687(6)
La2	8*j*	0.0494(3)	0.24987(9)	0.19824(3)
La3	4*i*	0.0978(3)	0	0.39672(6)
Ge1	4*i*	0.0642(3)	0	0.06705(13)
Ge2	4*i*	0.4698(3)	0	0.06656(14)
Ge3	8*j*	0.2668(3)	0.19993(9)	0.06693(7)
Ge4	4*i*	0.1847(6)	0	0.73895(12)
Ge5	4*i*	0.3121(6)	0	0.25119(13)
Ge6	8*j*	0.3344(6)	0.2454(2)	0.33592(7)
Ge7*	8*j*	0.1115(7)	0.2493(3)	0.52594(11)
Mg	4*i*	0.7734(1)	0	0.1019(3)

U_{eq} thermal displacement values show a flat distribution for all sites being of ~0.01 Å^2 of magnitude

* SOF of this site is 0.82(6)

It is worth noting that one of the RX_2 slabs is deficient, what is reflected also in the non-stoichiometric formula R_4MgGe_{10-x}. Looking for chemical reasons of this phenomenon one may refer to the RGe_{2-x} compounds, which manifest the presence of similar Ge-deficient positions in analogous AlB_2-type slabs. Accurate electron structure calculations on the La_4MgGe_{10-x}, currently in progress, should shed more light on the chemical bonding picture.

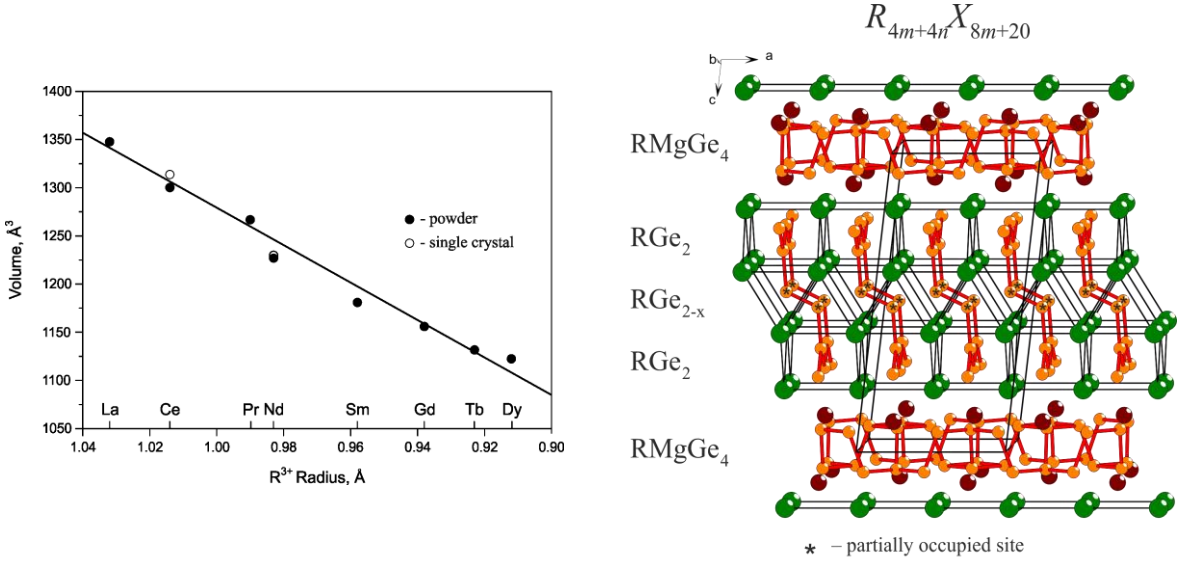

a) b)

Fig. 1. a) Trend of the unit cell volumes of R_4MgGe_{10-x} phases *vs*. size of R^{3+} ions. b) Linear packing of the RGe_2 and $RMgGe_4$ slabs for the title compounds.

References

[1] S. M. Kauzlarich, Ed. Chemistry, *Structure and Bonding of Zintl Phases and Ions*; VCH Pub., 1996.

[2] A. Saccone et al., 18-th International Conference on Solid Compounds of Transitional Elements, Lisbon (Portugal), 31 March -5 April 2012. – SUN_P24, P. 120.

[3] Sheldrick G. M., *SHELXL–97: Program for Crystal Structure Refinement*; University of Göttingen: Germany, 1997.

[4] Grin, Y. N. *The Intergrowth Concept as a Useful Tool to Interpret and Understand Complicated Intermetallic Structures*. In *Modern Perspectives in Inorganic Crystal Chemistry*; Parthé, E., Ed.; Kluwer Academic Publishers: Norwell, MA, 1992.

Influence of hydrostatic pressure on superconducting system YB_6

Takáčová I., Gabáni S., Pristáš G., Gažo E. and Flachbart K.

Institute of Experimental Physics SAS, Watsonova 47, SK-04001 Košice, Slovakia

The superconductor YB_6 has the second highest critical temperature, $T_c \approx 8$ K, among the boride family MB_n. In recent years many of the properties of YB_6 have been intensely investigated, above all the specific heat, resistivity, magnetic susceptibility, thermal expansion, electronic band structure and point-contact spectra. From these studies we can define YB_6 as the conventional type-II BCS superconductor, where the strong coupling superconductivity of YB_6 with $2\Delta / k_B T_c \approx 4.2$ is mediated by the phonon mode of Y atoms located at ≈ 8 meV. To our knowledge there is only a single experimental study published on the pressure effect on the superconducting properties of YB6 [1] in the pressure range up to 0.92 GPa.

We present the first investigation of high-pressure electrical resistivity of YB_6 using diamond-anvil cell (DAC) in mini ^{3}He-^{4}He dilution refrigerator down to 60 mK. From these experiments, mainly the pressure dependences of the transition temperature T_c and the upper critical field H_{c3} were obtained.

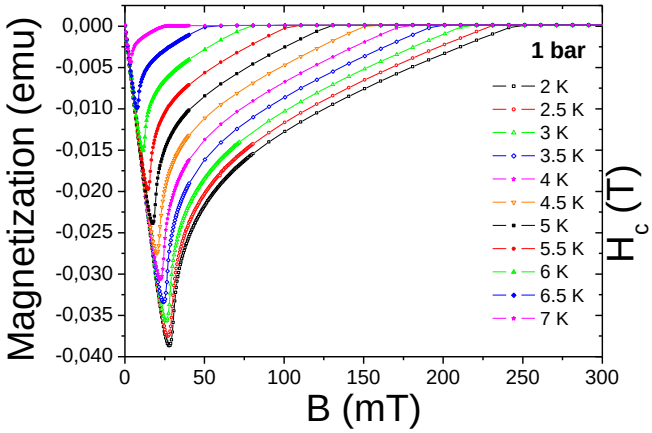

Fig. 1 Magnetization of YB_6 as a function of magnetic field for various different temperatures (virgin curves with increasing field).

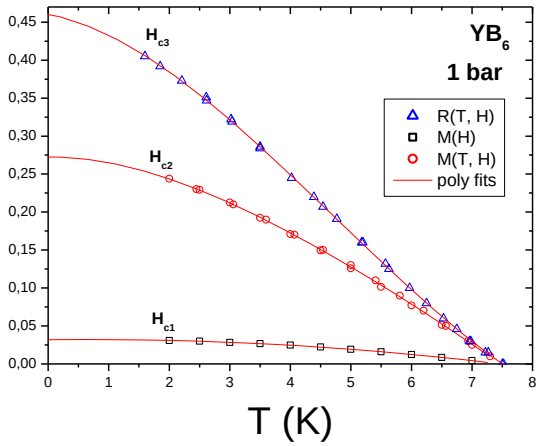

Fig. 2 Temperature dependences of the upper critical fields H_{c1}, H_{c2} and H_{c3} received from transport and magnetic measurements.

The field dependence of DC magnetization at temperatures from 2 to 7 K is shown in Fig. 1. The shape of curves is typical for a type-II superconductor. The superconducting phase diagrams were obtained from magnetization and resistivity (see Fig. 2). The critical fields $\boldsymbol{H_{c1}(0) \approx 0.03}$ **T**, $\boldsymbol{H_{c2}(0) \approx 0.27}$ **T** and $\boldsymbol{H_{c3}(0) \approx 0.45}$ **T** (the surface critical field) have been determined.

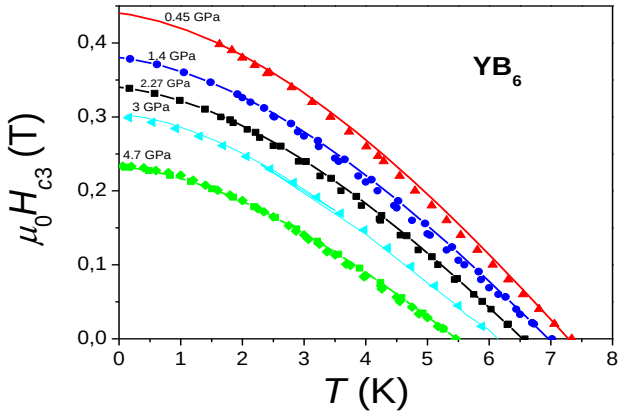

Fig. 3 Temperature dependences of upper critical field H_{c3} at 0.45, 1.4, 2.27, 3 and 4.7 GPa. Solid lines correspond to the fit of the WHH i.e. to the low-temperature s-wave BCS models.

Fig. 4 Photograph of the sample with four electrodes and Ruby in loaded diamond-anvil cell.

Data in phase diagram of the upper critical field H_{c3} (T) vs. T at various pressures up to 4.7 GPa (Fig. 3) were extracted from the electrical resistivity curves $\rho(T, H)$ measured in magnetic field between 0 and 0.5 T, at fixed temperatures down to 60 mK. The solid lines represent fits of the Werthamer-Helfand-Hohenberg (WHH) model to the experimental data. The values of the zero-temperature upper critical field $H_{c3}(0)$ at several pressures (see Fig. 5 (a)) were obtained. The linear fit yields $\mu_0 dH_{c3}(0)/dp$ = -0.0464 T/GPa.

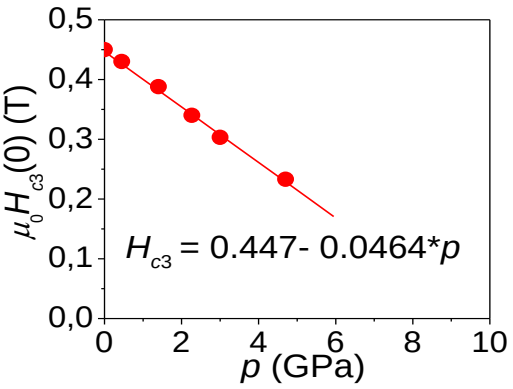

Fig. 5 (a) Pressure dependence of the upper critical field at T = 0.

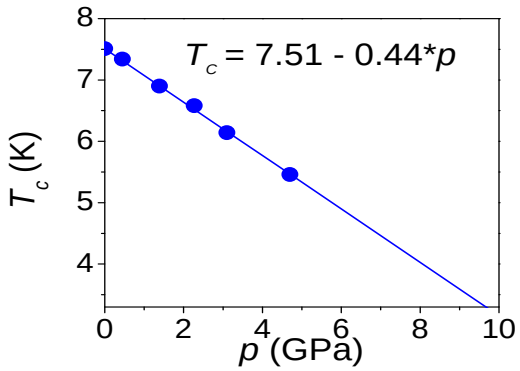

Fig. 5 (b) Pressure dependence of T_c at H = 0.

With increasing pressure the electrical resistivity (magnetoresistivity) curves shift almost parallel towards lower temperatures, implying a negative pressure effect on the transition temperature T_c (see Fig. 5 (b)). The linear fit yields dT_c/dp = -0.44 K/GPa. A general negative pressure effect on T_c and H_{c3} was observed.

References

[1] R. Khasanov, P.S. Häfliger, N. Shitsevalova, A. Dukhnenko, R. Brütsch, and H. Keller, Phys. Rev. Lett. **97** (2006) 157002.

Structure stability of the cubic γ-phase uranium molybdenum alloys

I. Tkach[1], N.-T.H. Kim-Ngan[2], S. Mašková[1], L. Havela[1], A. Warren[3], C. Stitt[3], T. Scott[3]

[1] *Faculty of Mathematics and Physics, Charles University, Ke Karlovu 5, 12116, Prague, Czech Republic, e-mail: ilimp@yandex.ru*
[2] *Institute of Physics, Pedagogical University, Podchorazych 2, 30-084 Krakow, Poland*
[3] *Interface Analysis Centre, University of Bristol, Oldbury House, BS2 8BQ, Bristol, United Kingdom*

Bcc U-Mo alloys were successfully prepared by splat cooling technique and characterized by X-ray diffraction and electron microscopy. Samples with 15 at.% Mo exhibit a pure γ-phase with *bcc* structure at room temperature, while with 11-12 at.% Mo show a stable γ^o-phase (tetragonal distorted γ-phase) [1]. Impurities of UC and UO_2 mostly segregated at the surface were observed in all samples. We performed phase stability investigation of γ-U as it is considered as a good candidate for low enriched nuclear fuel.
All samples were tested first for stability at ambient pressure of air. Our results indicate no visible changes on XRD of samples even after 1 year being exposed on air.
Thermal stability of splat samples with 12 at.% Mo and 15 at.% Mo was tested subsequently by annealing at temperatures 500 °C (773 K) and 800 °C (1073 K). Each sample was characterised by XRD after annealing time 4 h, 10 h, 72 h and 144 h. At annealing at 500 °C (Fig. 1 a, b), the α(021) reflection appeared after 4 h and increased after 10 h. At the same time the double peaks of initial γ^o-phase for sample with 12 at.% Mo transform into one broad peak of the γ-phase. With further increase of annealing time (72 h), the most intense γ-U peak γ(110) for both samples starts to split into double peaks of γ'-phase (known as U_2Mo) namely γ'(110) and γ'(103). So we can conclude that the splats are unstable at 500 °C.

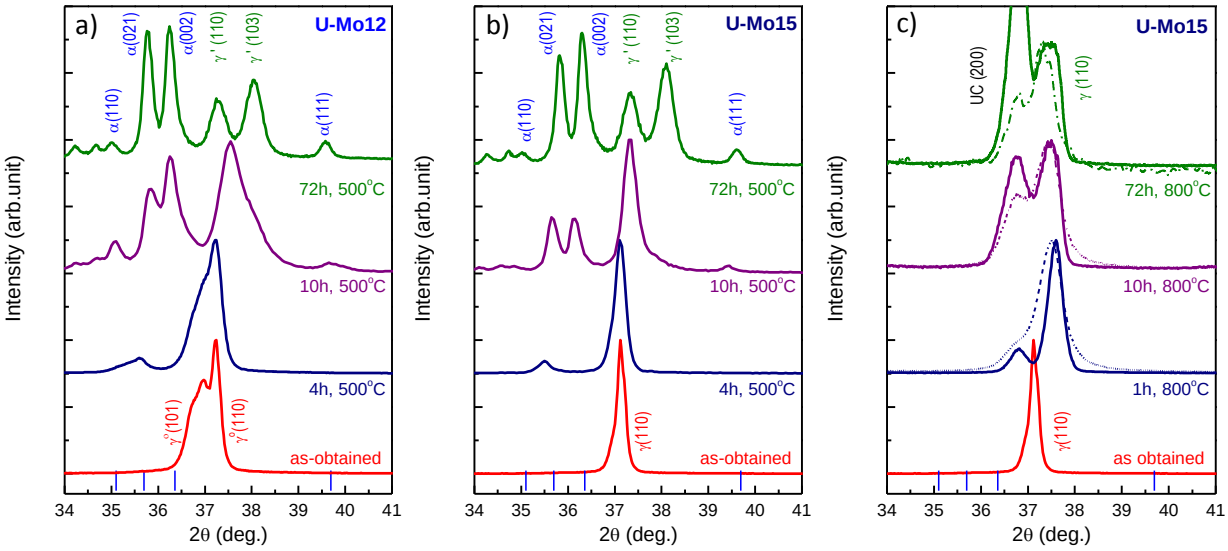

Fig. 1. Comparison of (low-angle) XRD patterns of the U-12 at.% Mo and U-15 at.% Mo splat samples in the as-formed state (γ^o and γ respectively) with those upon annealing at 500 °C (a,b) and 800 °C (c) for different annealing times. The (blue) vertical sticks indicate the main reflections of the orthorhombic α-U structure.

Upon annealing at 800 °C for 4 h, the sample with 12 at.% Mo transforms from γ^o to γ. More annealing time only increases intensity of the UC peaks. Sample with 15 at.% Mo behaves in

a similar way, preserving the γ-phase even for 144 h annealing (Fig.1 c). It is interesting that the annealing at 800 °C leads to the γ-phase even without subsequent quenching. The annealing effect may be in Mo homogenization.

Hydrogen absorption at room temperature was tested for pure-U splat and γ-phase alloys. While α-U sample quite easily, as expected, forms β-UH_3 hydride, γ-U samples did not absorb hydrogen at ambient pressure. With increase of hydrogen pressure over 2.5 bar, γ-U samples start to form hydrides with hydrogen concentration 3 H/U atom. On the contrary to known crystalline β-UH_3, which is highly pyrophoric fine powder, our hydrides have the form of 1-5 mm long brittle dark lamellas (Fig. 2), which are stable at air and have an amorphous structure (Fig. 3) with nanoscale grain size.

Such hydrides were tested by thermally stimulated desorption. Hydrogen release during heating is completed around 450 °C, going through the main outgassing around 250 °C. The sample was characterised by XRD also after desorption at 800 °C, which indicates γ-phase and UC, UO_2 impurities. XRD indicates mixture of γ-phase and α-phase with the same impurities in case of stopping annealing at 500 °C. We can suggest that heating up to 800 °C can cause not only desorption but also phase transformation like during annealing (homogenisation of γ-phase). On the other side, desorption at 500 °C also cause transformation of γ-phase into α-phase.

We suggest that crushing the hydride and desorption of hydrogen at 800 °C can be used for the production of γ-phase U-Mo fine powders as alternative to centrifugal atomization [2].

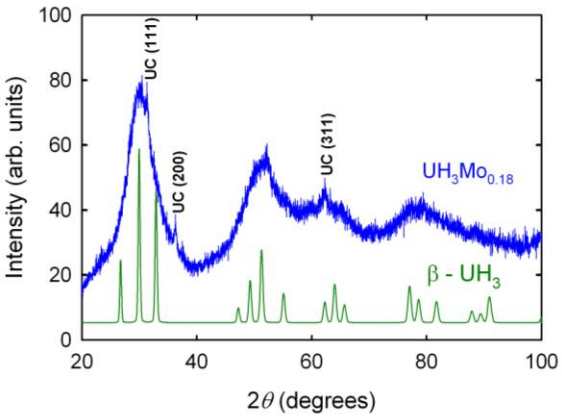

References

[1] I. Tkach, Nhu-T.H. Kim-Ngan, S. Mašková, M. Dzevenko, L. Havela, *J. Alloys Comp.* **101-109**, 534 (2012).
[2] K.H. Kim, D.B. Lee, C.K. Kim, G.E. Hofman, K.W. Paik, *J. Nucl. Mat.* **179-184,** 245 (1997).

Study on effect of Ge doping on magnetism of $CeNi_5$

Mariana Zapotokova,[1] Mauro Giovannini[2], Ivan Curlik[1], Jan Rusz[3], Miroslaw Werwinski[3], Marian Reiffers[1,4]

[1] *Institute of Experimental Physics, Slovak Academy of Sciences, Watsonova 47, 043 53 Kosice, Slovakia, e-mail:* vasilova@saske.sk

[2] *CNR-SPIN and Department of Chemistry, University of Genova, Via Dodecaneso 31, 16146 Genova, Italy*

[3] *Uppsala University, SE-75120 Uppsala, Sweden*

[4] *Faculty of Humanities and Natural Sciences, University of Presov, ul. 17.novembra 1, 080 78 Presov, Slovakia*

Many of Ce intermetallics are characterized by a strong hybridization of the magnetic *4f*-electrons with the conduction electron states which may results in a delocalization of the *4f*-level and in a change of occupancy level, and hence of Ce valence. One notable example of compound intensively studied for many years is $CeNi_5$ crystallizing in the hexagonal $CaCu_5$ type. Based on the various experimental results on Ce-Ni intermetallic system, Ce atoms in $CeNi_5$ are considered to be in the non-magnetic state and the sample, due to the Ni 3d band, to be an enhanced Pauli paramagnet near to a weak ferromagnet [1].
We have prepared the $Ce(Ni_xGe_{1-x})_5$ compounds with (x = 0; 0,1; 0,2; 0,5; 0,8) and studied the effect of the Ni/Ge substitution on the ground state of $CeNi_5$. The samples were prepared by arc melting technique and all the compounds crystallize in the $CaCu_5$ structure type (*P6/mmm* space group). The samples resulted to be single phase as confirmed by X-ray diffraction (XRD) and by electron probe microanalysis (EPMA). By substituting Ni by Ge, the lattice parameters of the unit cell increase linearly with the substitution of Ni atoms by bigger Ge atoms. $CeNi_5$ is a Stoner enhanced paramagnet characterized by a spin fluctuation contribution on its transport properties [2]. Its magnetic susceptibility $\chi(T)$ does not follow the Curie-Weiss law but shows a broad maximum around 100 K. In an effort to understand the reason for the existence of this maximum, it was found that Ce in this compound is nonmagnetic (it is almost in the 4+ valence state), and the maximum originates from the thermal smearing of the d electron density of state at the Fermi level, enhanced by spin fluctuations [1]. We provide results on ground state properties of these compounds obtained by measurements of heat capacity and electrical resistivity performed by PPMS commercial device (Quantum Design) in the temperature range 0.4 – 300 K and in applied magnetic field up to 9 T using 2-tau model of relaxation method and standard four probe AC technique, respectively. Magnetization and magnetic susceptibility measurements were performed by MPMS commercial device (Quantum Design) in the temperature range 2 - 300 K in an applied magnetic field up to 5 T. The temperature dependences of magnetic susceptibility in an applied magnetic field of 1 T for all the compounds are presented in Fig. 1. The broad maximum around 100 K for $CeNi_5$ is still visible in $CeNi_{4.9}Ge_{0.1}$ but it disappears in $CeNi_{4.8}Ge_{0.2}$. For higher concentrations of Ge dependences seem to be paramagnetic. This seems to indicate that the effect of Ni/Ge doping is to suppress the spin fluctuations. Fig. 2. shows the temperature dependences of the heat capacity for all the compositions $CeNi_{5-x}Ge_x$ (x = 0, 0.1, 0.2, 0.5, 0.8) reported in 0.4 - 200 K temperature range in zero applied field. The measurements show typical metallic behaviour for all samples. From the dependences $C(T)=T$

vs. T^2 (inset) we have determined the electronic Sommerfeld γ coefficient. The values (46, 54, 49, 17 and 23 mJ/molK^2, respectively) are very close to the value previously determined for $CeNi_5$ single crystal [3]. No sign of phase transition has been found, except for a small shoulder at about 6 K seen also in other Ce intermetallics and attributed to Ce oxide. In Fig. 3, the temperature dependence of the electrical resistivity $\rho(T)$ in zero applied magnetic field for $CeNi_{4.9}Ge_{0.1}$, as an example of the characteristic behaviour of all the samples, is presented. The trend of ρ (T) shows simple metallic behaviour without the sign of phase transitions. In order to study the infuence of magnetic field we have measured these dependences up to 9 T of applied magnetic field. The only feature which appears is the increase of the residual resistivity ρ_0, what is due to the Lorenz force (see inset of Fig. 3).

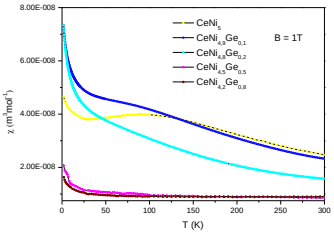

Fig. 1 Magnetic susceptibility versus temperature for all the compounds.

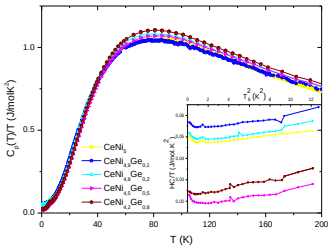

Fig. 2 Heat capacity dependencies for all the compositions in zero applied field. Inset: low temperature part of $C_p(T)$ over T versus T^2.

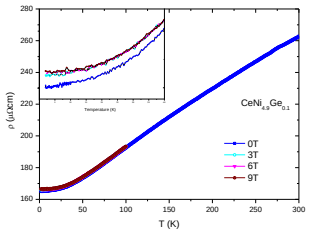

Fig. 3 Electrical resistivity of $CeNi_{4.9}Ge_{0.1}$ in different applied magnetic field 0 - 9 T. The inset shows low temperature detail.

The experimental results are compared to the theoretical predictions of the magnetic ground state evolution. To reproduce experimental concentrations we used two methods: Virtual Crystal Approximation (VCA) and supercells. Calculations were performed by using a full-potential augmented plane-wave method as implemented in the WIEN2k code [4]. We are presenting the dependency of magnetic energy ΔE on the Ge concentration x. In both approaches we observe a decrease of ΔE and achieving a paramagnetic ground state starting from certain value x of concentration of Ge. Obtained values of ΔE are small and indicate that the predicted magnetic ground state might not be very stable.

References

[1] D. Gignoux et al., J. Phys. (Paris) **43** (C7), (1982) 257
[2] M.Reiffers et al., J. Magn. Magn. Mater. **272-276**, (2004) 605
[3] P. Salamankha et al., J. Alloys Comp. **236**, (1996) 206.
[4] P. Blaha, K. Schwarz, G. Madsen, D. Kvasnicka and J. Luitz, *WIEN2k*, An Augmented Plane Wave +Local Orbitals Program for Calculating Crystal Properties (K. Schwarz, Techn. Universität Wien, Austria), 2001.

LIST OF POSTERS

P1. A.V. Andreev, S. Yasin, Y. Skourski, S. Zherlitsyn, J. Wosnitza, S. Mašková, L. Havela
High-field magnetization and magnetoacoustics of a U_2Ni_2Sn single crystal

P2. A.M. Cardinale, D. Macciò, G. Luciano, P. Traverso
Effect of Rare Earths Addition on Al-Si Hypoeutectic Alloys: Mechanical and Corrosion Behaviour, Thermal Analysis Results

P3. A. Gheorghe, R.-G. Manea, B. Negulici
Experimental Assessment Techniques for CANDU Steam Generators Degradation Mechanisms

P4. M. Giovannini, E. Bauer, H. Michor, T. Muramatsu, K. Shimizu, A. Amato
Reentrant quantum criticality in $Yb_2Pd_2(In,Sn)$ and Yb_2Pd_2Sn under pressure

P5. N.J. Harker, T. B Scott, C. P. Jones, J. R. Petherbridge & J. Glascott
Altering the hydriding behaviour of uranium metal by induced oxide penetration around carbonitride inclusions

P6. N.J. Harker, T. B Scott, G. C. Allen, J. R. Petherbridge & J. Glascott
3D ion mapping of nitro-carbide impurities in uranium metal using Magnetic Sector Secondary Ion Mass Spectrometry (MS-SIMS)

P7. N.J. Harker, T. B Scott & J. R. Petherbridge
Using EBSD to look for deformation in uranium metal surrounding carbide inclusions

P8. M.S. Henriques, A. Cruz, M. Kratochvílová, J. Marçalo, L. Havela, T. Stora, A.P. Gonçalves
Rare-earth electrospun carbides – model for submicron and nanostructured uranium carbides

P9. Yukio Hinatsu, Yoshihiro Doi, Akio Nakamura
Magnetic Studies on CoU_2O_6 and NiU_2O_6 by Magnetic Susceptibility, Specific Heat and Neutron Diffraction Measurements

P10. Hayao Imamura, Masahiro Kawazoe, Yoshihisa Sakata
Synthesis and Characterization of Nanostructured Cerium Nitride

P11. C. Jones, T.B. Scott, J. Petherbridge, J. Glascott
Structural deformation of metallic uranium surrounding hydride growth sites

P12. A. Keatley, T.B. Scott
Chemical Heterogeneity in Uranium Ore deposits: A case study South-West England

P13. S.A. Kulyukhin, E.P. Krasavina
Study of the U(Vl) Sorption on Layered Double Hydroxides under Different Conditions

P14. S.A. Kulyukhin, I.E. Veleshko, A.N. Veleshko
Method of plutonium preconcentration during sea water sampling

P15. M.A. Kuzin, O.I. Dreganov
Optimization of mechanical systems with abnormal functioning through the example of a precipitation centrifugation of powder precipitates

P16. A. Ochkin, D. Gladilov and S. Nekhaevskiy
Some Problems of Spent Fuel Reprocessing

P17. A. Ochkin, D. Gladilov and S. Stefanovsky
Estimation of the radiation hazard of curium after reprocessing of spent fuel

P18. A. Ochkin, S. Nekhaevskiy and D. Gladilov
Calculation of Organic Phase Composition in H_2O-$UO_2(NO_3)_2$-TBP System

P19. J. Rusz, F. Wilhelm, P. M. Oppeneer, G. Lander
First principles calculations of XMCD spectra of $NpOs_2$ and $PuFe_2$

P20. A. Saccone, S. De Negri, P. Solokha, M.Giovannini
Recycling of Neodymium from Nd-Fe-B magnets

P21. P. Solokha, R. Freccero, S. De Negri, D. M. Proserpio, A. Saccone
The crystal structure peculiarities of novel R_4MgGe_{10-x} (R=La-Nd, Sm, Gd-Dy) germanides

P22. I. Takáčová, S. Gabáni, G. Pristáš, E. Gažo and K. Flachbart
Influence of hydrostatic pressure on superconducting system YB_6

P23. I. Tkach, N.-T.H. Kim-Ngan, S. Mašková, L. Havela, A. Warren, C. Stitt, T.B. Scott
Structure stability of the cubic γ-phase uranium molybdenum alloys

P24. M. Zapotokova, M. Giovannini, I. Curlik, J. Rusz, M. Werwinski, M. Reiffers
Study on effect of Ge doping on magnetism of $CeNi_5$

LIST OF PARTECIPANTS

Adamska Anna Maria	Interface Analysis Centre, University of Bristol, UK
Agostini Pietro	National Agency for New Technologies, Energy and Sustainable Economic Development (ENEA), Italy
Alemberti Alessandro	Ansaldo Nucleare, Genova, Italy
Andreev Alexander V.	Institute of Physics, Academy of Sciences of The Czech Republic
Bram Avraham	Department of Materials Engineering, Ben-Gurion University, Israel
Broan Christopher John	National Nuclear Laboratory, Preston, UK
Caciuffo Roberto	European Commission, JRC, Inst. for Transuranium Elements, Germany
Cardinale Anna Maria	Dipartimento di Chimica e Chimica Industriale, Università di Genova, Italy
Colineau Eric	European Commission, JRC, Inst. for Transuranium Elements, Germany
Dorado Boris	CEA, DAM, DIF, Arpajon, France
Eloirdi Rachel	European Commission, JRC, Inst. for Transuranium Elements, Germany
Fournier Jean Marc	University of Grenoble, France
Geeson David	Atomic Weapons Establishment (AWE) Aldermaston, UK
Gheorghe Anca	Universitatea Politehnica Bucuresti, Romania
Gheorghe Valentin Paul	Universitatea Politehnica Bucuresti, Romania
Giovannini Mauro	Dipartimento di Chimica e Chimica Industriale - Università di Genova, Italy
Gorbunov Denis	Academy of Sciences and Charles University, Czech Republic
Grasso Giacomo	National Agency for New Technologies, Energy and Sustainable Economic Development (ENEA), Italy
Griveau Jean-Christophe	European Commission, JRC, Inst. for Transuranium Elements, Germany
Gumeniuk Roman	Max Planck Institute for Chemical Physics of Solids, Dresden, Germany
Halevy Itzhak	NED, Ben Gurion University and Nuclear Research Center Negev, Israel
Harker Nick J.	Interface Analysis Centre, University of Bristol, UK
Havela Ladislav	Faculty of Mathematics and Physics, Charles University, Czech Republic
Hen Amir	European Commission, JRC, Inst. for Transuranium Elements, Germany
Henriques Margarida S.	IST/ITN, Technical University of Lisbon, Portugal
Hinatsu Yukio	Division of Chemistry, Hokkaido University, Sapporo, Japan
Imamura Hayao	Graduate School of Science and Engineering, Yamaguchi University, Japan
Izosimov Igor	Joint Institute for Nuclear Research, Dubna, Russia
Jones Christopher P.	Interface Analysis Centre, University of Bristol, UK
Keatley Anya	Interface Analysis Centre, University of Bristol, UK
Khmelevskyi Sergii	CCMS, IAP, Vienna University of Technology, Austria.
Kulyukhin Sergey A.	Frumkin' Inst. Phys. Chem. and Electrochemistry, Russian Academy of Science

Kuzin Mikhail	JSC “State Scientific Center – Research Institute of Atomic Reactors”, Dimitrovgrad, Russia
Lander Gerry	European Commission, JRC, Inst. for Transuranium Elements, Germany
MacFarlane James	University of Bristol, UK
Manea Roxana-Georgiana	Universitatea Politehnica Bucuresti, Romania
Mansani Luigi	Ansaldo Nucleare, Genova, Italy
Martinelli Alberto	CNR-SPIN, Genova, Italy
Maskova Silvie	Dptm. of Condensed Matter Physics, Charles University, Czech Republic
Negulici Bodgan	Universitatea Politehnica Bucuresti, Romania
Ochkin Alexander V.	D.Mendeleev University of Chemical Technology of Russia
Pereira Gonçalves Antonio	IST/ITN, Technical University of Lisbon, Portugal
Reiffers Marian	Slovak Academy of Sciences and University of Presov, Slovakia
Ripani Marco	INFN Genova Italy
Rusz Jan	Department of Physics and Astronomy, Uppsala University, Sweden
Saccone Adriana	Dipartimento di Chimica e Chimica Industriale - Università di Genova, Italy
Samsel-Czekala Malgorzata	W. Trzebiatowski Inst. of Low Temperature and Structure Research, Poland
Scott Thomas B	Interface Analysis Centre, University of Bristol, UK
Shandalov Michael	Department of Physics, Nuclear Research Center Negev, Israel
Shick Alexander	Institute of Physics, ASCR, Czech Republic and European Commission, JRC, Institute for Transuranium Elements, Germany
Sladkov Vladimir	CNRS, Institut de Physique Nucléaire (IPN), Univ Paris-Sud, Orsay, France
Solokha Pavlo	Dipartimento di Chimica e Chimica Industriale - Università di Genova, Italy
Stitt Camilla	Interface Analysis Centre, University of Bristol, UK
Takácová Iveta	Slovak Academy of Sciences, Slovakia
Tereshina Evgeniya	Institute of Physics ASCR, Prague, Czech Republic
Tkach Ilya	Faculty of Mathematics and Physics, Charles University, Czech Republic
Tróc Robert	W. Trzebiatowski Inst. of Low Temperature and Structure Research, Poland
Vălu Sorin Octavian	European Commission, JRC, Inst. for Transuranium Elements, Germany
Vathonne Emerson	CEA, DEN, DEC, Centre de Cadarache, France
Wachter Peter	Laboratorium für Festkörperphysik, ETH Zürich, Switzerland
Wheeler David W.	Atomic Weapons Establishment (AWE) Aldermaston, UK
Wilhelm Fabrice	European Synchrotron Radiation Facility (ESRF), Grenoble, France
Zwicknagl Gertrud	Institut für Mathematische Physik, Technische Universität Braunschweig, Germany

INDEX OF AUTHORS

HITACHI
Inspire the Next

TM3000

Powerful SEM imaging and microanalysis on your desktop!

Features:

- SEM performance, but you don‘t realize it‘s a SEM:
  - Not any SEM typical alignment task such as beam alignment or stigma correction
  - No coating of samples, they remain as they are for further use
  - Point-and-shoot operation like a digital camera
- Magnification range up to 30.000x, and a depth of field >1mm
- Large samples (70mm x 50mm) with wide stage movement range
- Dual accelerating voltages (5kV, 15kV) allow greater flexibility in imaging and analysis of your samples
  - Low beam energy of 5keV provides surface information, also of soft matter
  - High beam energy of 15keV supports elemental analysis (EDS)
- Compositional and topographical imaging by annular, multi-segment electron detector
- Built-in measurement functions allow dimensional information to be acquired quickly and easily

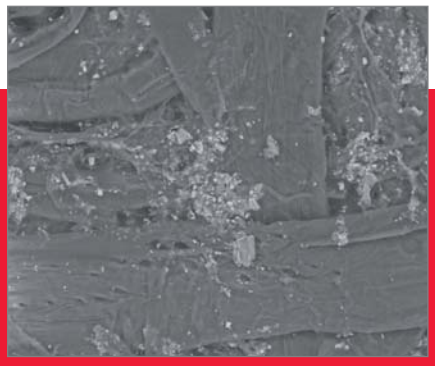

Paper bag, imaged in Normal Mode at 15keV beam energy.

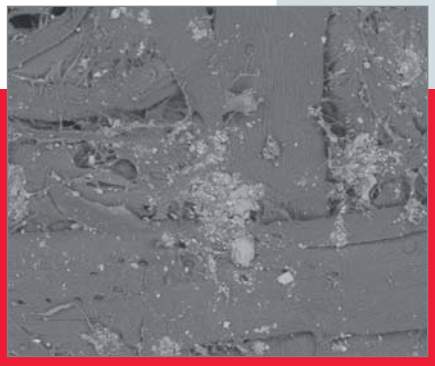

Same region image in Surface Mode at 5keV beam energy.

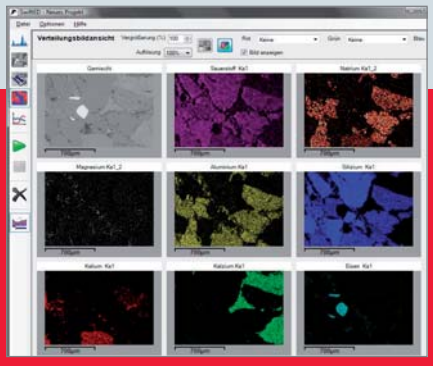

EDX mapping of polished sandstone. Acquisition time 10min.